

Single-Molecule Electronics with Graphene Nano-electrodes

By

Chit Siong Lau

Supervised by

Prof. G. Andrew D. Briggs, Prof. Jamie H. Warner & Dr. Jan A. Mol

Submitted in conformity with the requirements for the degree of

Doctor of Philosophy in Materials Science

Department of Materials

St. Anne's College

University of Oxford



June 2016

Copyright © by Chit Siong Lau

Declaration

The material contained within this thesis has not previously been submitted for a degree at the University of Oxford or any other university. The research reported within this thesis has been conducted by the author unless indicated otherwise.

Copyright Notice

The copyright of this thesis rests with the author. No quotation from it should be published without the prior written consent of the author, and other information derived from it should be acknowledged.

Abstract

Single-molecule electronics have attracted widespread attention for both basic scientific interests and potential in technological applications. However, development has been limited by the difficulty in fabricating robust nano-electrodes suitable for contacting individual molecules. Carbon based materials have recently emerged as alternative electrode materials and possess several distinct advantages over conventional gold based electrodes. This DPhil project is undertaken with the goal of developing graphene nano-electrodes and the subsequent fabrication and characterisation of graphene based single-molecule devices.

By combining the best of two prevalent approaches for fabricating graphene nano-gaps: feedback controlled electroburning and plasma etching, it is possible to produce graphene nano-gap with sizes 1 – 2 nm. The fabrication procedure is performed at room temperature and in ambient conditions with a high yield. Furthermore, arrays can be produced which makes the technique suitable for integration with conventional semiconductor technologies for scalable applications.

The graphene nano-electrodes are used to fabricate single-molecule transistors using porphyrin molecules. Due to the stability of the graphene nano-electrodes, the porphyrin single-molecule transistors show reproducible single-electron charging behaviour even at room temperature. High bias and gate transport spectroscopy can be performed where the excited energy spectrum of the molecule is measured.

Graphene-fullerene single-molecule transistors are studied. We observe electron avalanche transport and redox-dependent Franck-Condon blockade as a result of the strong electron-vibron coupling and weak vibronic relaxation of the system. The vibrational modes of the molecule are found to be due to both intrinsic vibrational and center-of-mass motion as verified by transport spectroscopy, Raman spectroscopy and DFT calculations. The current stability diagram of our device compares well with a rate equation model from which we extract the electron-vibron coupling constant.

Acknowledgements

This DPhil project would not have been possible without the contribution and support of many people. Indeed, the conditions laid out by my scholarship provided by ASTAR called for an especially challenging project; a collaborative effort between labs in Singapore and Oxford. The massive planning and coordination required would have been insurmountable without my supervisors, colleagues, scholarship officers, friends and family.

I would first like to thank all my supervisors and mentors: Prof. Andrew Briggs, Prof. Jamie Warner, Dr. Jan Mol, Dr. Wang Shi Jie and Prof. Andrew Wee, who all provided exemplary supervision and guidance. Jan, who introduced me to the field of quantum transport in single-molecule electronics and taught me almost everything I knew. Andrew, who provides invaluable insight and continually challenged me to rethink my conclusions and writings. Jamie, who is always patient, helpful and inclusive even when I am the only co-student in his group. Dr. Wang, who provided support and advice both in Singapore and Oxford, which must not have been easy. Prof. Wee, who even though is not an official supervisor, always took a keen interest in my work and took the time to meet up when I returned to Singapore and when he visited Oxford, in spite of his busy schedule.

The many research projects discussed in this thesis are the collaborative effort of many individuals. The porphyrin molecules are synthesized by Prof. Harry Anderson's group. The fullerene bisadducts are synthesized by Dr. Porfyrakis Kyriakos' group. Many thanks to Jonathan Cremers, Wilfred Lewis and Gregory Rogers who provided timely supplies of molecules in spite of my unreasonable and incessant demands. The Raman spectroscopy and mass spectroscopy of the fullerenes are performed by Panagiotis Dallas and Gregory Rogers. The DFT calculations are performed by Prof. Colin Lambert's group from the University of Lancaster. Many thanks to Hatef Sadeghi, Sara Sangtarash and Prof. Colin Lambert who provided invaluable assistance and advice concerning theoretical calculations.

My time spent in the lab would have been arduous without the guidance and training provided by the many postdocs and technicians. Many thanks to the postdocs in our group who took such great care of FWL lab and were patient when dealing with an impatient me: Edward Laird, Natalie Ares, Tian Pei, Pascal Gehring and Junjie Liu. Extra thanks to Junjie for taking the time to help me out in Physics with helium measurements. Paul Pattinson provided vital assistance in the cleanroom. Ten It Wong, Glen Goh, Yuli Huang, Brian Ong, Nancy Wong and Olga Neucheva provided technical expertise during my time in IMRE.

The administrative proceedings would have been difficult without the support of my scholarship officers from AGA. I would like to thank ASTAR and Prof. Andrew Briggs for financial funding and support.

Finally, I would like to extend my gratitude to my family and friends. To my friends and family in Oxford who made time away from home a far more pleasant experience. To my friends and family in Singapore who made it worth coming home. To Ele, who injected renewed energy with each visit. To my parents, I am sorry I was not around more.

Publications

Presented here is a list of works published during the course of this DPhil project. First authored publications are discussed in Chapters 2 – 4. Some of the co-author works listed here lie beyond the purview of this thesis.

Chapter 2

Lau, C. S., Mol, J. A., Warner, J. H. & Briggs, G. A. D. Nanoscale Control of Graphene Electrodes. *Physical Chemistry Chemical Physics* **16**, 20398–401 (2014).

Chapter 3

Mol, J. A.,* **Lau, C. S.**,* Lewis, W. J. M., Sadeghi, H., Roche, C. Cnossen, A., Warner, J. H., Lambert, C. J., Anderson, H. L., Briggs, G. A. D. Graphene-Porphyrin Single-Molecule Transistors. *Nanoscale* **7**, 13181–13185 (2015).

Chapter 4

Lau, C. S., Sadeghi, H., Rogers, G., Sangtarash, S., Dallas, P., Porfyrakis, K., Warner, J. H., Lambert, C. J., Briggs, G. A. D., Mol, J. A., Redox-Dependent Franck–Condon Blockade and Avalanche Transport in a Graphene–Fullerene Single-Molecule Transistor. *Nano Letters* **16**, 170–176 (2016).

Co-Author

Sadeghi, H., Mol, J. A., **Lau, C. S.**, Briggs, G. A. D., Warner, J. H., Lambert, C. J. Conductance Enlargement in Picoscale Electroburnt Graphene Nanojunctions. *Proceedings of the National Academy of Sciences* **112**, 2658-2663 (2015).

* Authors contributed equally to this work.

Puczkarski, P., Gehring, P., **Lau, C. S.**, Liu, J., Ardavan, A., Warner, J. H., Briggs, G. A. D., Mol, J. A. Three-terminal Graphene Single-Electron Transistor Fabricated Using Feedback-Controlled Electroburning. *Applied Physics Letters* **107**, (2015).

Tan, H., Fan, Y., Rong, Y., Porter, B., **Lau, C. S.**, Zhou, Y., He, Z., Wang, S., Bhaskaran, H., Warner, J. H., Doping Graphene Transistors Using Vertical Stacked Monolayer WS₂ Heterostructures Grown by Chemical Vapour Deposition. *ACS Applied Materials & Interfaces* **8**, 1644-1652 (2016).

Table of Contents

Chapter 1: Introduction.....	1
1.1 Top Contact Junctions	3
1.1.1 Scanning Probe Microscopy.....	3
1.2 Metal Nano-electrodes.....	4
1.2.1 Mechanically Controlled Break Junctions.....	4
1.2.2 Electromigrated Break Junctions	8
1.2.3 Conclusion.....	11
1.3 Carbon based Nano-electrodes	12
1.3.1 Carbon Nanotubes	12
1.3.2 Graphene.....	15
1.3.3 Conclusion.....	21
1.4 Electron Transport through Single-Molecule Transistors.....	22
1.4.1 Three-terminal Devices	22
1.4.2 Conclusion.....	30
References	33
Chapter 2: Nanoscale Control of Graphene Nano-Electrodes.....	44
2.1 Introduction.....	44
2.2 Fabrication	44
2.3 Nano-gap Characterization and Modelling	46
2.4 Conclusion	53
References.....	54
Chapter 3: Graphene-Porphyrin Single-Molecule Transistor	56
3.1 Introduction.....	56
3.2 Experimental Setup	56
3.3 Transport Spectroscopy	58
3.4 Conclusion	65
References.....	67
Chapter 4: Electron-Vibron Coupling in a Graphene-Fullerene Single-Molecule Transistor..	71
4.1 Introduction.....	71
4.2 Experimental Setup	71
4.3 Orbital Degeneracy	73
4.4 Vibrational Excited States	75
4.5 Franck-Condon Blockade.....	80
4.6 Rate Equation Model.....	83

4.7 Temperature Dependence	87
4.8 Vibrations vs Oscillations	89
4.9 Avalanche Transport	90
4.10 Conclusion	94
References	95
Chapter 5: Final Conclusion and Outlook.....	99
References	103
Appendix I: Feedback Controlled Electroburning Codes	104
Python Code:	104
Adwin Code: Feedback	112
Adwin Code: Measure	115
Appendix II: Simmons Model Fit	116
Matlab Code: Simmons Function.....	116
Matlab Code: Simmons $I - V$ fit.....	117
Appendix III: Rate Equation Model	122
Matlab Code: Rate Equation Model	122
Matlab Code: Functions	129

Chapter 1: Introduction

Moore's law is the empirical observation that the number of transistors packed into a given unit of space approximately doubles every two years. This describes the pace at which downscaling of transistors on integrated circuits has progressed.¹ The scaling has led to impressive levels of computing power. However, the miniaturization of silicon-based electronics cannot continue indefinitely and is gradually approaching its fundamental limits in the near future.² To circumvent this obstacle, alternatives to silicon technology are required.

Single-molecule devices where individual molecules serve as active electronic components in functional devices represent the ultimate form of device scaling.³⁻¹¹ These devices consist of individual molecules bridging a pair of conducting nano-electrodes. They offer tremendous possibilities for technological applications due to unique advantages. These include lower cost and power consumption, potential for self-assembly and diverse electronic functions that can be tailored through clever chemical design and synthesis of molecular geometry and composition. The use of single molecules as circuit elements was envisioned as early as 1974 when Aviram and Ratner first proposed the molecular rectifier.¹² Since then, research into single-molecule electronics has proceeded rapidly. A wide variety of electronic functions performed by single molecules has been reported. They include diodes^{13,14}, switches¹⁵⁻¹⁸, transistors¹⁹⁻²³ and memory^{24,25}, demonstrating the potential of single-molecule electronics as candidates for next generation electronics. Even if single-molecule electronics fail to ever replace silicon as the technology of tomorrow, the field remains intriguing as fundamental science. The tiny size of a molecule means that charge transport through single molecules is governed by quantum mechanics which can lead to phenomena very different from those of conventional metals/semiconductors. Single-molecule devices therefore provide an excellent platform for the study of novel physical and chemical properties at the molecular scale.

Despite the impressive advances made over the past decades, there remain significant challenges for the field of single-molecule electronics. The main challenge lies in integrating nanometre sized molecules with macroscopic electronic elements. There are two main approaches for contacting molecules between electrodes. The first is top-contact junctions which involves the use of scanning probe microscopy such as scanning tunnelling microscopy (STM) and atomic force microscopy (AFM),^{26–36} mercury drop electrodes,^{37,38} thermally deposited films³⁹ and cross wire junctions.^{40,41} While useful for fundamental investigations, top contact junctions are not suitable for practical applications due to the cumbersome equipment involved. The second approach is to fabricate stable electrodes with nanometre separation for contacting single molecules.^{42–45} The possibility to integrate these nano-electrodes in electronic circuits and insert molecules in desired positions means that they are far more suitable for technological applications. Such nano-gaps are typically fabricated prior to the insertion of molecules and therefore provide the means to characterize the junction with or without the molecule in place. Additionally, nano-gaps can be fabricated in a planar architecture that allow the underlying substrate to be used as a gate electrode for electrostatic tuning of the single-molecule device.⁴⁶

Significant progress has been made towards fabrication and measurement techniques. The subsequent sections will contain a literature review on a variety of important techniques for fabricating conventional metal electrodes break junctions such as scanning probe microscopy junctions, mechanically controlled break junctions and electromigrated break junctions. Next, carbon based electrodes such as carbon nanotubes and graphene are introduced and a comparison with conventional metal electrodes is made. A section is devoted to describing electron transport in three terminal single-molecule devices. Finally, the review will conclude with a summary of challenges and prospects in the field and introduce the research projects conducted in this DPhil project.

1.1 Top Contact Junctions

1.1.1 Scanning Probe Microscopy

Scanning probe microscopy (SPM) includes the scanning tunnelling microscope (STM) and the conducting probe atomic force microscope (CP-AFM). In STM break junctions, an atomically sharp metallic tip is brought into contact with adsorbed molecules on a metallic surface which acts as the other electrode. The tip is feedback controlled with a piezo-actuator.²⁸ In this way, molecular junctions can be formed quickly and repeatedly, as illustrated in Fig. 1.

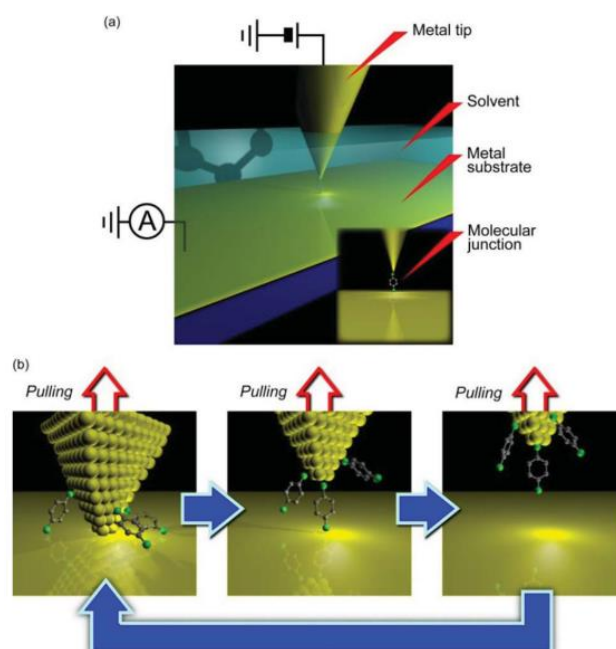


Figure 1. Schematic of the STM break junction. (a) The system consists of a metallic tip and a metal substrate covered with adsorbed molecules. (b) Tip is brought into contact with the substrate and retracted. The conductance through the tip decreases in steps corresponding to the number of contacted molecules until the last molecular junction is broken.⁴⁷

The working principle of the CP-AFM break junction is similar to the STM. The main difference lies in the size of the metallic tip which is significantly larger than the atomically sharp STM tip. This leads to higher uncertainty with regards to the number of contacted molecules. A critical requirement is to avoid applying excess pressure on the molecules which

may modify molecular conformation and electron transport. The CP-AFM has proved useful for investigating the relationship between molecular conformation and charge transport.

SPM based junctions have contributed greatly towards the understanding of electron transport through molecular junctions.⁹ Because of the large number of measurements that can be performed in a relatively quick fashion, robust statistical analysis of the conductance data shows peaks corresponding to the formation of preferred molecular contact geometry.^{16,26,27,31} Measurements on alkanedithiols reveal the exponential dependence of conductance on the molecular length.^{8,29,48,49} Molecules that are π -conjugated such as oligophenylenes,²⁷ oligopeptides,⁵⁰ caltеноide polyenes⁵¹ and oligothiophenes⁵² have also been studied where smaller tunnelling decay constants are observed. The smaller decay constants are due to the delocalisation of the highest occupied molecular orbital (HOMO) and lowest unoccupied molecular orbital (LUMO). The transition of charge transport from electron tunnelling to hopping has been reported in the systematic study of a family of long conjugated molecular wires.^{33,52-54} The main advantages of SPM junctions are its speed and versatility. The combination of high resolution imaging and spatially resolved scanning tunnelling spectroscopy provides the ability to probe local density of states with atomic spatial resolution. However, it is necessary to operate in good vacuum conditions in order to achieve clean contacts. Furthermore, SPM has a fundamental limitation for applications due to its size, complexity and lack of electrostatic gating. In order to truly realise functional integrated circuits nano-gap electrodes must be utilised and are the subject of the following sections.

1.2 Metal Nano-electrodes

1.2.1 Mechanically Controlled Break Junctions

The mechanically controlled break junction (MCBJ) is a technique for fabricating electrodes with a controllable separation of a few nanometres.^{42,55-57} As its name suggests, mechanical forces control the distance between the electrodes. Fig. 2 shows a schematic of the MCBJ technique. A lithographically defined notched metallic free-standing bridge is glued to a flexible elastic substrate which serves as a bending beam. This substrate is typically

composed of a phosphor-bronze sheet^{3,46} for improved flexibility and compatibility with electron beam lithography, allowing for a wider variety when depositing metal electrodes. A three-point bending geometry is employed where the substrate is bent by pushing the centre with a piezo-controlled pushing rod. The metallic wire is mechanically stretched until a break occurs resulting in a tunnelling nano-gap between two electrodes. This design allows for sub-picometre resolution through the manipulation of the pushing rod displacement that can be controlled at the nanometre level.⁴²

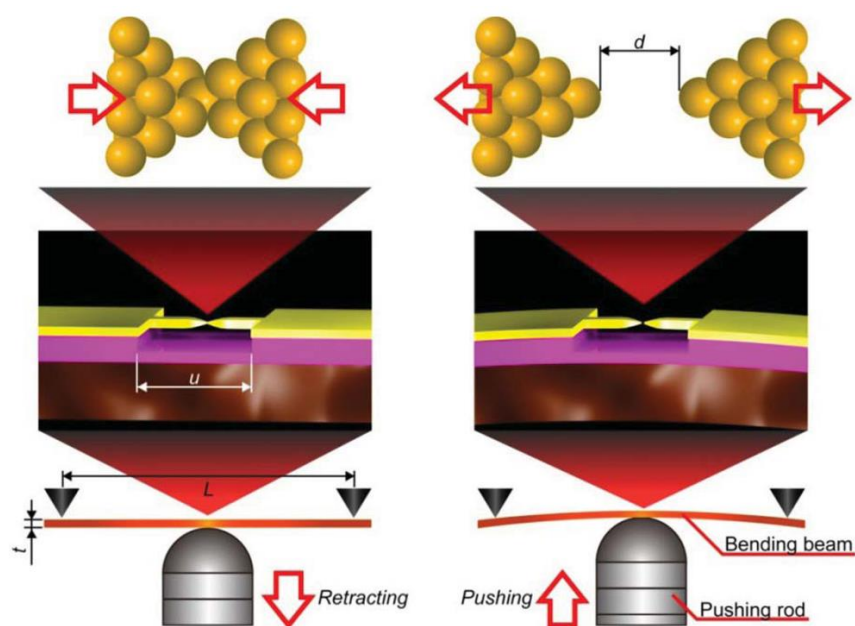


Figure 2 Schematic of the MCBJ. A suspended metal constriction on a flexible substrate is fabricated using standard electron beam lithography. The substrate is bent by the piezo-controlled pushing rod which induces tensile force on the suspended constriction. A break forms resulting in a nano-gap of size d that can be tuned by the vertical displacement of the pushing rod.⁴⁷

The MCBJ's outstanding stability enables room temperature experiments to probe stability and conductance of single molecule junctions.^{47,58} Paired with the ability to continuously adjust the size of the nano-gap size without polluting the junction, large number of measurements can be carried out on a target molecule allowing statistical analysis of the transport measurements.⁵⁹ Stable junction configurations can be identified from the peaks of conductance histograms. The stability of the technique is shown in the investigation of single

bipyridyl-dinitrooligophenylene-ethynylene dithiol (BPDN-DT) molecules. Reversible and controllable switching of the single-molecule junction is demonstrated where the system retained its switching even after more than 500 positive and negative bias sweeps.⁶⁰ Comparison with bipyridyl oligophenylene-ethynylene dithiol (BP-DT) molecules shows that the switching effect can be attributed to the nitro groups of the BPDN-DT and is not due to molecule-electrode coupling or electrode properties.

A significant advantage of the system is that the nano-gaps are only formed during the experiment. This means that cleanliness conditions during sample fabrication are comparably less stringent. Molecules can be self-assembled on the gold wire prior to the breaking process.⁶¹ After the nano-gap is formed, the metal electrodes are covered with a monolayer of molecules. By carefully monitoring the junction conductance while simultaneously reducing the nano-gap size, the formation of a single molecule junction can be determined. The MCBJ has proved useful for investigating metal-molecule contact stability. This is demonstrated in an experimental study of the room temperature stability of Au-S and Au-NH₂ contacts. The natural lifetimes of two types of molecular junctions each containing a distinct anchor group, thiol or amine, are measured.³² Au-thiol bonds are found to be far more stable than Au-amine linkages; single-molecule junctions composed of the former are a factor of 10⁵ more stable.

While MCBJs have contributed enormously to fundamental studies, there are several limitations.^{3,42,46} Highly integrated devices which are necessary for technological applications is a challenge in MCBJs due to the constraints imposed by the bulky piezo-components. The components impose an upper limit to the gap size and larger gaps are difficult to produce. Compared to scanning probe microscopy junctions, MCBJs cannot obtain surface topography of the sample. Thermal effects are a necessary consideration. Because of the high electric field applied, electron-phonon coupling can induce significant local heating leading to junction instabilities.^{62,63} Large thermal resistance at Au-benzenedithiol contacts are observed due to the phonon mismatch between the low energy acoustic phonons of the Au electrodes and the high energy optical vibration modes of benzenedithiols which impeded heat dissipation from

the junction to the electrodes.⁶³ Vertical dissipation through the substrate is not applicable due to the suspended nature of the junction. As a result, the current carrying capacity of single-molecule junctions is limited. But perhaps the most limiting factor in early forms of MCBJs is the lack of a gate terminal which hindered fundamental investigation into molecular energy spectrum and inhibited the development of devices such as field effect transistors (FET). Without a gate electrode, controlled electron transport through the molecule is not possible.

There have been attempts to implement the gate electrode through either a bottom^{64,65} or side gate geometry.⁶⁶ In the former, a back gate is implemented by fabricating the device on top of a doped silicon chip with a layer of oxide (Fig. 3a). Hydrofluoric acid is then used to etch away the oxide layer and suspend the Au constriction. However, in such a device the amount of bending allowed is limited due to the brittle Si chip and is usually insufficient to break the constriction through solely mechanical tensile stress. Frequently, electromigration is required to fully break the junction. Even then, the main advantage of the MCBJ, the ability to vary the gap size, is much diminished. Another approach for introducing a bottom gate is a sandwich-type architecture where the source-drain electrodes are directly deposited on a plasma oxidised Al gate such that both source-drain and gate electrodes are suspended above the substrate (Fig. 3b).⁶⁵ The source-drain electrodes are then broken while the electrical continuity of the gate is maintained. Charge transport through the junction is demonstrated where a gate voltage up to 1.8 V can be applied and Coulomb blockade is observed. However, the gate voltage range is unable to access more than a single redox state. A larger substrate bending is also required to break the Au constriction in such an architecture. Again, mechanical forces are limited to producing gaps sizes up to a few angstroms and an additional electromigration step is required. In side gate approach, a metal gate electrode is fabricated lithographically on the shoulder located a few nanometres away from the suspended constriction as shown in Fig. 3c.⁶⁶ The gate electrode remains unchanged when bending the substrate. However, the molecular junctions become unstable and can collapse when gate voltages are increased beyond 10 V. Gating can only be observed with high bias voltage. In

addition, the variability of the lithography process means that only gate electrodes that are sufficiently close to the junction show gate coupling. The gate coupling is sensitive to the exact position of the molecule; devices with molecules located on the far side result in gate failure due to screening of the electric field by the source-drain electrodes. A yield of only 18% (12 out of 67 devices) is obtained for typical FET behaviour. There remain additional drawbacks with the use of Au electrodes which shall be discussed together with the electromigrated break junction technique in the next section.

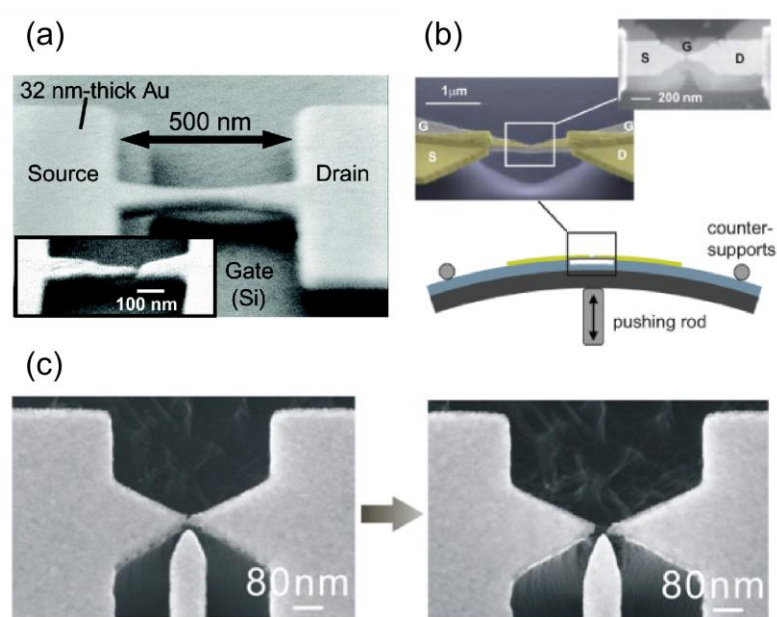


Figure 3 Three terminal MCBJ architectures. (a) Bottom gating using a doped silicon substrate. Reprinted with permission from [64], copyright (2005) American Chemical Society. (b) Al back gate is in direct contact with the source-drain electrodes.⁶⁵ (c) Side gate using a lithographically defined Au nano-electrode. Reprinted with permission from [66], copyright (2013) American Chemical Society.

1.2.2 Electromigrated Break Junctions

Electromigration is a process where ions are gradually transported at high electrical current densities due to momentum transfer from conduction electrons to lattice ions.⁶⁷ Electromigration is well studied as a major failure mode in microelectronics⁶⁸ and has now been applied to nano-gap electrode fabrication.^{21,43,55,69} A voltage ramp applied to a lithographically defined metal constriction causes electromigration of the metal atoms resulting

in eventual breakage. This produces two nano-electrodes separated by distances down to 1 – 2 nm (Fig. 4). Molecules can be introduced either before or after nano-gap formation via solution or thermal evaporation.³ Depositing molecules before forming the nano-gap is preferred as it reduces contamination in the gap.

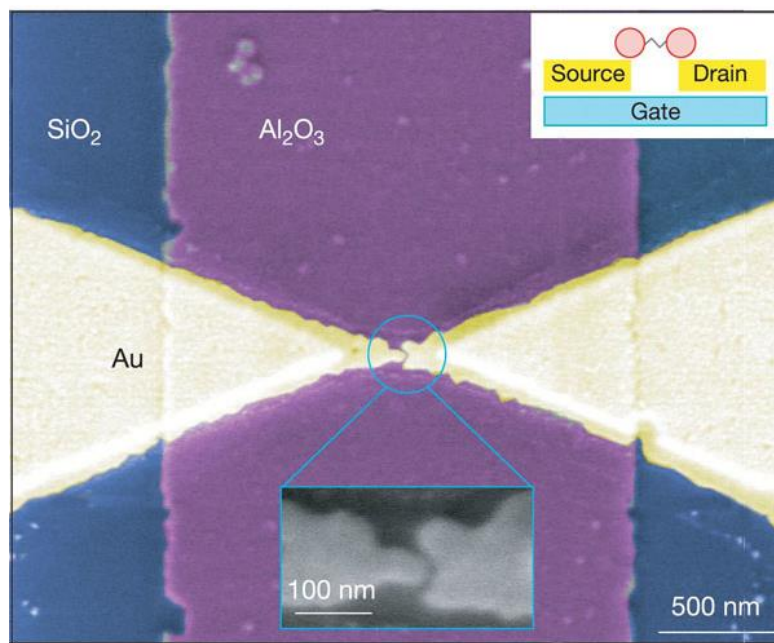


Figure 4 SEM image (false colour) of an electromigrated break junction. Two Au nano-electrodes are separated by ~1 – 2 nm above an Al pad covered with a ~3 nm thick layer of oxide. The Al pad serves as a gate electrode. Inset: Schematic diagram of single-molecule transistor composed of individual divanadium molecules. Reprinted with permission from [69], copyright (2002) Nature Publishing Group.

The most important difference of electromigrated break junctions (EBJ) compared to MCBJs and SPM based junctions is the solid contact of the electrodes with the substrates resulting in four main advantages. Firstly, excellent mechanical stability is obtained which is important for studying electron transport through molecular junctions subjected to external electromagnetic fields.⁴⁷ Secondly, no stringent requirements exist for the substrate as compared to MCBJs which requires flexible substrates; or SPM based junctions that require conducting substrates. Thirdly, the planar architecture is suitable for integrating large arrays for applications. Lastly, and perhaps the most critical difference, is the ability to prepare three terminal devices using the substrate as a gate electrode.^{21,43,55,69,70} This enables fabrication of

devices, such as single electron transistors, and fundamental investigation into physical phenomenon such as Coulomb Blockade^{55,71} and Kondo effect.^{55,69}

EBJs are used to fabricate colloidal cadmium selenide nanocrystals based single-electron transistors.⁴³ Up to 60% of the fabricated devices showed single electron tunnelling characteristics upon depositing the nanocrystals. EBJs are instrumental in the study of nano-mechanical oscillations of a single C₆₀ molecule due to coupling between tunnelling electrons and center-of-mass motion of the molecule.²¹ Transport measurements through a single molecule magnet led to the observation of complete current suppression and negative differential conductance on the energy scale of the magnetic anisotropy barrier.⁷⁰ Charge state dependent Kondo effect is observed in a single molecule transistor where an individual divanadium molecule serves as the spin impurity (Fig. 4).⁶⁹ The Kondo effect occurs when the charge state corresponded to an unpaired electron which serves as a spin impurity coupled to the lead electrodes.

A crucial factor in obtaining high quality junctions is the local temperature in the gap, where high current densities can result in excessive Joule heating.⁷² This leads to undesired melting that produces large gaps, destruction of molecules and unintentional formation of metal debris in the gap. The metal islands interfere with the insertion of molecules and mask intrinsic molecular characteristics. The problem can be circumvented by minimising the total series resistance of the system and keeping the temperature low as demonstrated with EBJs fabricated on free standing transparent SiN_x membranes. The SiN_x membranes enables transmission electron microscopy (TEM) to image the gap formation process in situ.⁷³ The nano-gaps so produced when minimising the total series resistance are found to be clean and free of debris.

Even better yield and reproducibility have been obtained through the use of feedback control. Instead of a single voltage ramp, the bias voltage can be feedback controlled such that the applied voltage is dependent on the junction resistance. This prevents thermal runaway that leads to large gaps. Feedback control enabled the parallel fabrication of a 15-

junction array in a single step by ensuring that the inter-junction resistance is smaller than the individual junction resistance (Fig. 5).⁷⁴ This allows even power dissipation between the junctions resulting in successful fabrication of arrays which is promising for integrated circuits of molecular devices. The main drawback of EBJs compared to MCBJs is the inability to vary the gap size in situ. As mentioned in the previous section, a combination of the two techniques overcomes this problem but limits the range of gap sizes as well as introducing drawbacks associated with MCBJs such as bulky piezo components.

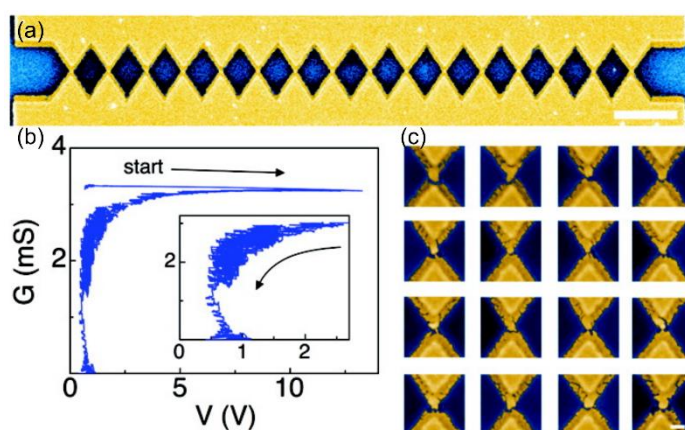


Figure 5 Parallel fabrication of nano-electrodes array by feedback-controlled electromigration. (a) SEM image (false colour) of 16 junctions defined by electron beam lithography and shadow evaporation. Scale bar: 1 μm . (b) Conductance G as a function of the bias voltage V during the feedback-controlled electromigration process. (c) SEM images of the nano-gaps formed from the 16 junctions. Scale bar: 100 nm. Reprinted with permission from [74], copyright (2007) American Chemical Society.

1.2.3 Conclusion

To summarise this section, the drawbacks of Au nano-electrodes employed in MCBJs and EBJs are discussed. In both techniques, the uncontrollable microscopic details of the breaking process mean that the local shape and atomic configurations of the electrodes can vary substantially. As the molecular junction is sensitive to its atomistic configuration, large ranges of conductance values are reported for the same junction.^{4,75–80} This is further exacerbated by a number of factors. Applied bias voltages can lead to large electric fields over the 1 – 2 nm long junction. At typical electric fields of 10^9 Vm^{-1} , Au atoms at the electrode

surface start to diffuse.⁷ Additional fluctuations occur from thiol anchors, the preferred anchor groups for binding to Au, which can switch stochastically between bonding sites.³² The high atomic mobility of Au nano-electrodes is a major problem for stable room temperature device applications. Furthermore, effective gate coupling is challenging due to gate screening by the bulky Au electrodes.^{81–84} Replacing Au with other metals is not ideal since other metals are easily oxidised under ambient conditions. Given these fundamental issues, carbon based electrodes such as carbon nanotubes (CNT) and graphene^{85,86} have emerged as alternatives for molecular electronics and will be the focus of the following section.

1.3 Carbon based Nano-electrodes

Carbon based electrodes possess certain superior characteristics compared to Au electrodes. Their covalent structure ensures stability up to high temperatures far in excess of room temperature.^{7,86,87} CNTs have current carrying capacity that exceed $10 \mu\text{A nm}^{-2}$, 1000 times higher than that of noble metals. Graphene possesses extraordinary thermal conductivity, electron mobility and current carrying capacity including ballistic transport at room temperature.^{44–46,85–88} Unlike bulky Au electrodes, carbon based electrodes are better suited for contacting to diverse organic molecules through interactions such as covalent bonding or $\pi - \pi$ stacking. Moreover, gate screening that limits electrostatic control using Au electrodes is substantially minimised due to the extremely reduced spatial dimensions; graphene is a single atomic layer of sp^2 bonded carbon atoms while CNTs are essentially rolled up graphene sheets.

1.3.1 Carbon Nanotubes

Single-walled carbon nanotube (SWNTs) nano-electrodes have been fabricated through precise oxidative cutting (Fig. 6).⁴⁴ SWNTs grown through chemical vapour deposition (CVD) with diameters of $\sim 1 - 2 \text{ nm}$ are contacted by metallic electrodes separated by $20 \mu\text{m}$. A 10 nm sized window is opened in a layer of PMMA using electron beam lithography (EBL). Oxygen plasma ion etching is used to cut the nanotubes through the open window resulting in gaps with an upper limit of $\sim 10 \text{ nm}$. Due to the strongly oxidising conditions a prevalence of

carboxylic groups is expected to terminate the CNT edges (Fig. 6a). A molecular bridge with amine end groups is then covalently attached to the CNTs through amide linkage by a dehydration reaction. These functionalised contacts are useful for fabricating devices with a variety of molecules to produce pH sensors, photogated switches and DNA hybridization sensors. The technique was subsequently improved by another group to realise in situ and real time characterization during multi-walled carbon nanotubes (MWNTs) fabrication (Fig. 6(b-g)).⁸⁹ The MWNTs are cut using oxidative plasma etching to produce initial gap sizes between 10 – 60 nm. Organic molecules are deposited onto the MWNTs and finally electron beam induced decomposition (EBID) of the molecules result in broadening of the MWNT diameter and reduction in the gap size. This step is carried out using the scanning electron microscope such that in-situ characterization and precise control of the gap size is possible. DNA molecules are then assembled between the electrodes by $\pi - \pi$ stacking interactions. The current-voltage characteristics before and after assembly are taken where an increase in current after molecular deposition is observed.

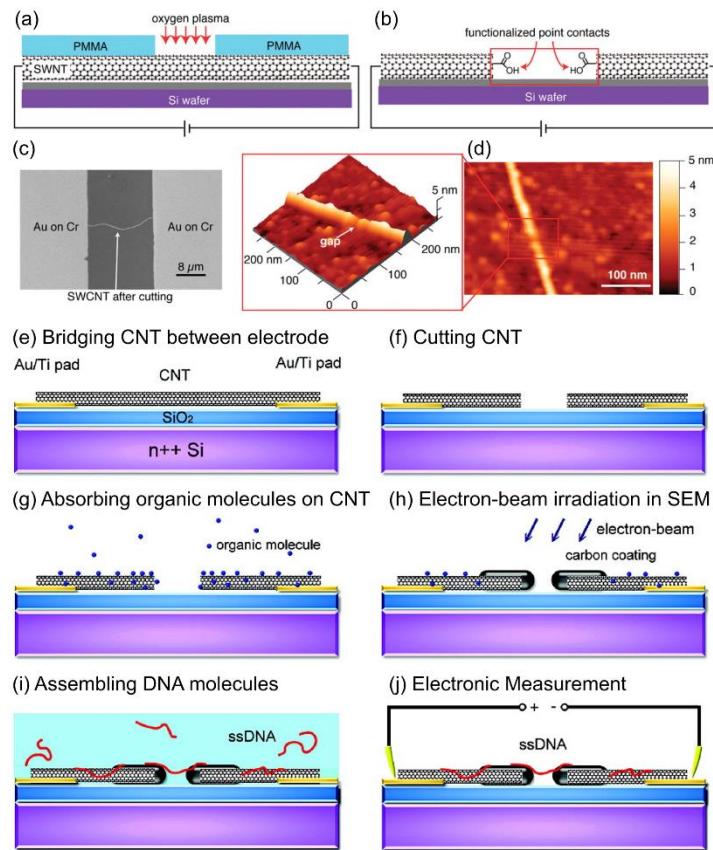


Figure 6 CNT nano-electrodes. (a) Schematic of precise oxidative cutting of SWNTs through a window of EBL defined PMMA. (b) Oxidative cutting produces two point-contacts separated by as close as 2 nm with their ends functionalised by carboxylic groups. (c) SEM of a cut SWNT on Au/Cr leads. (d) AFM image of the SWNT nano-gap. Inset shows the height profile of the isolated tubes ~ 1.6 nm. Reprinted with permission from [44], copyright (2006) American Association for the Advancement of Science. (e-f) Schematic of CNT nano-electrodes fabricated using SEM EBID for in situ characterization and assembly. DNA molecules are introduced by immersing in DNA buffer solution and the electronic properties of the bridged DNA molecules are measured. Reprinted with permission from [89], copyright (2008) American Chemical Society.

Electrical breakdown technique similar to the electromigration for Au electrodes can also be applied to CNTs.^{90,91} Organic field effect transistors (OFETs) with channel lengths down to 1 – 3 nm have been demonstrated with SWNT electrodes fabricated using electrical breakdown. Pentacene nanocrystal transistor using CNT nano-electrodes fabricated with electrical breakdown demonstrated Coulomb blockade at 4.2 K and controllable transistor operation at room temperature.⁹⁰ The evaporated pentacene are found to selectively grow around the electrodes possibly due to the common unit composition of six membered rings of

both the CNTs and pentacene. This leads to the commensurate absorption of the molecule on the nanotube surface due to strong van der Waals force.

A third technique utilised focused ion beam (FIB) to make MWNT nanoelectrodes.⁹² A focused Ga²⁺ ion beam with a beam size down to 22 nm in diameter is used to define gaps down to 50 nm. The CNT nano-electrodes are then used to fabricate a nanoscale C₆₀ FET which exhibited good performance with a low voltage drive operation. While the nano-gaps defined in this way are larger compared to the previous two techniques, the main advantage compared to oxygen plasma ablation is that lithography is not required. This reduces contamination from incomplete removal of resist residue. Compared with the electrical breakdown technique the position and width of the gap along the CNT can be controlled which makes it easier to align with additional gate electrodes.

1.3.2 Graphene

Graphene, the 2D counterpart of CNTs, is also considered a prime candidate for nano-electrodes.^{7,85,93} In addition to the benefits associated with carbon based electrodes such as reduced gate screening, compatibility for contacting organic molecules and high stability, graphene offers additional advantages. In particular, high quality single and few layer graphene can now be reliably grown on the wafer scale with chemical vapour deposition.^{94–97} This makes graphene an extremely attractive candidate for scalable applications compared to CNTs. Graphene devices have been fabricated on 200 mm wafers in an entirely silicon complementary metal-oxide-semiconductor (CMOS) process by cleverly reversing the order to passive first active last.⁹⁸ The ultra-high mobility of graphene has been demonstrated where 40 nm wide graphene nanoribbons show room temperature ballistic transport on length scale greater than 10 μm with an equivalent sheet resistance below 1 ohm per square.⁸⁸

Motivated by these advantages several approaches have been formulated to fabricate graphene nano-gaps. One such approach is AFM nanolithography.⁹⁹ In this technique, the AFM tips are used as ‘knives’ to define the nano-gaps in graphene and graphene oxide.

Square and linear arrays are demonstrated (Fig. 7). The process is fast and does not require any lithography steps that would otherwise introduce resist residue. However, the nano-gap sizes are limited by the AFM tip size, with the smallest gap obtained ~ 10 nm. Another approach utilises anisotropic etching of monolayer graphene using thermally activated nickel nanoparticles (Fig. 8).¹⁰⁰ The etching is based on catalytic hydrogenation of carbon atoms from graphene edges resulting in trenches across the graphene surface. These gaps can be down to 10 nm in width depending on the size of the nanoparticles. However, the technique is unsuitable for defining arrays as there is no way to control the direction of etching. Similar to electrical breakdown in CNTs, the same technique applied to graphene is shown to produce gaps with sizes ~ 10 nm.¹⁰¹ These break junctions showed stable and reproducible switching behaviour at room temperature under high vacuum and can possibly be developed into memory devices. However, for single-molecule devices stable nano-gaps are required. Nano-gaps can also be formed using mechanical stress by first employing standard EBL process to produce freestanding graphene bridges which are then torn apart by surface tension of solvent during the drying process.¹⁰² The resulting gaps are a few hundred nanometres. This technique easily produces gaps with atomically parallel edges.

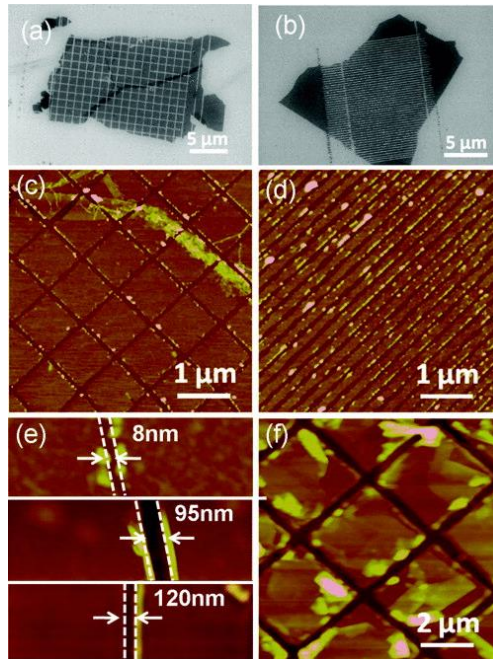


Figure 7 SEM images of fabricated nano-gaps using AFM nanolithography: (a) square arrays, (b) linear arrays. AFM images of (c) square arrays, (d) linear arrays, (e) nano-gaps and (f) nano-gap electrode arrays. Reprinted with permission from [99], copyright (2010) AIP Publishing LLC.

Single Layer Graphene

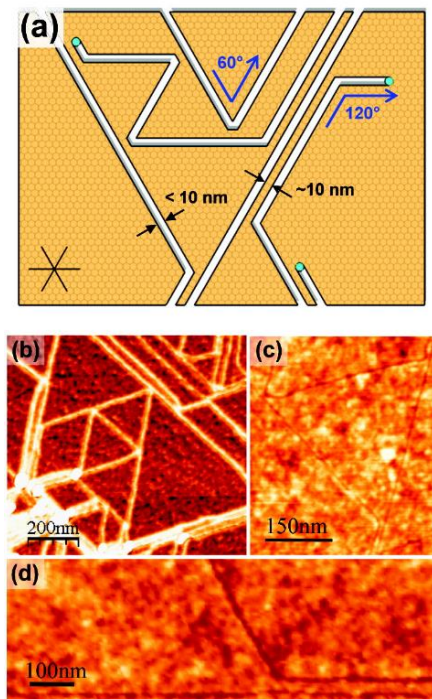


Figure 8 Schematic of etching with nanoparticles. (b) AFM phase image of the etched trenches. (c) AFM height image of etched triangle and of (d) a trench which avoided another trench and ran parallel to it. Reprinted with permission from [100], copyright (2009) American Chemical Society.

While the above mentioned techniques offer certain advantages in their own right, an important criterion for use in single-molecule devices has not been met. Sub 10 nm gaps cannot be reliably and controllably fabricated. This requirement is paramount for contacting individual molecules as larger gap sizes can result in the bridging of no or several molecules. In order to realise this requirement, two distinct approaches towards fabrication of sub 10 nm sized graphene nano-gaps have been developed. They are based on plasma etching¹⁰³ and feedback controlled electroburning.^{45,104} The former is similar to plasma etching of CNTs. By over-etching lithographically defined graphene point contacts gaps with sizes 1 – 10 nm can be obtained. Combined with the use of large area CVD grown graphene fabrication of arrays on the wafer scale with precise control over the position of the nano-gaps can be achieved. However, the key drawback is the yield which is only 33%.

Feedback controlled electroburning of graphene is similar to electrical breakdown of CNTs and electromigration of Au nano-electrodes, but with a higher degree of precision over the nano-gap size through the use of the feedback control.^{45,104} Studies have suggested that electroburning relies on a thermally activated reaction between reactive edge carbon atoms and oxygen at high temperatures induced by Joule heating at high current densities, hence the term 'burning'.^{105,106} The precise control over nano-gap sizes is demonstrated in the feedback-controlled electroburning of mechanically exfoliated few layer graphene (FLG) flakes at room temperature in ambient conditions.⁴⁵ The process starts with a voltage ramp applied to the graphene flakes while the current is continuously sampled. The current voltage characteristics of a typical electroburning procedure are shown in Fig. 9b. The first electroburning event is indicated by the decrease in the differential conductance. At a predetermined drop the feedback control rapidly sweeps the voltage back to 0 V before a new voltage ramp is applied. As the process continues the conductance decreases in steps while the voltage that indicates the onset of electroburning decrease. Once the device reaches a low-bias resistance in the range of 500 M Ω to 10 G Ω , the process stops and the fabrication of a nano-gap is deemed complete. In this work the yield obtained is much higher than the

plasma etching technique, with 35 out of 38 devices (92%) producing nano-gaps. More importantly, the fabricated nano-gap sizes are $\sim 1 - 2$ nm, the perfect size range for contacting single molecules. The nano-gaps are shown to be very stable, displaying only slight variations in the current-voltage characteristics after several weeks. These outstanding properties mean that the nano-gaps are suitable for fabricating single-molecule transistors.

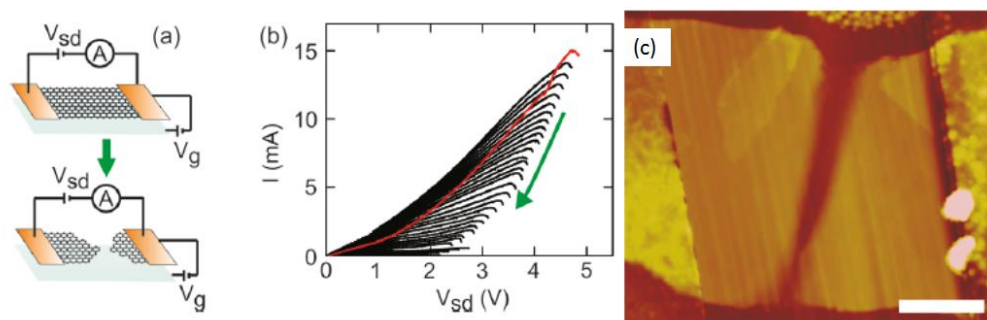


Figure 9 (a) Schematic of the feedback controlled electroburning on FLG. (b) Current-voltage characteristics during the electroburning process. (c) AFM image of a FLG nano-gap. The scale bar is $1 \mu\text{m}$. Reprinted with permission from [45], copyright (2009) American Chemical Society.

This is shown by the deposition of anthracene-functionalised curcuminoid molecules (1,7-(di-9-anthracene)-1,6-heptadiene-3,5-dione, abbreviated as 9Accm) on the nano-gaps. 14 out of 35 devices displayed an increase in conductance. Using the doped silicon substrate as a back gate, 4 out of 14 devices display gate dependent transport (Fig. 10a). That the conductance of the nano-gaps is gate independent before deposition is strong evidence for the formation of a molecular junction. The charge stability diagram where the current is measured as a function of the source-drain bias and gate voltage displays single electron tunneling¹⁰⁷ and Coulomb blockade¹⁰⁸ even though full Coulomb diamonds are not observed.

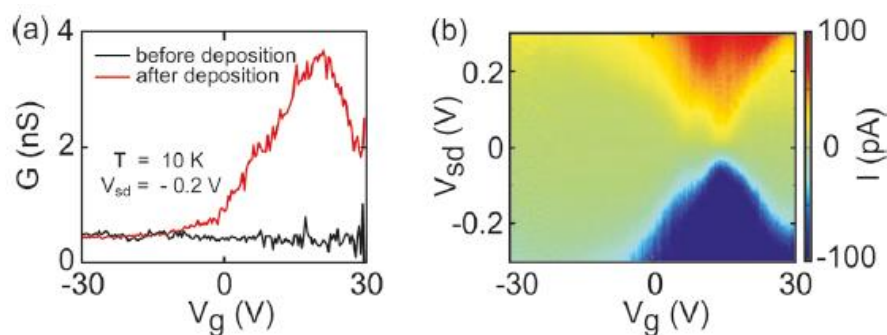


Figure 10 (a) Conductance through the graphene nano-gaps as a function of the gate voltage before and after the deposition of molecules. (b) Current stability diagram showing Coulomb blockade. Reprinted with permission from [45], copyright (2009) American Chemical Society.

The fabrication of sub 5 nm wide single layer graphene nano-gaps through electroburning without the use of a feedback has also been demonstrated.¹⁰⁴ CVD single layer graphene is first transferred onto a Si chip and patterned via EBL into 400 – 600 nm or 2 μ m wide constrictions. By alternating the bias voltage between a low (V_{low}) and high (V_{high}) value and superimposing a modulation voltage (V_{mod}) to measure the differential resistance, the change in the differential resistance at V_{high} , which corresponds to Joule heating effects, can be observed (Fig. 11). V_{high} is ramped in steps of 0.1 V (Fig. 11b). When the resistance at high voltage increases to a high value which indicates the breaking of the graphene constriction, the voltage is set back to 0 V. Graphene nano-gaps are thus fabricated in a single step without the use of a feedback. The yield of the technique is excellent at over 95%, with obtained gap sizes between 0.3 nm and 2.2 nm. However, this yield is only applicable to devices fabricated in vacuum. As the electroburning is sensitive towards the oxygen partial pressure, devices fabricated in ambient conditions had an extremely low yield of 20% with 2 out of 10 devices working.

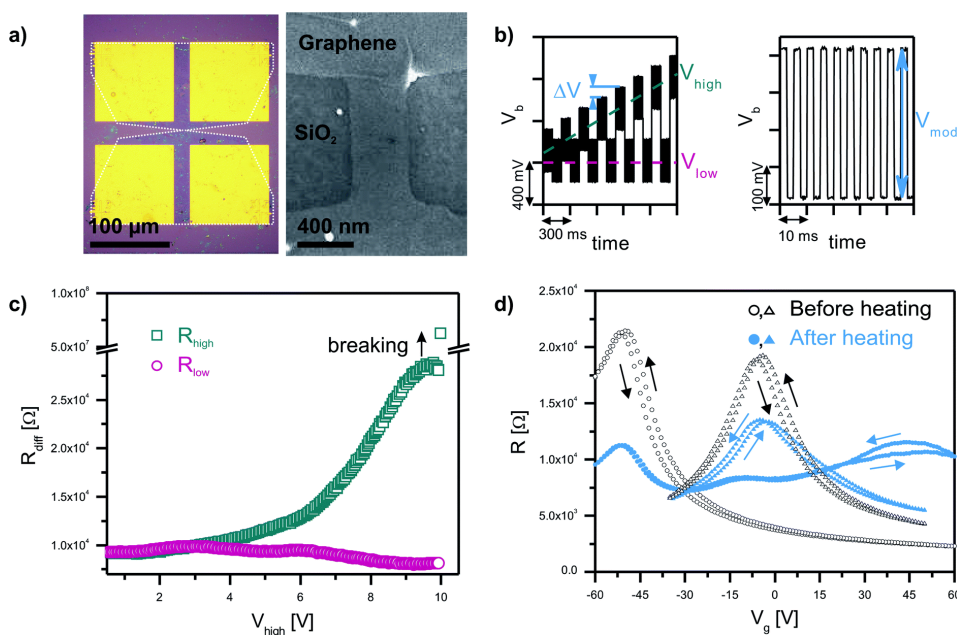


Figure 11 (a) Optical (left) and SEM (right) images of a graphene nano-gap sample. (b) Bias voltage applied during the electroburning process. The voltage is alternated between a high and low value while superimposing a modulation voltage to measure the differential resistance. (c) Differential resistance as a function of the high bias, which increases during breaking of the constriction. (d) Gate dependent resistance before and after heating the sample during electroburning but before breakdown for two different samples. Reprinted with permission from [45], copyright (2014) Royal Society of Chemistry.

1.3.3 Conclusion

Carbon based electrodes hold enormous potential for building single-molecule devices, circumventing shortcomings of gold based nano-electrodes while offering unique advantages. Feedback controlled electroburning is particularly attractive for its high yield, suitable nano-gap sizes and ease of fabrication in ambient conditions. Plasma etching of lithographically defined large area graphene allows for scalability of devices with precise control over the nano-gap position. We therefore decide to focus on developing graphene as the material of choice for building nano-electrodes by using a combination of feedback controlled electroburning and plasma etching, while also leveraging on the group's expertise in CVD growth of large area graphene.¹⁰⁹ Our fabrication approach will be extensively discussed in Chapter 2. The development of suitable nano-gaps is only the first step towards realisation of single-molecule devices. A thorough understanding of electron transport through

single-molecule transistors is necessary. In the next section, we briefly review electron transport through single-molecule transistors with particular focus on the weak coupling regime.

1.4 Electron Transport through Single-Molecule Transistors.

Transistors constitute the foundation of modern electronic circuits. The most basic concept is an electronic component with at least three terminals: source, drain and gate. Applying a voltage to the gate electrode regulates the current through the source-drain terminals when operated as an electrical switch. The output power can be higher than the input power which allows the transistor to function as an amplifier. While the switch and amplifier are the most common uses for a silicon transistor, the gate in a single-molecule transistor functions mostly as a spectroscopic tool. The gate electrode allows electrostatic tuning of molecular levels into and out of resonance with the Fermi level of the electrodes such that the excited energy spectrum can be obtained, which also serves as a molecular fingerprint. These excited states can be vibrational modes and in the limit of strong electron-vibron coupling, lead to phenomenon such as Franck-Condon blockade and avalanche transport (Chapter 4).

1.4.1 Three-terminal Devices

The gate electrode in a three-terminal device is electrically insulated from the source/drain electrodes and the molecule through a suitable insulating layer. The gate is therefore only capacitively coupled to the molecule and enables the tuning of the local electrostatic potential of the molecule with respect to the reservoirs. This shifts the molecular orbitals with respect to the Fermi level E_F of the electrodes. The total shift of the molecular orbitals is determined by the voltage applied to the gate electrode and quantified by the gate coupling parameter β , which should be as large as possible. The breakdown voltage of the insulating layer limits the maximum voltage that can be applied to the gate electrode. Maximising the product of β and the breakdown voltage maximises the total electrostatic potential tuning attainable. To increase β , thin insulators with high dielectric constant are

required. However, certain considerations need to be taken into account when decreasing the insulator thickness. Decreasing the insulator thickness decreases the breakdown voltage which limits the total electrostatic potential shift attainable in an experiment. Moreover, very thin insulating barriers (<nm) leads to gate leakage currents due to quantum tunnelling, which increases exponentially with decreasing insulator thickness. The gate leakage current obscures molecular features and so should be kept as low as possible. Therefore, the key challenge during device fabrication is the design of a junction geometry using suitable materials and insulator thickness which maximises the electrostatic potential tuning of the molecule while also minimising gate leakage current.

The two most frequently used gate materials are heavily doped silicon substrates with thermally grown silicon oxide on top and aluminium strips with a native oxide of a few nanometres.⁸³ In aluminium gates with a 3 nm thick oxide, the gate coupling is ~ 0.1 with a typical breakdown voltage of 4 V. In silicon devices with a 250 nm thick oxide layer the gate coupling is $\sim 10^{-3}$ with a breakdown voltage of 100 V. This translates to an energy range of about ± 0.4 eV and ± 0.1 eV over which the potential on the molecule can be varied for aluminium and silicon gates respectively. These reported values are for devices using Au nano-electrodes. As discussed previously, the presence of bulky Au electrodes limits β due to electrostatic screening. The use of graphene nano-electrodes can improve β and the tuneable electrostatic potential range, as will be discussed in Chapter 3 describing graphene-porphyrin single-molecule transistors.

In metals, the electrons are delocalised over collective states and described by band theory,¹¹⁰ which derives the electronic band structure through quantum mechanical wavefunctions of electrons in large periodic lattice of atoms or molecules. The dimensions of the metal can be reduced to a size such that quantization of the energy spectrum occurs, i.e. a set of discrete energy levels. Such a system is known as a quantum dot (QD).^{108,111} A molecular junction is typically viewed as a system with discrete and quantized energy levels coupled via tunnelling barriers to two electronic reservoirs characterized by filled energy

bands. Molecules can therefore be compared to QDs with much of the physics involved applicable to both. Charge carriers on the molecule are only allowed to populate these discrete energy levels, also known as molecular orbitals. The Pauli exclusion principle dictates that each orbital can only be filled by two electrons with opposite spin while the Aufbau principle determines the filling order, with electrons filling available orbitals with the lowest energy before filling those with higher energy. The highest(lowest) energy orbital that is occupied(unoccupied) is then defined as the highest(lowest) occupied(unoccupied) molecular orbital, also known as the HOMO(LUMO). The HOMO and LUMO are to molecules what the conduction and valence bands are for inorganic semiconductors. The energy difference between the HOMO and LUMO is known as the HOMO-LUMO gap Δ_{HL} . The small size of the molecule means that Coulombic interactions between charge carriers need to be taken into account and is quantified by the charging energy $E_C = e^2/2C$, where e is the electron charge and C the total capacitance of the molecule to the environment. C is given by the sum of the capacitances to the source, drain and gate, i.e. $C = C_S + C_D + C_G$. The energy required to add an extra electron, known as the addition energy, is $E_{add} = E_C + \delta E$, where δE is the energy spacing between two discrete levels. For electrons added to the same spin degenerate orbital, $\delta E = 0$ such that $E_{add} = E_C$. When electrons are added to a molecule with a fully occupied HOMO, $\delta E = \Delta_{HL}$ and $E_{add} = E_C + \Delta_{HL}$.

The source/drain electrodes act as electron reservoirs with a chemical potential equal to the Fermi energy E_F at 0 K. For temperatures $T > 0$ K, thermal broadening leads to the smearing of electron energies for which the distribution is given by the Fermi-Dirac distribution function:

$$f(\varepsilon) = \frac{1}{e^{\frac{\varepsilon - \mu}{k_B T}} + 1}, \quad (1)$$

where k_B is the Boltzmann constant, ε the electron energy, μ the chemical potential of the reservoir and T the temperature. In equilibrium, $\mu_S = \mu_D$ and no current flows between the

source and drain electrodes. The application of a bias voltage V_b shifts the chemical potential of the electrode:

$$\mu_S = E_F + eV_b, \quad (2)$$

$$\mu_D = E_F, \quad (3)$$

which leads to occupied(empty) states in the source(drain). The bias voltage applied therefore defines the energy range between the chemical potential of the source and drain electrodes and is commonly referred to as the bias window. When the electrodes are brought close to the molecule, the molecule couples to the source and drain electrodes via tunnelling barriers defined by the molecule-electrode coupling Γ_S, Γ_D . The molecule-electrode coupling describes the overlap between the wavefunction of the molecule with that of the conduction electrons of the electrodes and is related to the bare electron tunnelling rates between the molecular level and each electrode. Electrons tunnel onto and from the molecule with a finite probability. Heisenberg's energy uncertainty principle relates the finite window of tunnelling electron energies to the finite residence time of a tunnelling electron on the molecule, essentially describing the broadening of the molecular orbitals due to the wavefunction overlap. Depending on the ratio of $E_C, \Delta_{HL}, k_B T$ and the total molecule-electrode coupling $\Gamma = \Gamma_S + \Gamma_D$, three different transport regimes are distinguished: (i) strong coupling, (ii) weak coupling and (iii) intermediate coupling.

In the strong coupling regime where $\Gamma, k_B T > E_C, \Delta_{HL}$, the molecular states are strongly mixed with the wavefunction of the electrodes resulting in low tunnel barriers and significant level broadening. In the weak-coupling regime where $\Gamma \ll E_C, \Delta_{HL}, k_B T$, the molecular states are well separated from the electrode wavefunction and are described by a series of discrete levels with negligible level broadening. The tunnel barriers are high and charge transport proceeds via first order sequential charging. In the intermediate coupling regime where $\Gamma, k_B T \leq E_C, \Delta_{HL}$, the molecular and electrode wavefunctions are partially mixed. The tunnel barriers are lower and level broadening needs to be taken into account. The value of Γ

therefore determines the transport regime. We shall focus on the weak-coupling regime which is most relevant for our single-molecule devices where the molecule is bonded to graphene nano-electrodes via weak $\pi - \pi$ stacking interactions.

The electronic properties of systems in the weak-coupling regime are dominated by spatial confinement and Coulomb interactions. Charge transport in this regime is commonly described with the constant interaction model which is based on two assumptions.^{83,108} Firstly, a single constant capacitance $C = C_S + C_D + C_G$ can be used to parameterize the Coulomb interactions between electrons in the molecule and between electrons in the molecule and the environment. Secondly, the single particle energies are independent of Coulomb interactions and the number of electrons. The electron chemical potential μ of the molecule is then defined as the difference in the total energy of the system with and without an additional electron during transitions between states $|a\rangle$ and $|b\rangle$:

$$\mu_{a \leftrightarrow b}(N) \equiv U_b(N + 1) - U_a(N), \quad (4)$$

where $U(N)$ is the total energy of the molecule with N electrons. Electron transport through the molecule is dependent on the alignment of the chemical potentials of the molecule with those of the source and drain. Any chemical potential level involving the current molecular state which falls within the bias window results in sequential tunnelling. Electrons tunnel from the filled reservoir onto the molecule, and off to the empty reservoir in a two-step process where only a single electron tunnels across the molecule at any time. This is known as single-electron tunnelling (SET) or sequential transport.^{107,108}

Fig. 12 shows the schematic for sequential transport through the molecule. A potential V_b applied across the electrodes determines the bias window while the gate potential V_g electrostatically tunes the chemical potential levels of the molecule. In the low bias regime (Fig. 12a), transport can only occur when a charge transition between successive ground states (GS) of the molecule falls within the bias window, i.e. $\mu_S \geq \mu(N) \geq \mu_D$ for at least one N . If no such transition can occur, transport is blocked and the molecule is in Coulomb

blockade (CB). This is illustrated in Fig. 12c which shows a typical three terminal measurement where both the gate and bias voltages are swept to create a current map, commonly referred to as a charge stability diagram. Here, slopes separate regions of high conductance (red, blue) from the diamond shaped low conductance (white) Coulomb blocked regions, also known as Coulomb diamonds. Within each Coulomb diamond, the number of electrons N is fixed to an integer value. N increases(decreases) by 1 between adjacent Coulomb diamonds for increasing(decreasing) gate voltage. However, it is not trivial to determine the absolute value of N . The Coulomb diamond at zero bias and gate voltage may not correspond to the neutral charge state of the molecule as partial (dis)charging from charge traps in the dielectric or stabilisation of image charges can rearrange the level positions with respect to the Fermi energy of the electrodes.¹¹² The slopes of the Coulomb diamond edges correspond to the alignments of the chemical potential level of a GS state to GS state transition $\mu(N)$ with the Fermi energy of the source(negative slope) or the drain (positive slope) electrode (Fig. 12c (iv, v)). The crossing point of the slopes zero bias voltage is known as the charge degeneracy point where the molecule can be in either one of two redox states. The positive slope is $\alpha_+ = C_G/C_S$ and the negative slope $\alpha_- = -C_G/(C - C_S)$. The gate coupling $\beta = C_G/C$ can be determined from the slopes where $\beta = \frac{|\alpha_+||\alpha_-|}{|\alpha_+|+|\alpha_-|}$. The addition energy E_{add} is determined from the size of the diamond, where the height along the bias axis corresponds to E_{add}/e while the width along the gate axis corresponds to $E_{\text{add}}/\beta e$.

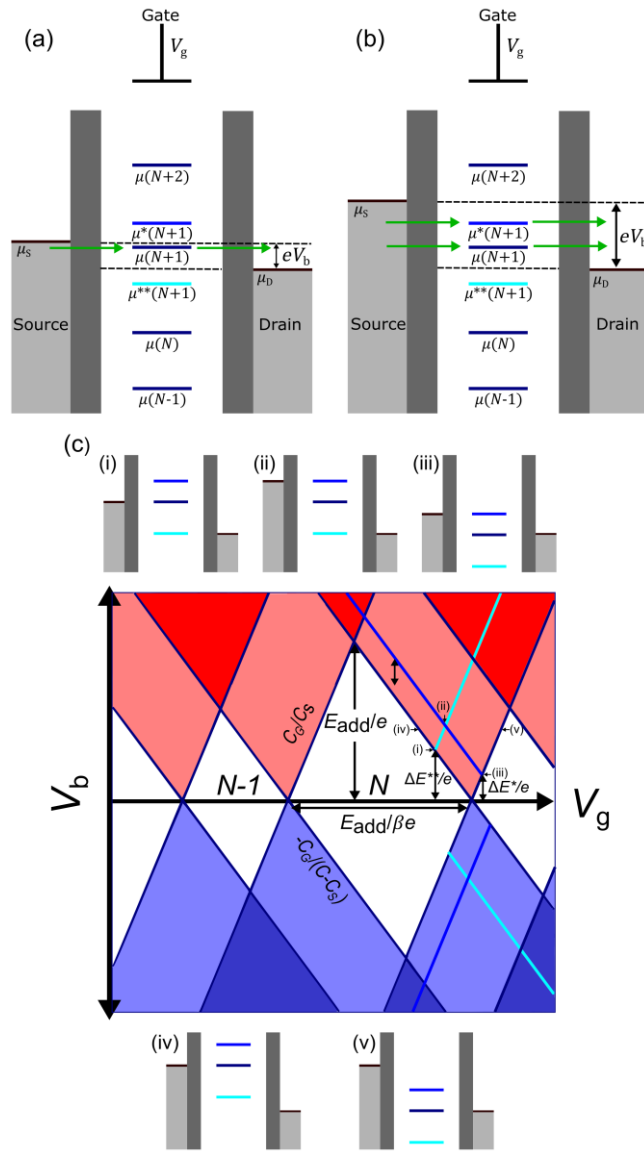


Figure 12 Schematic of single-electron transport. A potential V_b is applied across the source-drain electrodes while a gate potential V_g tunes the electrochemical potential levels of the molecule. For simplicity the drain is set to 0 V. (a) Low bias regime where single-electron tunnelling occurs through a single level. (b) High bias regime where excited state transitions participate in transport. (c) Schematic of a charge stability diagram for a molecule weakly coupled to the source and drain electrodes. Coloured regions indicate high conductance while white regions indicate Coulomb blockade where the number of electrons N remain fixed. Light shaded regions correspond to single-electron transport where a single GS chemical potential level lies within the bias window. Dark shaded regions correspond to two-electron transport where two GS chemical potential levels lie within the bias window. The addition energy E_{add} and gate coupling β can be extracted from the height and width of the Coulomb diamonds. The energy of excited state transitions ΔE^* , ΔE^{**} can be determined from the intersection of the excited state lines with the Coulomb diamond edges. (i-v) Schematics corresponding to the alignment of the electrochemical potential levels of the molecule with the Fermi levels of the leads.

Excited state (ES) transitions can also show up in the charge stability diagram. A simple schematic of the molecular orbital filling for GS and ES with redox states N and $N + 1$ is shown in Fig. 13a. Fig. 13b shows the corresponding energy level diagram and chemical potential ladder for different GS and ES transitions. In the high bias regime when the chemical potential level $\mu^*(N)$ involving an ES transition falls within the bias window, the number of electron tunnelling paths increases (Fig. 13b). This leads to a step increase in the current which shows up as lines running parallel to the diamond edges within the SET regime (Fig. 12c). The excited state energy ΔE^* is determined from the bias at which the excited state line intersects the Coulomb diamond edge. The intersection point corresponds to the case where the chemical potential levels of the GS to GS transition and the ES transitions are each aligned with the Fermi level of either the source or drain electrode (Fig. 13c (i, iii)). For ES state transitions terminating at the N -electron CB region (Fig. 12c (i)), the transition necessarily involves an N -electron excited state and is true for any N unless $N = 0$, in which case no lines terminate at the CB region since there are no excited states for $N = 0$. For transitions involving two excited states (not illustrated) the line terminates at the region where the energy level spacing is larger. Transitions between two excited states are dependent on the relative magnitude of the tunnel and relaxation rates. When the relaxation rate is larger than the tunnel rate, the molecule is effectively constantly in its ground state and such a transition does not occur. Visibility of excited state transitions therefore provides an insight to the relative magnitudes of the tunnel and relaxation rates.¹¹³

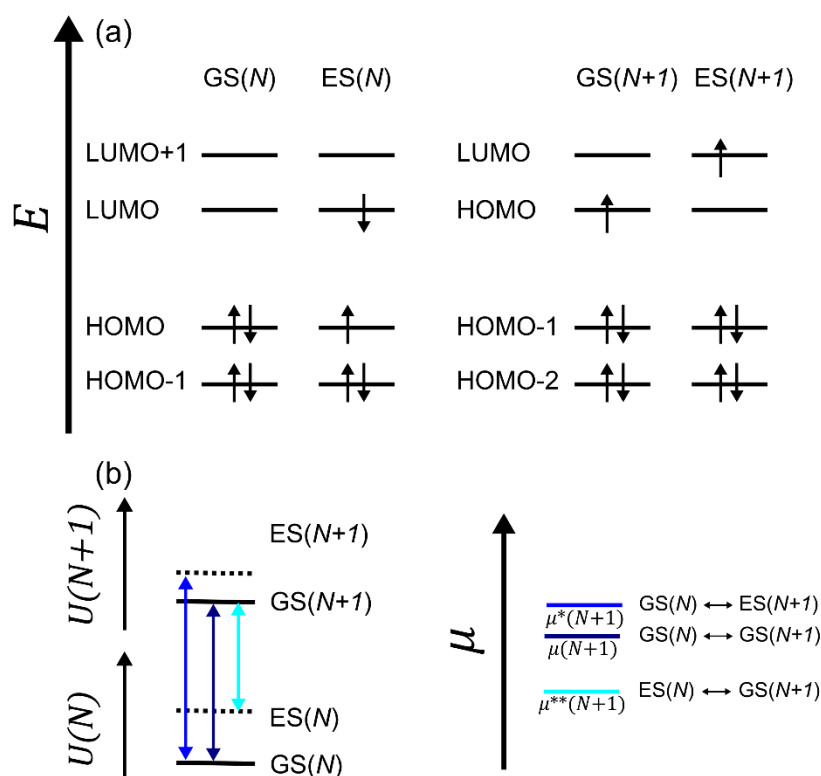


Figure 13 (a) A simple schematic of the molecular orbital filling for GS and ES with redox states N and $N+1$. Arrows indicate the electron spin state. (b) Corresponding energy level diagram and chemical potential level for different GS and ES transitions.

1.4.2 Conclusion

To fulfil the promise of single-molecule electronics, a number of important issues need to be addressed. Besides the chemical design of the molecular structures, the molecule-electrode interface must also be controlled as the molecule-electrode coupling Γ defines the transport regime.^{9,10,48,114} Nano-electrode separation is key as nano-gaps that are too large do not allow single molecules to bridge, while nano-gaps that are too small lead to ill-defined molecule-electrode coupling and steric conformations that affect charge transport. Variability in junction conductance has been partially addressed through a statistical approach that identifies the most stable molecular junction configurations. However, they cannot solve the reproducibility and control problems that is one of the most pressing obstacles in the field.

Another puzzling issue is the discrepancy between Δ_{HL} of the molecule in a junction and in the gas phase. Experiments frequently report values for molecules in a junction that

are an order of magnitude smaller than its gas phase value.^{19,115–118} X-ray and ultraviolet photoemission spectroscopy, Kelvin probe measurements and STM studies have shown that the formation of interfacial dipoles can result in substantial workfunction shifts that affect molecular orbitals.^{119–124} Strain in the molecular junction is also a possible factor.¹²⁵ Additionally, the combination of mechanical and electrostatic gate control has shown that image charge effects can cause a substantial reduction the addition energy.^{16,19,55,115,125} A point charge placed at a distance from a metal surface induces a polarization of surface charges such that the electric field outside the metal surface is due to both the actual charges as well as its mirror image. The mutual attraction lowers the energy of the system and reduces the HOMO-LUMO gap. However, DFT calculations cannot accurately capture the image charge effect to the non-local electron correlation.¹²⁶ Incorporation into first principle calculations is extremely computationally demanding and is only applicable for small molecules.^{127,128} Further theoretical efforts are required in order to properly model this effect.

Recent innovations in carbon based electrodes have proved particularly encouraging in addressing some of these issues. By moving away from Au electrodes and embracing the advantages offered by carbon based electrodes; high performance, stable, reproducible and diverse junctions are possible. Different types of chemical bonding have been demonstrated with carbon based electrodes.^{44,45,89,90,103} An especially promising approach of fault-tolerant designs using graphene electrodes is shown in Fig. 14.⁷

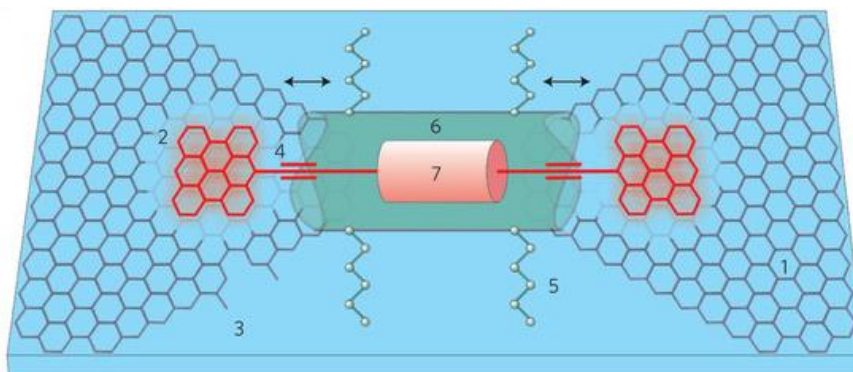


Figure 14 Schematic of a fault-tolerant design using graphene nano-electrodes consisting of large area hydrophobic single layer graphene (1) on a hydrophilic substrate. Large anchor groups (2) provide stable molecule-electrode contact. Edge defects (3) can be largely circumvented through the use of spacers (4) and cages (6). Self-alignment of the functional unit (7) of the molecule is achieved through the hydrophilic side groups (5). Reprinted with permission from [7], copyright (2013) Nature Publishing Group.

In this design based on modular buildings blocks, the junction is constrained to two dimensions thus limiting the number of bridging sites and reducing gate field screening. Large anchor groups form stable contacts by coupling the molecule to the defect-free region of the graphene electrode away from edge defects. In order to preserve the molecular identity, spacers or cages can be used to limit the overlap of molecular and electrode wavefunctions. Interactions between hydrophobic graphene, hydrophilic molecular side groups and the hydrophobic substrate can allow for the self-alignment of the system and prevent aggregation in order to obtain single molecule devices. The fabrication of such a device will be a key breakthrough in demonstrating nanoscale control over molecular devices. In the next chapter, we present the technique for fabricating graphene nano-electrodes using a combined approach of feedback controlled electroburning and lithographically defined plasma etching of large area CVD graphene. In Chapter 3, we demonstrate a single-molecule transistor architecture with a modular design connected to graphene nano-electrodes. Finally, we present excited states transport spectroscopy involving molecular vibrational modes in a graphene-C₆₀ single-molecule transistor in Chapter 4, before concluding this thesis with thoughts on challenges and future prospects in the field.

References

1. Moore, G. E. Cramming more components onto integrated circuits. *Proc. IEEE* **86**, 82–85 (1998).
2. Markov, I. L. Limits on fundamental limits to computation. *Nature* **512**, 147–154 (2014).
3. Song, H., Reed, M. a & Lee, T. Single molecule electronic devices. *Adv. Mater.* **23**, 1583–608 (2011).
4. Moth-Poulsen, K. & Bjørnholm, T. Molecular electronics with single molecules in solid-state devices. *Nat. Nanotechnol.* **4**, 551–6 (2009).
5. Son, J. Y. & Song, H. Molecular scale electronic devices using single molecules and molecular monolayers. *Curr. Appl. Phys.* **13**, 1157–1171 (2013).
6. Ratner, M. A brief history of molecular electronics. *Nat. Nanotechnol.* **8**, 378–81 (2013).
7. Lörtscher, E. Wiring molecules into circuits. *Nat. Nanotechnol.* **8**, 381–4 (2013).
8. Song, H., Kim, Y., Jeong, H., Reed, M. A. & Lee, T. Coherent Tunneling Transport in Molecular Junctions †. *J. Phys. Chem. C* **114**, 20431–20435 (2010).
9. Tao, N. J. Electron transport in molecular junctions. *Nat. Nanotechnol.* **1**, 173–81 (2006).
10. Hihath, J. & Tao, N. The role of molecule–electrode contact in single-molecule electronics. *Semicond. Sci. Technol.* **29**, 054007 (2014).
11. Akkerman, H. B. & de Boer, B. Electrical conduction through single molecules and self-assembled monolayers. *J. Phys. Condens. Matter* **20**, 013001 (2008).
12. Aviram, A. & Ratner, M. A. Molecular rectifiers. *Chem. Phys. Lett.* **29**, 277 (1974).
13. Díez-Pérez, I. *et al.* Rectification and stability of a single molecular diode with controlled orientation. *Nat. Chem.* **1**, 635–41 (2009).

14. Nerngchamnong, N. *et al.* The role of van der Waals forces in the performance of molecular diodes. *Nat. Nanotechnol.* **8**, 113–8 (2013).
15. Blum, A. S. *et al.* Molecularly inherent voltage-controlled conductance switching. *Nat. Mater.* **4**, 167–72 (2005).
16. Quek, S. Y. *et al.* Mechanically controlled binary conductance switching of a single-molecule junction. *Nat. Nanotechnol.* **4**, 230–4 (2009).
17. Chen, I. W. P. *et al.* Conductance and stochastic switching of ligand-supported linear chains of metal atoms. *Angew. Chemie - Int. Ed.* **45**, 5814–5818 (2006).
18. Jan van der Molen, S. & Liljeroth, P. Charge transport through molecular switches. *J. Phys. Condens. Matter* **22**, 133001 (2010).
19. Kubatkin, S. *et al.* Single-electron transistor of a single organic molecule with access to several redox states. *Nature* **425**, 698–701 (2003).
20. Song, H. *et al.* Observation of molecular orbital gating. *Nature* **462**, 1039–43 (2009).
21. Park, H. *et al.* Nanomechanical oscillations in a single-C₆₀ transistor. *Nature* **407**, 57–60 (2000).
22. Vincent, R., Klyatskaya, S., Ruben, M., Wernsdorfer, W. & Balestro, F. Electronic read-out of a single nuclear spin using a molecular spin transistor. *Nature* **488**, 357–60 (2012).
23. Kubatkin, S. *et al.* Single electron transistor with a single conjugated molecule. *Curr. Appl. Phys.* **4**, 554–558 (2004).
24. Lee, J., Chang, H., Kim, S., Bang, G. S. & Lee, H. Molecular monolayer nonvolatile memory with tunable molecules. *Angew. Chem. Int. Ed. Engl.* **48**, 8501–4 (2009).
25. Green, J. E. *et al.* A 160-kilobit molecular electronic memory patterned at 10(11) bits per square centimetre. *Nature* **445**, 414–7 (2007).

26. Xu, B. & Tao, N. J. Measurement of single-molecule resistance by repeated formation of molecular junctions. *Science* **301**, 1221–3 (2003).
27. Venkataraman, L., Klare, J. E., Nuckolls, C., Hybertsen, M. S. & Steigerwald, M. L. Dependence of single-molecule junction conductance on molecular conformation. *Nature* **442**, 904–7 (2006).
28. Tao, N. J. Measurement of Single Molecule Conductance: Benzenedithiol and Benzenedimethanethiol. *Nano Lett.* **4**, 267–271 (2004).
29. Chen, F., Li, X., Hihath, J., Huang, Z. & Tao, N. Effect of anchoring groups on single-molecule conductance: Comparative study of thiol-, amine-, and carboxylic-acid-terminated molecules. *J. Am. Chem. Soc.* **128**, 15874–15881 (2006).
30. Li, Z., Smeu, M., Ratner, M. A. & Borguet, E. Effect of anchoring groups on single molecule charge transport through porphyrins. *J. Phys. Chem. C* **117**, 14890–14898 (2013).
31. Taniguchi, M. *et al.* Dependence of single-molecule conductance on molecule junction symmetry. *J. Am. Chem. Soc.* **133**, 11426–9 (2011).
32. Tsutsui, M., Taniguchi, M. & Kawai, T. Quantitative evaluation of metal-molecule contact stability at the single-molecule level. *J. Am. Chem. Soc.* **131**, 10552–6 (2009).
33. Hines, T. *et al.* Transition from tunneling to hopping in single molecular junctions by measuring length and temperature dependence. **115**, 11658–11664 (2010).
34. Song, H., Lee, H. & Lee, T. Intermolecular chain-to-chain tunneling in metal–alkanethiol–metal junctions. *J. Am. Chem. Soc.* **129**, 3806–3807 (2007).
35. Wang, G., Kim, T., Jo, G. & Lee, T. Enhancement of Field Emission Transport by Molecular Tilt Configuration in Metal - Molecule - Metal Junctions. 5980–5985 (2009).
36. Son, K. -a., Kim, H. I. & Houston, J. E. Role of stress on charge transfer through self-

- assembled alkanethiol monolayers on Au. *Phys. Rev. Lett.* **86**, 5357–5360 (2001).
37. Rampi, M. A. & Whitesides, G. M. A versatile experimental approach for understanding electron transport through organic materials. *Chem. Phys.* **281**, 373–391 (2002).
 38. Rampi, M. A., Schueller, O. J. A. & Whitesides, G. M. Alkanethiol self-assembled monolayers as the dielectric of capacitors with nanoscale thickness. *Appl. Phys. Lett.* **72**, 1781–1783 (1998).
 39. Collier, C. P. A [2]catenane-based solid state electronically reconfigurable switch. *Science (80-.)*. **289**, 1172–1175 (2000).
 40. Kushmerick, J. G., Naciri, J., Yang, J. C. & Shashidhar, R. Conductance scaling of molecular wires in parallel. *Nano Lett.* **3**, 897–900 (2003).
 41. Kushmerick, J. G. *et al.* Metal-molecule contacts and charge transport across monomolecular layers: measurement and theory. *Phys. Rev. Lett.* **89**, 086802 (2002).
 42. Xiang, D., Jeong, H., Lee, T. & Mayer, D. Mechanically controllable break junctions for molecular electronics. *Adv. Mater.* **25**, 4845–4867 (2013).
 43. Park, H., Lim, A. K. L., Alivisatos, a. P., Park, J. & McEuen, P. L. Fabrication of metallic electrodes with nanometer separation by electromigration. *Appl. Phys. Lett.* **75**, 301 (1999).
 44. Guo, X. *et al.* Covalently bridging gaps in single-walled carbon nanotubes with conducting molecules. *Science* **311**, 356–9 (2006).
 45. Prins, F. *et al.* Room-temperature gating of molecular junctions using few-layer graphene nanogap electrodes. *Nano Lett.* **11**, 4607–11 (2011).
 46. Li, T., Hu, W. & Zhu, D. Nanogap electrodes. *Adv. Mater.* **22**, 286–300 (2010).
 47. Tsutsui, M. & Taniguchi, M. Single molecule electronics and devices. *Sensors (Basel)*. **12**, 7259–98 (2012).

48. Sen, A. & Kaun, C. C. Effect of electrode orientations on charge transport in alkanedithiol single-molecule junctions. *ACS Nano* **4**, 6404–6408 (2010).
49. Venkataraman, L. *et al.* Single-molecule circuits with well-defined molecular conductance. *Nano Lett.* **6**, 458–62 (2006).
50. Xiao, Xu & Tao. Conductance titration of single-peptide molecules. *J. Am. Chem. Soc.* **126**, 5370–5371 (2004).
51. He, J. *et al.* Electronic decay constant of carotenoid polyenes from single-molecule measurements. *J. Am. Chem. Soc.* **127**, 1384–1385 (2005).
52. Yamada, R., Kumazawa, H., Noutoshi, T., Tanaka, S. & Tada, H. Electrical conductance of oligothiophene molecular wires. *Nano Lett.* **8**, 1237–1240 (2008).
53. Choi, S. H. *et al.* Transition from tunneling to hopping transport in long, conjugated oligo-imine wires connected to metals. *J. Am. Chem. Soc.* **132**, 4358–4368 (2010).
54. Lu, Q. *et al.* From tunneling to hopping: A comprehensive investigation of charge transport mechanism in molecular junctions based on oligo(p-phenylene ethynylene)s. *ACS Nano* **3**, 3861–3868 (2009).
55. Park, J. *et al.* Coulomb blockade and the Kondo effect in single-atom transistors. *Nature* **417**, 722–5 (2002).
56. Wagner, S. *et al.* Switching of a coupled spin pair in a single-molecule junction. *Nat. Nanotechnol.* **8**, 575–9 (2013).
57. Moreland, J. & Ekin, J. W. Electron tunneling experiments using Nb-Sn ‘break’ junctions. *J. Appl. Phys.* **58**, 3888–3895 (1985).
58. Kergueris, C. *et al.* Electron transport through a metal-molecule-metal junction. *Phys. Rev. B* **59**, 12505–12513 (1999).
59. Lörtscher, E., Weber, H. B. & Riel, H. Statistical approach to investigating transport

- through single molecules. *Phys. Rev. Lett.* **98**, 176807 (2007).
60. Lörtscher, E., Cizek, J. W., Tour, J. & Riel, H. Reversible and controllable switching of a single-molecule junction. *Small* **2**, 973–7 (2006).
 61. Reed, M. A. Conductance of a molecular junction. *Science (80-.)*. **278**, 252–254 (1997).
 62. Galperin, M., Nitzan, A. & Ratner, M. Heat conduction in molecular transport junctions. *Phys. Rev. B* **75**, 155312 (2007).
 63. Chen, Y.-C., Zwolak, M. & Di Ventra, M. Local heating in nanoscale conductors. *Nano Lett.* **3**, 1691–1694 (2003).
 64. Champagne, A. R., Pasupathy, A. N. & Ralph, D. C. Mechanically adjustable and electrically gated single-molecule transistors. *Nano Lett.* **5**, 305–8 (2005).
 65. Martin, C. a, van Ruitenbeek, J. M. & van der Zant, H. S. J. Sandwich-type gated mechanical break junctions. *Nanotechnology* **21**, 265201 (2010).
 66. Xiang, D. *et al.* Three-terminal single-molecule junctions formed by mechanically controllable break junctions with side gating. *Nano Lett.* **13**, 2809–13 (2013).
 67. Black, J. R. Electron transport through single Mn₁₂ molecular magnets. *IEEE Trans. Electron Devices* **16**, 338–347 (1969).
 68. Ho, P. S. & Kwok, T. Electromigration in metals. *Rep. Prog. Phys.* **52**, 301 (1989).
 69. Brink, M. *et al.* Kondo resonance in a single-molecule transistor. *Nature* **417**, 725–9 (2002).
 70. Heersche, H. *et al.* Electron Transport through Single Mn₁₂ Molecular Magnets. *Phys. Rev. Lett.* **96**, 206801 (2006).
 71. Averin, D. V. & Likharev, K. K. Coulomb blockade of single-electron tunneling, and coherent oscillations in small tunnel junctions. *J. Low Temp. Phys.* **62**, 345–373 (1986).

72. Trouwborst, M. L., van der Molen, S. J. & van Wees, B. J. The role of Joule heating in the formation of nanogaps by electromigration. *J. Appl. Phys.* **99**, 114316 (2006).
73. Strachan, D. R. *et al.* Clean electromigrated nanogaps imaged by transmission electron microscopy. *Nano Lett.* **6**, 441–444 (2006).
74. Johnston, D. E., Strachan, D. R. & Johnson, a T. C. Parallel fabrication of nanogap electrodes. *Nano Lett.* **7**, 2774–7 (2007).
75. Basch, H., Cohen, R. & Ratner, M. A. Interface geometry and molecular junction conductance: Geometric fluctuation and stochastic switching. *Nano Lett.* **5**, 1668–1675 (2005).
76. Schull, G., Frederiksen, T., Arnau, A., Sánchez-Portal, D. & Berndt, R. Atomic-scale engineering of electrodes for single-molecule contacts. *Nat. Nanotechnol.* **6**, 23–7 (2011).
77. Tongay, S. *et al.* Stable hole doping of graphene for low electrical resistance and high optical transparency. *Nanotechnology* **22**, 425701 (2011).
78. Quek, S. Y. *et al.* Amine - Gold linked single-molecule circuits: Experiment and theory. *Nano Lett.* **7**, 3477–3482 (2007).
79. Néel, N., Kröger, J. & Berndt, R. Two-level conductance fluctuations of a single-molecule junction. *Nano Lett.* **11**, 3593–3596 (2011).
80. Salomon, A. *et al.* Comparison of electronic transport measurements on organic molecules. *Adv. Mater.* **15**, 1881–1890 (2003).
81. Datta, S., Strachan, D. & Johnson, a. Gate coupling to nanoscale electronics. *Phys. Rev. B* **79**, 205404 (2009).
82. Bai, J. *et al.* Top-gated chemical vapor deposition grown graphene transistors with current saturation. *Nano Lett.* **11**, 2555–2559 (2011).

83. Osorio, E. a, Bjørnholm, T., Lehn, J.-M., Ruben, M. & van der Zant, H. S. J. Single-molecule transport in three-terminal devices. *J. Phys. Condens. Matter* **20**, 374121 (2008).
84. Dhungana, K. B., Mandal, S. & Pati, R. Switching of conductance in a molecular wire: Role of junction geometry, interfacial distance, and conformational change. *J. Phys. Chem. C* **116**, 17268–17273 (2012).
85. Geim, A. K. & Novoselov, K. S. The rise of graphene. *Nat. Mater.* **6**, 183–191 (2007).
86. Avouris, P. Molecular electronics with carbon nanotubes. *Acc. Chem. Res.* **35**, 1026–1034 (2002).
87. Castro Neto, A. H. . *et al.* The electronic properties of graphene. *Rev. Mod. Phys.* **81**, 109–162 (2009).
88. Baringhaus, J. *et al.* Exceptional ballistic transport in epitaxial graphene nanoribbons. *Nature* **506**, 349–54 (2014).
89. Wei, D. *et al.* Real time and in situ control of the gap size of nanoelectrodes for molecular devices. *Nano Lett.* **8**, 1625–30 (2008).
90. Tsukagoshi, K., Yagi, I. & Aoyagi, Y. Pentacene nanotransistor with carbon nanotube electrodes. *Appl. Phys. Lett.* **85**, 1021–1023 (2004).
91. Moriyama, S. *et al.* Coupled quantum dots in a graphene-based two-dimensional semimetal. *Nano Lett.* **9**, 2891–2896 (2009).
92. Horiuchi, K. *et al.* Fabrication of nanoscale C₆₀ field-effect transistors with carbon nanotubes. *Appl. Phys. Lett.* **86**, 153108 (2005).
93. Huang, X. *et al.* Graphene-based materials: Synthesis, characterization, properties, and applications. *Small* **7**, 1876–902 (2011).
94. Lee, Y. *et al.* Wafer-scale synthesis and transfer of graphene films. *Nano Lett.* **10**, 490–

- 3 (2010).
95. Bae, S. *et al.* Roll-to-roll production of 30-inch graphene films for transparent electrodes. *Nat. Nanotechnol.* **5**, 574–578 (2010).
 96. Gao, L. *et al.* Face-to-face transfer of wafer-scale graphene films. *Nature* **505**, 190–4 (2014).
 97. Lee, J.-H. *et al.* Wafer-scale growth of single-crystal monolayer graphene on reusable hydrogen-terminated germanium. *Science (80-.)*. **344**, 286–289 (2014).
 98. Han, S.-J., Garcia, A. V., Oida, S., Jenkins, K. a & Haensch, W. Graphene radio frequency receiver integrated circuit. *Nat. Commun.* **5**, 3086 (2014).
 99. He, Y. *et al.* Graphene and graphene oxide nanogap electrodes fabricated by atomic force microscopy nanolithography. *Appl. Phys. Lett.* **97**, 133301 (2010).
 100. Campos, L. C., Manfrinato, V. R., Sanchez-Yamagishi, J. D., Kong, J. & Jarillo-Herrero, P. Anisotropic etching and nanoribbon formation in single-layer graphene. *Nano Lett.* **9**, 2600-4 (2009).
 101. Standley, B. *et al.* Graphene-based atomic-scale switches. *Nano Lett.* **8**, 3345–9 (2008).
 102. Wang, H. M. *et al.* Fabrication of graphene nanogap with crystallographically matching edges and its electron emission properties. *Appl. Phys. Lett.* **96**, 023106 (2010).
 103. Cao, Y. *et al.* Building high-throughput molecular junctions using indented graphene point contacts. *Angew. Chemie* **124**, 12394–12398 (2012).
 104. Nef, C. *et al.* High-yield fabrication of nm-size gaps in monolayer CVD graphene. *Nanoscale* **6**, 7249–54 (2014).
 105. Warner, J. H. *et al.* Structural transformations in graphene studied with high spatial and temporal resolution. *Nat. Nanotechnol.* **4**, 500–4 (2009).

106. Jin, C., Lan, H., Peng, L., Suenaga, K. & Iijima, S. Deriving carbon atomic chains from graphene. *Phys. Rev. Lett.* **102**, (2009).
107. Likharev, K. K. Single-electron devices and their applications. *Proc. IEEE* **87**, (1999).
108. Hanson, R. *et al.* Spins in few-electron quantum dots. *Rev. Mod. Phys.* **79**, 1217–1265 (2007).
109. Wu, Y. a *et al.* Large single crystals of graphene on melted copper using chemical vapor deposition. *ACS Nano* **6**, 5010–7 (2012).
110. Kittel, C. Introduction to solid state physics. *Solid State Physics* (2005).
111. Kouwenhoven, L. P., Austing, D. G. & Tarucha, S. Few-electron quantum dots. *Reports on Progress in Physics* **64**, 701–736 (2001).
112. Perrin, M. L., Burzurí, E. & van der Zant, H. S. J. Single-molecule transistors. *Chem. Soc. Rev.* **44**, 902–919 (2015).
113. Fujisawa, T., Austing, D. G., Tokura, Y., Hirayama, Y. & Tarucha, S. Allowed and forbidden transitions in artificial hydrogen and helium atoms. *Nature* **419**, 278–281 (2002).
114. Danilov, A. *et al.* Electronic transport in single molecule junctions: control of the molecule-electrode coupling through intramolecular tunneling barriers. *Nano Lett.* **8**, 1–5 (2008).
115. Perrin, M. L. *et al.* Large tunable image-charge effects in single-molecule junctions. *Nat. Nanotechnol.* **8**, 282–7 (2013).
116. Verzijl, C. J. O. *et al.* Image effects in transport at metal-molecule interfaces. *J. Chem. Phys.* **143**, (2015).
117. Neaton, J. B., Hybertsen, M. S. & Louie, S. G. Renormalization of molecular electronic levels at metal-molecule interfaces. *Phys. Rev. Lett.* **97**, (2006).

118. Kaasbjerg, K. & Flensberg, K. Strong polarization-induced reduction of addition energies in single-molecule nanojunctions. *Nano Lett.* **8**, 3809–14 (2008).
119. Ishii, H., Sugiyama, K., Ito, E. & Seki, K. Energy level alignment and interfacial electronic structures at organic/metal and organic/organic interfaces. *Adv. Mater.* **11**, 605 – 625 (1999).
120. Koch, N. Energy levels at interfaces between metals and conjugated organic molecules. *J. Phys. Condens. Matter* **20**, 184008 (2008).
121. Lange, I. *et al.* Band bending in conjugated polymer layers. *Phys. Rev. Lett.* **106**, (2011).
122. Braun, S., Salaneck, W. R. & Fahlman, M. Energy-level alignment at organic/metal and organic/organic interfaces. *Advanced Materials* **21**, 1450–1472 (2009).
123. Hwang, J., Wan, A. & Kahn, A. Energetics of metal-organic interfaces: New experiments and assessment of the field. *Materials Science and Engineering R: Reports* **64**, 1–31 (2009).
124. Otsuki, J. STM studies on porphyrins. *Coordination Chemistry Reviews* **254**, 2311–2341 (2010).
125. Bruot, C., Hihath, J. & Tao, N. Mechanically controlled molecular orbital alignment in single molecule junctions. *Nat. Nanotechnol.* **7**, 35–40 (2012).
126. Lambert, C. J. Basic concepts of quantum interference and electron transport in single-molecule electronics. *Chem. Soc. Rev.* **44**, 875–888 (2015).
127. Strange, M., Rostgaard, C., Häkkinen, H. & Thygesen, K. S. Self-consistent GW calculations of electronic transport in thiol- and amine-linked molecular junctions. *Phys. Rev. B - Condens. Matter Mater. Phys.* **83**, (2011).
128. Heimel, G. & Brédas, J.-L. Molecular electronics: Reflections on charge transport. *Nat. Nanotechnol.* **8**, 230–1 (2013).

Chapter 2: Nanoscale Control of Graphene Nano-Electrodes

2.1 Introduction

Recent studies report two distinct approaches towards the fabrication of graphene nano-electrodes for single-molecule junctions: electroburning^{1,2} and plasma etching.³ Electroburning relies on the current induced breakdown of graphene and the size of the nano-gaps are controlled by either varying the partial pressure of oxygen² or feedback control.¹ The fabrication yield of feedback controlled electroburning is high and allows for precise control over the gap sizes which are typically 1 – 2 nm. However, the positioning of nano-gaps is not well controlled due to the stochastic nature of the electroburning procedure. Plasma etching relies on over-etching lithographically defined patterns of CVD grown graphene point contacts. This approach can produce nano-gaps with sizes ≤ 1 nm. The use of large area CVD graphene enables scaling up through fabrication of nano-gaps arrays on the wafer scale with precise control over the positioning. The main drawback of this technique is the yield which is only 33%.

We combine the best of both techniques by developing a fabrication strategy based on these two approaches. This strategy utilises lithography with a minimum feature size of 200 nm for precise positioning of the nano-gap arrays. Feedback controlled electroburning is then employed for the high yield production of nano-electrodes with gap sizes 0.5 – 2.5 nm, suitable for contacting small molecules.⁴ We process a total of 1079 devices of which 776 are nano-gaps. The geometry of the nano-gaps is studied with atomic-force microscopy (AFM) and the nano-gap formation investigated by modelling the current density in our devices.

2.2 Fabrication

The graphene devices are fabricated through a passive-first active last process flow where the graphene is transferred onto a pre-patterned silicon chip as illustrated in Fig. 15(a-d). This passive first active last process reduces the number of lithography steps the graphene is exposed to. This produces cleaner devices and enables integration of graphene into

conventional silicon logic circuits.⁵ Single-layer graphene (SLG) is synthesized using a 1% CH₄:Ar gas mixture at atmospheric pressure on liquid copper in a 1 inch quartz tube CVD furnace at 1090 °C.⁶ The copper foil is placed on a tungsten support (99.8% purity 0.1 mm thick, Alfa Aesar) and annealed for 1 hour at 1060 °C and a further 30 mins at 1090 °C. Thereafter, graphene growth proceeds for 30 mins by switching on the CH₄. After rapid cooling to room temperature, PMMA is spun on the SLG/copper/tungsten stack. The tungsten support is removed by electrochemical etching in a 2 M sodium hydroxide solution with a 2.4 V voltage drop between the cathode and anode (sample). The copper is then etched away with a 0.1 M solution of ammonium persulfate. The remaining PMMA/SLG stack is rinsed in DI water and transferred onto the pre-patterned 1 × 1 cm² Si/SiO₂ chip (Fig. 15(a, b)) where the PMMA is removed with acetone. Each chip contains 540 pairs of 10/80 nm Cr/Au electrodes patterned with electron beam lithography and metal evaporation. We use a bi-layer PMMA recipe for the Cr/Au electrodes, where PMMA 495 A8 is first spun at 4500 rpm for 60s and baked at 180 °C for 90s before PMMA 950 A8 is spun and baked with the same parameters. The sample is exposed with a dose of 550 μC/cm² and developed in MIBK:IPA (1:3) solution for 45s. After metal deposition with a thermal evaporator, the lift off is performed in acetone overnight and then rinsed in IPA.

The SLG is next patterned into a 'bowtie' structure through negative resist electron beam lithography followed by oxygen plasma etching (Fig. 15(c, d)). We spin MaN-2405 negative resist onto the sample for 30 s at 3000 rpm and bake at 90 °C for 90 s. The sample is exposed with a dose of 160 μC/cm² and developed in ma-D525 solution for 150 s and rinsed in DI water for 10 mins. After plasma etching, the resist is removed with mr-REM 660 overnight followed by annealing at 350 °C in an Ar atmosphere for 1 hour.

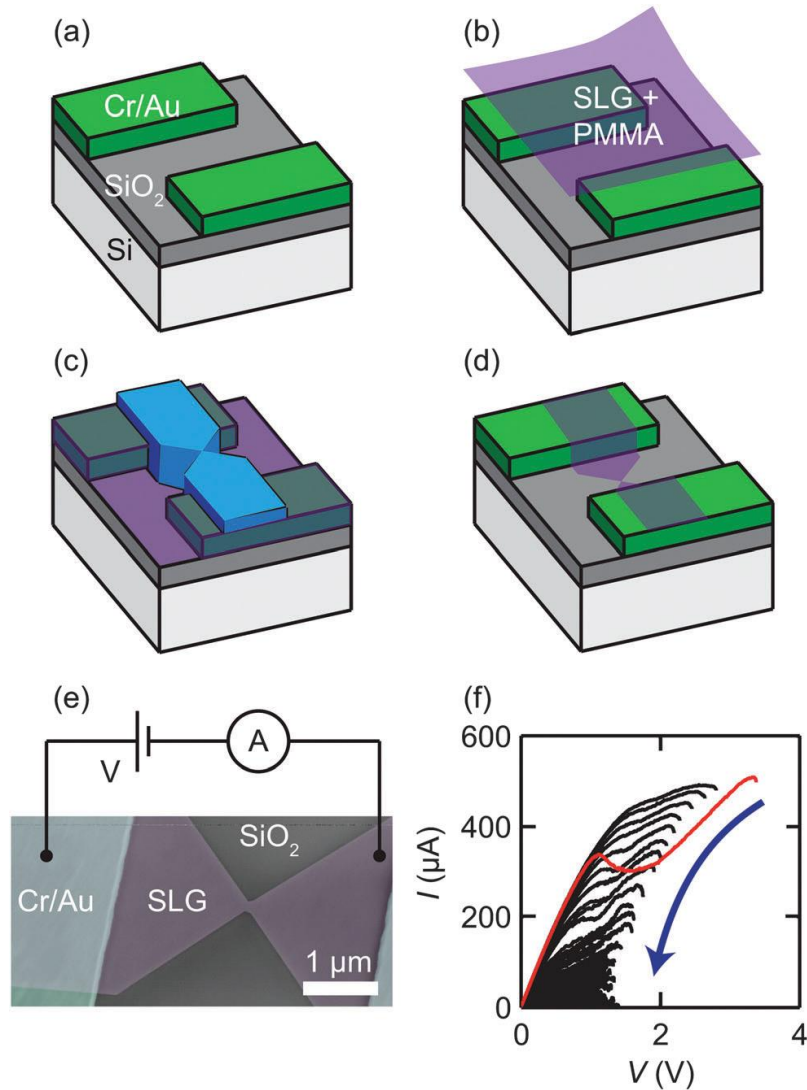


Figure 15 (a-d) Schematics of the device fabrication process flow. (e) Scanning electron micrograph of a patterned single layer graphene 'bowtie' device between two 10/80 nm Cr/Au contacts. (f) $I - V$ traces recorded during feedback controlled electroburning. The feedback conditions are $\Delta I_{\text{set}} = 6, 9, 12$ and $15 \mu\text{A}$ for $V_{\text{th}} \geq 1.9, 1.6, 1.3$ and 1.0 V respectively.

2.3 Nano-gap Characterization and Modelling

Fig. 15e shows a scanning electron micrograph of a SLG device lithographically patterned into a 'bowtie' structure between two Cr/Au electrodes. We perform the feedback controlled electroburning at room temperature in air using an automated MicroCascade probestation. The process starts by applying a voltage V across the SLG device which is ramped up at a rate of 0.75 Vs^{-1} while recording the current I with a $200 \mu\text{s}$ sampling rate. We set the feedback condition as a drop ΔI_{set} of the current within the last 15 mV. Upon meeting

this feedback condition, the voltage is quickly ramped down to zero at a rate of 225 Vs^{-1} . The low-bias resistance of the device is measured after each voltage ramp. The process repeats until this resistance exceeds R_{set} . In order to prevent the electroburning proceeding too abruptly, the feedback condition for each voltage ramp is adjusted depending on the threshold voltage V_{th} at which the previous feedback condition is met.

Fig. 15f shows the current-voltage ($I - V$) traces of a typical feedback controlled electroburning process. The first voltage ramp, represented by the red curve, shows a distinct region of negative differential conductance (NDC). NDC, or 'kinks' in the $I - V$ traces of single layer graphene devices are characteristic features of ambipolar transport.⁷ Graphene on SiO_2 is typically p-doped and holes are the majority carriers through the entire channel. As the source-drain voltage increases, the current begins to saturate as the electrochemical potential at the drain end of the channel moves towards the Dirac point. At a particular voltage V_{kink} , a pinch-off at the drain end occurs when the electrochemical potential there corresponds to the Dirac point.⁸ As V is increased beyond V_{kink} , the pinch-off moves through the channel until the carriers in the entire channel switch to electrons and the current increases again. V_{kink} is determined by the relative position of the Fermi levels from the Dirac point of the graphene electrodes, which is dependent on the doping level. We observe that V_{kink} shifts towards lower source-drain voltages with each electroburning voltage ramp and attribute this to the removal of residual resists. The removal of residual resists decreases the doping level and brings the Fermi level closer towards the Dirac point, corresponding to the shift of V_{kink} towards lower voltages. The change in conductance has similarly been observed in electroburning of few-layer graphene flakes and attributed to the removal of residual resist from Joule heating of the graphene.¹ Atomic force micrograph shows that graphene is much cleaner in the region around the narrowest point of the constriction compared to regions further away (Fig. 17(a, b)). This is an indication of the removal of residual resist from current annealing during the electroburning.

We next characterize the graphene nano-gaps by measuring low-bias current-voltage curves. Fig. 16a shows a typical $I - V$ trace of a nano-gap obtained after the electroburning process completes, i.e. when the low-bias resistance exceeds R_{set} which is typically 300 – 500 M Ω . Non-ohmic $I - V$ traces are characteristic of quantum tunnelling through a single tunnel barrier.⁹ The width and height of the tunnel barrier can be estimated by fitting the $I - V$ traces to the Simmons model where the current density j is described by equation (5), with the barrier height, width and asymmetry as fitting parameters:^{1,9}

$$j = \frac{4\pi m_e e}{h^3} \int_0^\infty [f_L(\varepsilon) - f_R(\varepsilon)] d\varepsilon \int_0^\varepsilon T(\varepsilon_x) d\varepsilon_x, \quad (5)$$

where m_e is the electron mass, e is the electron charge, h is the Planck constant, $T(\varepsilon_x)$ is the transmission function describing the tunnel probability of an electron with energy ε_x moving in the x -direction and $f_{L/R}(\varepsilon)$ is the Fermi-Dirac distribution of the left/right leads. $T(\varepsilon_x)$ is given by the WKB approximation for a barrier potential $\phi(x)$:

$$T(\varepsilon_x) = e^{-\frac{8m_e\pi}{h} \int_{x_1}^{x_2} [(\phi(x) - \varepsilon_x)]^{\frac{1}{2}} dx}, \quad (6)$$

assuming a barrier with constant height independent of x ,

$$T(\varepsilon_x) = e^{-\frac{8m_e\pi}{h} d \sqrt{\phi - \varepsilon_x}}, \quad (7)$$

where the barrier width $d = x_2 - x_1$. We fit the current $I(V)$ to eqn (5) with the average barrier height $\phi = \phi_L + \phi_R$, asymmetry factor $\alpha = \frac{\phi_L - \phi_R}{\phi_L + \phi_R}$, gap size d and a prefactor A that takes into account the cross-section of the junction as fitting parameters. When the work function on the left electrode ϕ_L equals that on the right, j becomes:

$$j \approx \frac{e}{2\pi h d^2} \left[(\phi - \mu_L) e^{-\frac{4\pi d \sqrt{2m(\phi - \mu_L)}}{h}} - (\phi - \mu_R) e^{-\frac{4\pi d \sqrt{2m(\phi - \mu_R)}}{h}} \right], \quad (8)$$

when they are different, for $\varepsilon_x < \phi_L, \phi_R$,

$$\int_{x_1}^{x_2} [(\phi(x) - \varepsilon_x)]^{\frac{1}{2}} dx = \frac{2}{3} d \frac{((\phi_R - \varepsilon_x)^{\frac{3}{2}} - (\phi_L - \varepsilon_x)^{\frac{3}{2}})}{\phi_R - \phi_L}, \quad (9)$$

and for $\phi_{L/R} < \varepsilon_x < \phi_{R/L}$,

$$\int_{x_1}^{x_2} [(\phi(x) - \varepsilon_x)]^{\frac{1}{2}} dx = \frac{2}{3} d \frac{(\phi_{R/L} - \varepsilon_x)^{\frac{3}{2}}}{\phi_{R/L} - \phi_{L/R}}. \quad (10)$$

To investigate the control and reproducibility of the fabrication process, 307 devices are fitted to the Simmons model. The mean nano-gap size d of 140 devices with $R_{\text{set}} = 300 \text{ M}\Omega$ is $d = 1.42 \pm 0.56 \text{ nm}$. The mean nano-gap size d of 167 devices with $R_{\text{set}} = 500 \text{ M}\Omega$ is $d = 1.39 \pm 0.46 \text{ nm}$. In addition, 94.8% of 307 devices fitted return a nano-gap size of $0.5 \leq d \leq 2.5 \text{ nm}$, which make these graphene nano-gaps suitable for contacting single-molecules. The mean barrier height fitted is $0.24 \pm 0.11 \text{ eV}$, comparable to the values obtained in electromigrated metal electrodes¹⁰ and electroburnt few-layer graphene nano-gaps.¹ Fig. 16d shows the plot of ϕ vs d for the 167 devices with $R_{\text{set}} = 500 \text{ M}\Omega$. While the overall spread of the data is broad, there is a bunching of the data points in the middle of the plot which suggest a linear correlation between the barrier height and the gap size. The Pearson coefficient $p_{\phi,d} = \frac{\text{cov}(\phi,d)}{\sigma_{\phi}\sigma_d}$, where $\text{cov}(\phi,d)$ is the covariance and σ is the standard deviation, measures the linear dependence between ϕ and d and has a value between -1 and +1. A value of 1 indicates total positive linear correlation, 0 no linear correlation and -1 total negative linear correlation. We calculate that $p_{\phi,d} = 0.12$, suggesting a very weak linear dependence between ϕ and d where larger gaps correspond with larger barrier heights.

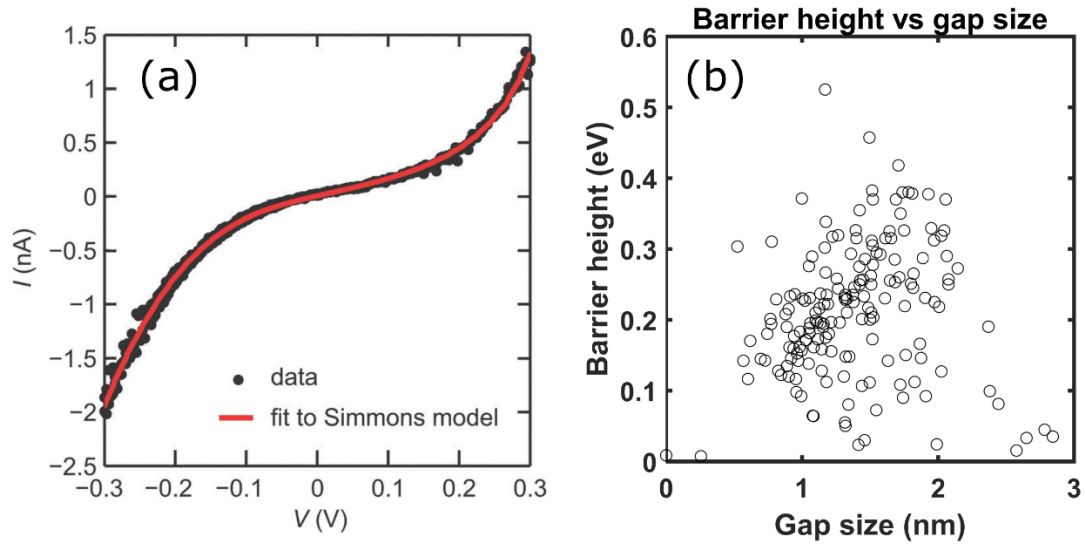


Figure 16 (a) Typical I - V trace of a SLG nano-gap. The I - V trace is fitted to the Simmons model for tunnelling through a single trapezoidal barrier with the fitting parameters: barrier height $\phi = 0.26$ eV; barrier width (gap-size) $d = 1.50 \pm 0.03$ nm; and barrier asymmetry $\alpha = -0.89 \pm 0.05$. (b) Plot of barrier height ϕ vs gap size d for 167 devices with $R_{\text{set}} = 500$ M Ω .

We next perform atomic force microscopy (AFM) on several nano-gaps. Fig. 17(a, b) shows AFM images of an electroburnt nano-gap. The images reveal that the nano-gap forms at the narrowest part of the constriction. This can be understood by considering that the current density and therefore the Joule heating will be the largest at this region. We determine the breakdown current I_{BD} as the current at which the feedback condition is met for the first voltage ramp. $I_{\text{BD}} = 310$ μA for the device shown in Fig. 17(a, b), corresponding to a current density $j = 4.7 \times 10^8$ Acm^{-2} assuming a graphene van der Waals thickness of 0.355 nm. This is comparable to breakdown current densities of $j \approx 5 \times 10^8$ Acm^{-2} reported for mechanically exfoliated SLG.¹¹ For 1079 devices, we find a mean $I_{\text{BD}} = 324 \pm 63$ μA .

It has been previously suggested that the electroburning process is based on thermally activated reaction between carbon atoms and oxygen due to the fact that the nano-gap formation in graphene flakes takes place furthest from the metal electrodes, where the temperature due to Joule heating is highest. This is consistent with our observation that the nano-gaps form at the point where the current density, and therefore the Joule heating is

maximum. The nano-gap formation is expected to occur at the graphene edges due to the higher reactivity of edge carbon atoms from incomplete sp^2 -hybridisation.^{12,13} From the AFM images in Fig. 17(a, b), we observe that the formation of the nano-gap proceeds via a crack developing across the narrowest part of the graphene constriction instead of a gradual narrowing of the entire region.

The evolution of the nano-gap formation is investigated by calculating the current density profile in the graphene 'bowtie' structure. The current density ($j(r) \propto \nabla V(r)$, where $V(r)$ is the potential) as a function of the position r is calculated by solving the Laplace equation $\nabla^2 V(r) = 0$ using conformal mapping with a Schwarz transformation.^{4,14} The calculated current density profiles for a graphene 'bowtie' structure before electroburning (Fig. 17c) and for a partially formed nano-gap (Fig. 17d) are shown. The current density is highest at the apex of the constriction (Fig. 17c), consistent with where we experimentally observe the formation of the nano-gap. The calculated current density profile (Fig. 17d) shows that the current flows around a crack extending from the apexes of the constriction resulting in a hotspot at the crack-tip where the current density is highest. Once a crack forms at the apex, it is expected to propagate across the constriction, rather than becoming wider. Our calculations and experimental findings demonstrate that we are able to control the position of the nano-gaps, allowing for precise alignment with other lithographically defined features.

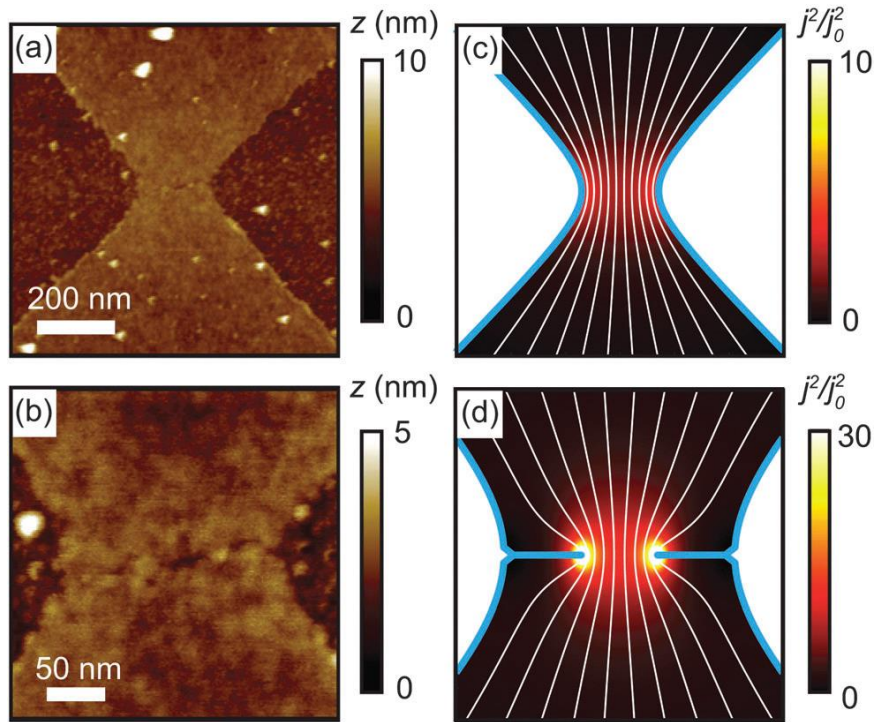


Figure 17 (a, b) AFM images of a typical graphene nano-gap. Light areas are graphene and dark areas are the SiO₂ substrate. A crack across the narrowest region of the constriction can be observed. Close to the crack, the graphene is much cleaner compared to regions further away due to the removal of residual resist from current annealing. Calculated current density profile for a graphene 'bowtie' structure (c) and a partially formed nano-gap (d). The thick solid blue lines outline the device geometry while the narrow stream white lines indicate the current flow. The current flows around the cracks extending across the graphene constriction resulting in a current 'hotspot' around the crack-tip.

An overview of the electroburning process for a total of 1079 devices on 5 chips is given in Table 1. There are three ways in which the electroburning process can fail: (i) I_{BD} is larger than the maximum current that the voltage source can supply; (ii) the voltage ramp back to zero upon meeting the feedback condition is too slow, leading to thermal runaway and a device with infinite resistance ($>100 \text{ G}\Omega$); (iii) the feedback condition is too sensitive and ramps the voltage back to zero before the current reaches I_{BD} . As (i) is not intrinsic to the electroburning process but related to a lithographically defined constriction that is too wide, we define the yield of the electroburning by only considering devices where the threshold current is within the range of our experimental setup. We find that the yield of the electroburning process is 85% while the total fabrication yield is 71%.

	Number of devices
Devices before electroburning	1079
Threshold current too high	167
Feedback not fast enough	67
Feedback too sensitive	69
Nano-gaps after electroburning	776

Table 1 Fabrication yield of the feedback controlled electroburning process.

2.4 Conclusion

We have demonstrated scalable fabrication of CVD graphene nano-gaps with a yield of 71% by combining conventional lithographically defined plasma etching and feedback controlled-electroburning. Our AFM images and current density profile calculations show that the nano-gaps are formed across the narrowest part of the graphene ‘bowtie’ structure. By fitting the $I - V$ data, we determined for 94.8% of 307 devices a gap size of 0.5 – 2.5 nm. The use of CVD graphene means that the technique is scalable using wafer-scale grown graphene, while the passive-first active-last process adopted enables integration with conventional silicon CMOS process. Most importantly, the ability to controllably fabricate and position nano-gaps of this size range allows for the possibility of building single-molecule transistors, which we discuss in the subsequent chapters.

References

1. Prins, F. *et al.* Room-temperature gating of molecular junctions using few-layer graphene nanogap electrodes. *Nano Lett.* **11**, 4607–11 (2011).
2. Nef, C. *et al.* High-yield fabrication of nm-size gaps in monolayer CVD graphene. *Nanoscale* **6**, 7249–54 (2014).
3. Cao, Y. *et al.* Building high-throughput molecular junctions using indented graphene point contacts. *Angew. Chemie* **124**, 12394–12398 (2012).
4. Lau, C. S., Mol, J. A., Warner, J. H. & Briggs, G. A. D. Nanoscale control of graphene electrodes. *Phys. Chem. Chem. Phys.* **16**, 20398–401 (2014).
5. Han, S.-J., Garcia, A. V., Oida, S., Jenkins, K. a & Haensch, W. Graphene radio frequency receiver integrated circuit. *Nat. Commun.* **5**, 3086 (2014).
6. Wu, Y. a *et al.* Large single crystals of graphene on melted copper using chemical vapor deposition. *ACS Nano* **6**, 5010–7 (2012).
7. Meric, I. *et al.* Current saturation in zero-bandgap, top-gated graphene field-effect transistors. *Nat. Nanotechnol.* **3**, 654–9 (2008).
8. Castro Neto, A. H. . *et al.* The electronic properties of graphene. *Rev. Mod. Phys.* **81**, 109–162 (2009).
9. Simmons, J. G. Generalized formula for the electric tunnel effect between similar electrodes separated by a thin insulating Film. *J. Appl. Phys.* **34**, 1793 (1963).
10. Mangin, A., Anthore, A., Della Rocca, M. L., Boulat, E. & Lafarge, P. Reduced work functions in gold electromigrated nanogaps. *Phys. Rev. B - Condens. Matter Mater. Phys.* **80**, (2009).
11. Standley, B. *et al.* Graphene-based atomic-scale switches. *Nano Lett.* **8**, 3345–9 (2008).

12. Warner, J. H. *et al.* Structural transformations in graphene studied with high spatial and temporal resolution. *Nat. Nanotechnol.* **4**, 500–4 (2009).
13. Jin, C., Lan, H., Peng, L., Suenaga, K. & Iijima, S. Deriving carbon atomic chains from graphene. *Phys. Rev. Lett.* **102**, (2009).
14. Lodge, K. W. & Briggs, G. A. D. The potential drop across an imperfect diffusion bond. *J. Mater. Sci.* **18**, 2354–2360, (1983).

Chapter 3: Graphene-Porphyrin Single-Molecule Transistor

3.1 Introduction

Having established a reliable technique for fabricating graphene nano-gaps suitable for contacting single molecules, we next demonstrate a robust graphene nano-electrodes based single-molecule transistor using a single porphyrin molecule. We observe remarkably reproducible single-electron charging which we attribute to the insensitivity of the molecular junction to the atomic configuration of the graphene electrodes. In addition, the stability and reduced electrostatic screening afforded by the graphene electrodes allow for high-bias transport spectroscopy and the observation of multiple redox states at room temperature.

We achieve stable and reproducible single-molecule single-electron transistor (SET) architecture through controlled fabrication of graphene nano-gaps and careful molecular design. The use of graphene nano-electrodes and modular molecules consisting of a ligand backbone with specific side groups for anchoring, spacing and self-alignment, have been proposed to overcome variability issues that hindered the development of single-molecule electronics.^{1,2} Although orbital gating of small molecules anchored to graphene electrodes has been demonstrated,³ studies of charge transport through complex modular molecules anchored to graphene electrodes are lacking. Porphyrins are a widely studied class of molecules which provide a versatile platform for the design of molecular device functionalities.⁴⁻⁷ We therefore commit to investigating single porphyrin molecules anchored to graphene nano-electrodes through $\pi - \pi$ stacking interactions³ which preserves the electronic structure of the molecule,⁸ in contrast to thiol anchors to gold electrodes that introduce gap-type states.⁹

3.2 Experimental Setup

The porphyrin molecule studied is shown in Fig. 18a. It comprises a zinc-porphyrin backbone (black) with tetrabenzofluorene (TBF) 'butterfly' anchors (green) and two bulky side groups (red). TBF 'butterfly' anchor groups are known to bind strongly to graphite surfaces¹⁰

as well as being robust in solvent solution,¹¹ requirements for molecular deposition via solution. Density functional theory (DFT) calculations indicate that the porphyrin molecule relaxes across the graphene nano-gap in a planar geometry with no steric hindrance (Fig. 18b). The wavefunction of the HOMO delocalises over the porphyrin backbone and anchor groups allowing for electron transport through the fully conjugated porphyrin molecule. In contrast, the wavefunction of the LUMO is only localised over the porphyrin backbone, as revealed by DFT calculations in Fig. 18c. The porphyrin backbone is separated from the TBF 'butterfly' anchor groups by a spacer (blue) allowing the anchors to bind to the graphene plane via $\pi - \pi$ stacking rather than to the graphene edges which are expected to contain significantly more defects. The bulky side groups (red) prevent the central porphyrin from binding to the graphene electrodes as well as increasing the solubility of the molecule.

We use graphene nano-electrodes fabricated using the technique described in Chapter 2 to contact the porphyrin molecule. The chemical potential of the molecule can be electrostatically tuned using the conducting silicon substrate as a back-gate (Fig. 18b), which is separated from the molecule and graphene nano-electrodes by a 300 nm thick silicon oxide layer. We deposit the molecules from a chloroform solution, after which the samples are immediately transferred into vacuum to minimise contamination. For cryogenic measurements, the sample are transferred to an Oxford Instruments Triton dilution fridge. The current-voltage ($I - V$) traces of the device measured at 4 K before (blue) and after (red) molecular deposition is shown in Fig. 18d. A scanning electron micrograph of the device is shown in the inset of Fig. 18d. Prior to deposition, the $I - V$ trace displays smooth exponential behaviour characteristic of tunnelling across a nano-gap. The presence of a molecule leads to steps in the $I - V$ trace as expected for sequential single-electron tunnelling through a double barrier system.

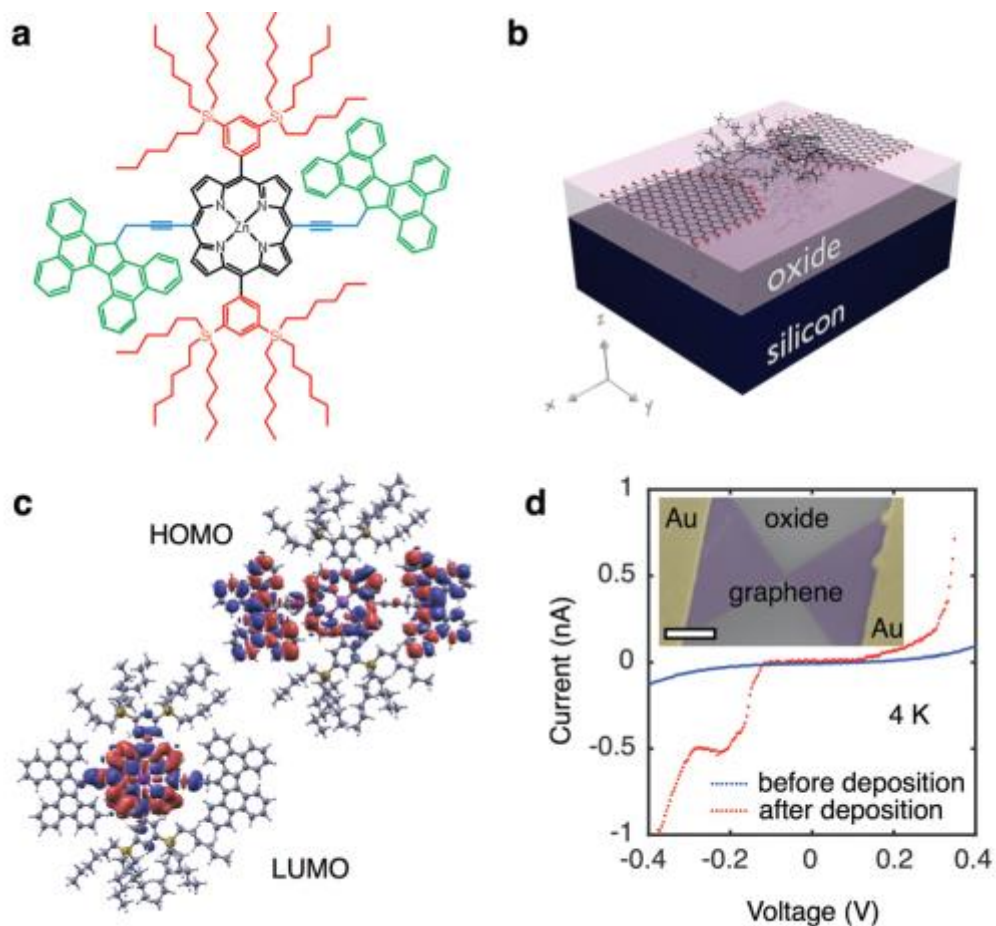


Figure 18 (a) Chemical structure of the molecule with a zinc-porphyrin backbone (black), TBF 'butterfly' anchor groups (green) and bulky side groups (red). The side groups provide different functionalities as discussed in the text. (b) Schematic of the single-molecule transistor. The device is separated from the heavily doped silicon substrate, which serves as a back-gate, by a 300 nm silicon oxide layer. (c) DFT simulations of the local density of states (LDOS) for HOMO and LUMO iso-surfaces. (d) Typical $I - V$ traces before (blue) and after (red) molecular deposition. The inset shows a false colour scanning electron micrograph of the device. The scale bar is 1 μm .

3.3 Transport Spectroscopy

Transport spectroscopy shows reproducible single-electron transport in our devices, where single-electron charging is determined mainly by the molecule rather than atomistic details of the graphene nano-electrodes. We observe reproducible SET behaviour in 10 of 48 devices measured at 20 mK. Fig. 19 shows the current stability diagram I measured as a function of the bias voltage V_b and the gate voltage V_g for these 10 devices. Similar addition energies E_{add} for the Coulomb diamond closest to zero gate voltage are observed for all 10

devices. The mean addition energy is $E_{\text{add}} = 370 \pm 50$ meV, as measured from the height of the Coulomb diamonds. Device statistics are presented in Table 2. Statistics for the control experiment where 20 devices are measured using the same porphyrin molecule but without the TBF ‘butterfly’ anchor groups are also included. No Coulomb diamonds are observed for these 20 devices. We therefore deduce based on the reproducibility of the addition energies and the control experiment the following: (i) porphyrin molecules attach to the electrodes only when they are functionalised with TBF ‘butterfly’ anchor groups; (ii) the observed SET behaviour for the 10 devices in Fig. 19 can be attributed to a molecule bridging the graphene nano-gap and; (iii) cannot be attributed to multiple molecules or random carbon islands. The presence of multiple molecules would lead to Coulomb shards caused by multiple overlapping Coulomb diamonds whereas carbon islands with random sizes are expected to result in more variable addition energies.^{12,13} Observing similar $E_{\text{add}} \sim 370$ meV for 10 out of 12 of the devices displaying Coulomb diamonds suggests that there is only one active molecule for these 10 devices.

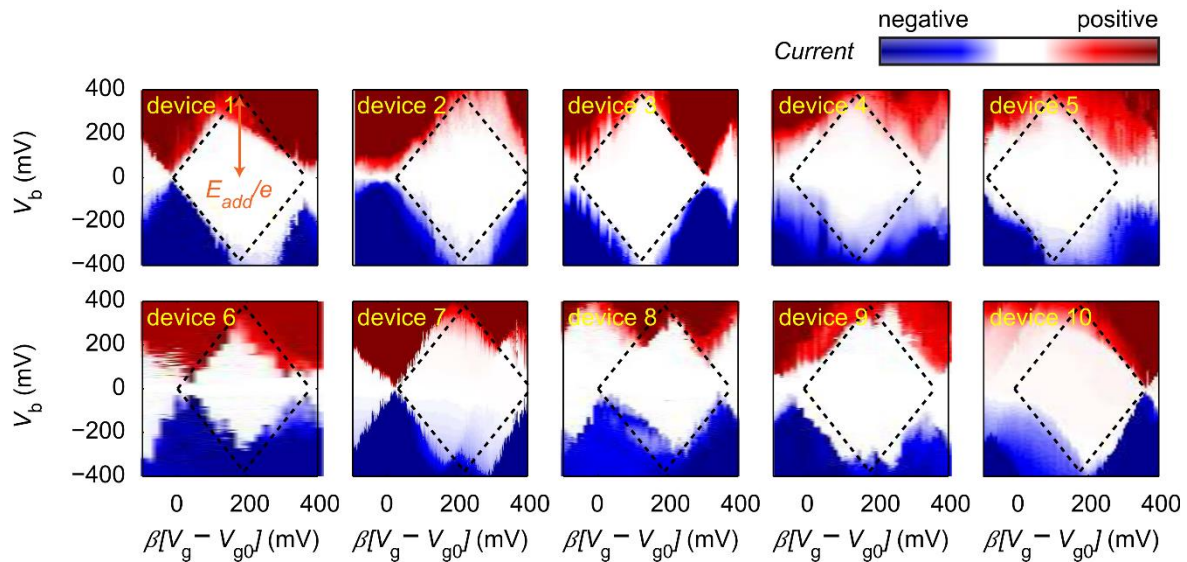


Figure 19 Current stability diagram for 10 devices. Sequential electron tunnelling leads to diamond shaped regions where charge transport is Coulomb blocked. All devices are measured at 20 mK.

	$E_{\text{add}} < 100 \text{ meV}$	$E_{\text{add}} \sim 370 \text{ meV}$	No Coulomb diamonds
TBF anchors	2	10	36
No anchors	0	0	20

Table 2 Statistics of 68 devices measured at 20 mK. For devices assigned to the column 'No Coulomb diamonds', we did not observe any Coulomb peaks at low bias (10 mV), indicating either no formation of quantum dots or the addition energy of the quantum dot exceeds our gate range. ($E_{\text{add}} > 800 \text{ meV}$ for a gate coupling $\beta = 0.01$)

The horizontal axes in Fig. 19 are offset by a value V_{g0} and scaled by the effective gate coupling β which measures the capacitive coupling between the gate and the molecule and relates the shift in gate voltage to the shift in the chemical potential of the molecule. We find a mean β value of $\beta_{\text{mean}} = 0.01$, estimated from the slopes of the Coulomb diamond edges. This measured value for our devices with graphene nano-electrodes sitting on a 300 nm thick silicon oxide is almost an order of magnitude higher than reported values of $\sim 10^{-3}$ for single-molecule junctions with gold nano-electrodes on a thinner 250 nm thick SiO_2 .¹⁴ The improved gate coupling is attributed to the reduced electrostatic screening by the two dimensional graphene nano-electrodes compared to bulky gold nano-electrodes and allows the observation of multiple redox states in our devices.

Although the single-electron charging behaviour for the devices is similar, a degree of variability is still present in the devices. The gate coupling β ranges from 0.006 – 0.04. The small value of β indicates that the total capacitance is dominated by the source and drain electrodes. There are also significant differences in the current through the single-molecule devices. The variation in β can be attributed to difference in screening of the gate-field by the source and drain electrodes. Trap states in the form of defects in the oxide layer which capture mobile charge carriers; and adsorbents on the graphene electrodes which changes the doping level can lead to variations in the electrostatic environment between devices. This variation is manifested in the transport measurements as shifted and non-closing Coulomb diamonds with different values of V_{g0} . Doping level variations of graphene, and therefore the local densities of states, leads to differences in the current through the device. Inconsistencies in overlap between the TBF 'butterfly' anchor groups and the graphene nano-electrodes also contributes to the current variation. DFT calculations of the relaxed geometry shows that the TBF 'butterfly' anchors are not completely flat and its configuration on top of the graphene nano-electrodes

differs for the source and drain contacts (Fig. 18b). Table 3 reports the values of E_{add} , β and V_{g0} for all 10 devices.

Device	E_{add} (meV)	β	V_{g0} (V)
1	440	7.4×10^{-3}	14
2	440	6.1×10^{-3}	25
3	350	6.5×10^{-3}	25
4	390	8.6×10^{-3}	15
5	380	7.7×10^{-3}	27
6	290	3.9×10^{-2}	0
7	390	8.5×10^{-3}	15
8	310	1.9×10^{-2}	12
9	340	1.6×10^{-2}	12
10	360	9.3×10^{-3}	22

Table 3 E_{add} , β and V_{g0} for the 10 devices shown in Fig. 19

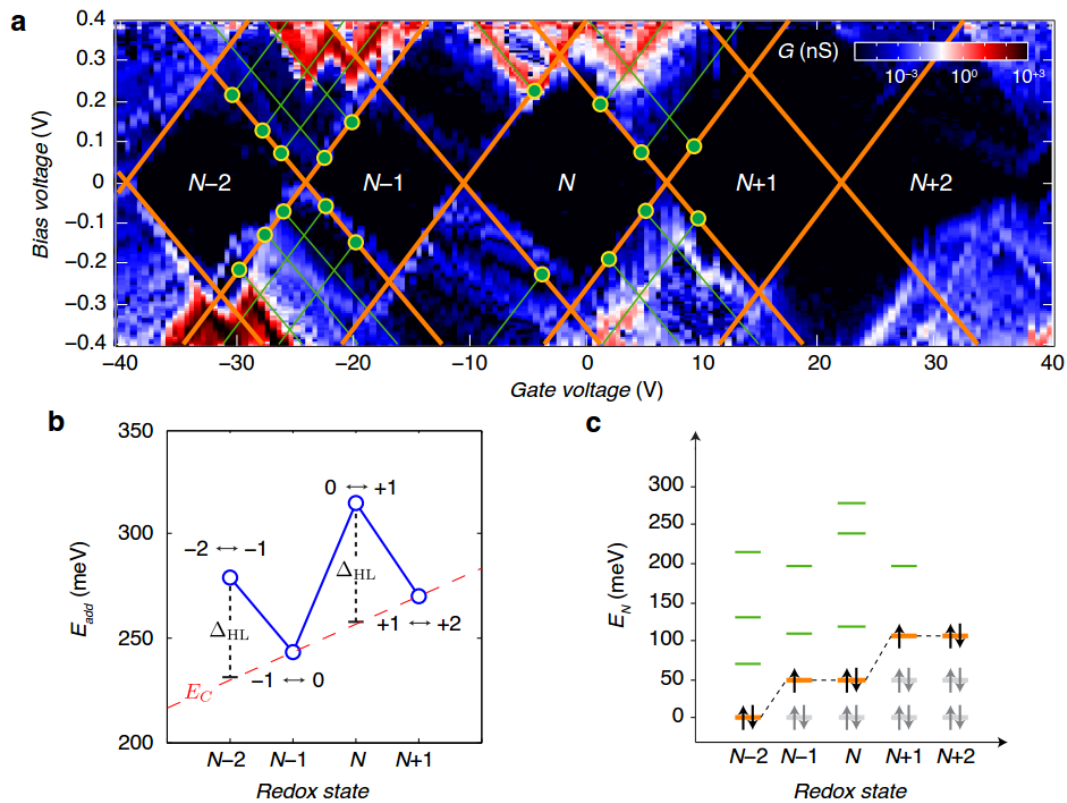


Figure 20 (a) Differential conductance G obtained from the numerical derivative of the current (dl/dV_b) as a function of V_b and V_g . Excited state transitions lead to lines in the stability diagram running parallel to the edges of the Coulomb diamonds in the SET regime. The bias voltage V_b where the excited state line intersects the Coulomb

diamond edges (green dots) is a direct measure of the i^{th} excited state energy with respect to the ground state of the redox state N , $E_{N,i} = e|V_{b,i}|$. We infer the charge degeneracy point of the $N + 1 \leftrightarrow N + 2$ transition from the features in the bottom-right of the $N + 1$ diamond and the top-left of the $N + 2$ diamond. (b) Addition energy E_{add} as a function of the redox state N . We estimate Δ_{HL} from the energy differences between odd/even redox states. (see main text) (c) Single-particle energy spectrum E_N as a function of redox state N . Starting from $N - 2$ redox state, successive ground state energy is determined by adding Δ_{HL} (orange lines). The excited state energies $E_{N,i}$ as determined from (a) are then added to the ground state energy for each redox state N (green lines). The black arrows indicate the electron spins in the orbital filling.

The level spacing of the molecular orbitals and electron-electron interactions can be investigated by looking more closely at the transport spectroscopy of device 8. Fig. 20a shows the differential conductance G obtained from the numerical derivative of the current (dI/dV_b) as a function of V_b and V_g . This conductance stability diagram shows multiple Coulomb diamonds each representing a different redox state. In the constant interaction model,¹⁵ E_{add} consists of: (i) the charging energy E_C due to Coulomb interactions of electrons in the molecule and (ii) Δ_{HL} , the energy spacing between the HOMO and LUMO. The contribution of E_C and Δ_{HL} to E_{add} can be estimated by comparing $E_{\text{add}}(N)$ for successive redox states N and considering the spin-degeneracy of the molecular orbitals. Fig. 20b shows $E_{\text{add}}(N)$ as a function of successive redox states $N - 2$ to $N + 1$ which displays odd/even oscillation typical for spin $\frac{1}{2}$ systems with an orbital degeneracy of 2.¹⁶ For a molecular redox state with an even number of electrons, the HOMO is fully occupied and the additional electron has to occupy the LUMO, which is separated from the HOMO by the energy spacing Δ_{HL} . The addition energy is then $E_{\text{add}} = E_C + \Delta_{\text{HL}}$. For a molecular redox state with an odd number of electrons, the additional electron occupies the HOMO and $E_{\text{add}} = E_C$. This leads to the observed odd/even oscillations of low/high $E_{\text{add}}(N)$ for successive redox states.

There are two high-energy transitions where the additional electron occupies the LUMO where $E_{\text{add}} = E_C + \Delta_{\text{HL}}$; and two low-energy transitions where the additional electron occupies the HOMO where $E_{\text{add}} = E_C$. We estimate the charging energy $E_C(N) = E_{C0} + \beta N$ with $E_{C0} = 230$ meV and $\beta = 10$ meV from a linear interpolation of $E_{\text{add}}(N - 1)$ and

$E_{\text{add}}(N + 1)$. We calculate for two redox states $\Delta_{\text{HL}}(N - 2) = 50$ meV and $\Delta_{\text{HL}}(N) = 60$ meV. Several redox states have been previously observed for OPV molecules in gold nano-gaps.¹⁶ We further substantiate this interpretation of the addition energies by considering the high-bias excited state spectroscopy for each redox state (Fig. 20c), enabled by the stability of our graphene nano-electrodes which allows for applied bias voltages beyond the limit of electromigrated gold electrodes.¹⁶ We construct the single-particle energy spectrum $E_{N,i}(N)$ as a function of the redox state N by using the excited state spectra for each redox state and the values for Δ_{HL} . Starting with the $N - 2$ redox state, the successive ground state energy levels are obtained by adding Δ_{HL} (orange lines in Fig. 20c). The excited state energies $E_{N,i}$, obtained from the bias voltage V_b where the i^{th} excited state lines intersect the Coulomb diamond edges (Fig. 20a), are then added to the ground state energy for each redox states (green lines in Fig. 20c). We find that the energy of the first excited state of the $N - 2$ redox state $E_{N-2,1}$ aligns with the ground state energies, $E_{N-1,0}$ and $E_{N,0}$, of the $N - 1$ and N redox states. $E_{N,i}$ is largely independent of N with intervals dominated by Δ_{HL} .

The experimentally determined Δ_{HL} is rather small compared to spectroscopic measurements of self-assembled monolayers of molecules or calculations of gas-phase molecules.¹⁷⁻²⁰ Renormalisation corrections of $\sim 3 - 4$ eV have been experimentally observed and theoretically predicted for single-molecules in nano-gap junctions^{9,16,21-24} and for molecules on graphitic surfaces.²⁵ This renormalisation effect is usually attributed to the formation of image charges in the gate and source/drain electrodes which rearranges the electron density in the molecule leading to a modification of the frontier orbitals alignment. As a result, DFT calculations cannot be relied upon to produce exact values for the positions of the HOMO and LUMO levels relative to the chemical potential of the electrodes, but can be used to predict other properties such as molecular conformations (Fig. 18b), HOMO-LUMO gap trends and orbital symmetries.^{26,27} Indeed, the addition energy for one electron obtained from our DFT calculations for unscreened gas phase molecules is 3.84 eV. We consider a screening potential where the charging contribution is $W = \frac{e^2 \ln 2}{8\pi\epsilon_0 a}$,^{28,29} where $a = 3.2$ Å is the

distance between the surface of the graphene electrodes and the surface of the TBF ‘butterfly’ anchor groups as obtained from the DFT calculated relaxed geometry (Fig. 18b). This correction reduces the additional energy to ~ 740 meV.

Finally, the large addition energies observed in our measurements mean that room temperature operation should in principle be possible, since $E_{\text{add}} > k_{\text{B}}T$, the thermal energy. At $T = 300$ K, $k_{\text{B}}T = 25.6$ meV $< E_{\text{add}} \sim 370$ meV for our devices. Additionally, the stability of graphene at elevated temperature is an important factor to enable room temperature operation. The stability diagram of device 2 measured at room temperature in vacuum is shown in Fig. 21. It is necessary to perform the measurements in vacuum as the devices are sensitive to the adsorption of ambient molecules. We are able to fully resolve two Coulomb diamonds and therefore analyse the charge transitions between three successive redox states. We estimate the charging energy $E_{\text{C}} = 280 \pm 50$ meV and $\Delta_{\text{HL}} = 90 \pm 50$ meV by comparing E_{add} for N and $N + 1$ redox states at room temperature. There are notable differences between measurements taken at cryogenic and room temperatures. Substantially more noise at room temperature is observed due to thermal fluctuations. Random switching events are observed even at low gate voltage as compared to cryogenic measurements where occasional switching events are observed at large gate voltages. One possibility for this observation is molecular conformation changes due to the increased thermal energy. Molecular conformation is known to influence the conductance.^{30–32} Another possibility is the presence of dopants and trapped charges in the thermally grown SiO_2 layer that are more mobile at elevated temperatures. The dopants and trapped charges alters the electrostatic environment around the molecule and therefore its chemical potential. One way to improve stability and performance in our devices is to replace the thick 300 nm SiO_2 layer. Thin aluminium oxide layers of a few nanometres will greatly enhance the gate coupling. This reduces the gate voltage required to access multiple redox states. Hexagonal boron nitride has also been studied as an excellent substrate for graphene devices. Its atomically smooth

surface which is relatively free of dangling bonds and charge traps has led to improved carrier mobilities and reduced inhomogeneities compared to SiO₂.³³

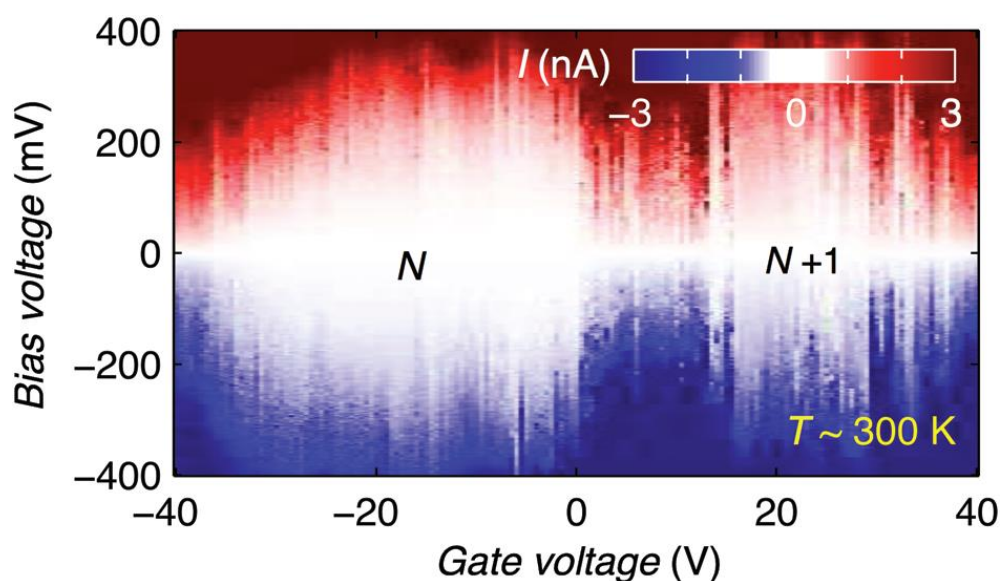


Figure 21 Current stability diagram I as a function of V_b and V_g measured at room temperature. Coulomb diamonds for two redox states, N and $N + 1$ are fully resolved owing to the high stability and reduced electrostatic screening afforded by the graphene nano-electrodes.

3.4 Conclusion

We have demonstrated room temperature operation of a stable and reproducible graphene-porphyrin-graphene single-molecule transistor architecture. The modular design of the porphyrin molecule allows for specific device functionalities based on diverse functional groups. In particular, the stable $\pi - \pi$ anchoring of the TBF ‘butterfly’ anchor groups to the graphene nano-electrodes allow for high-bias spectroscopy of excited states. Our results offer possibilities for quantum transport experiments well established for semiconductor quantum dots but at an energy scale much larger than $k_B T$ at room temperature.

Combining single molecules with novel two dimensional materials and semiconductor fabrication techniques provides a platform for realising scalable room-temperature single-molecule transistor networks. Such a device architecture could consist of single molecules coupled to each other via graphene nano-electrodes, with nearby graphene gate-electrodes to electrostatically tune the chemical potential of each molecule. The gate electrodes can be

separated from the molecules by a two-dimensional insulator such as hexagonal boron nitride to enhance the gate coupling. Side gate electrodes can also allow for strong gate coupling due to the close proximity to the molecule. Recently, our group demonstrated a three-terminal graphene single-electron transistor where the side gate electrode is fabricated using feedback controlled electroburning.³⁴ Here we demonstrate the first step towards such a device architecture. Further improvements in the fabrication of the graphene nano-gaps and oxide layer is required in order to reduce variability in the gate coupling and molecule-electrode coupling and will be crucial for the development of single-molecule electronics.

References

1. Lörtscher, E. Wiring molecules into circuits. *Nat. Nanotechnol.* **8**, 381–4 (2013).
2. Péterfalvi, C. G. & Lambert, C. J. Suppression of single-molecule conductance fluctuations using extended anchor groups on graphene and carbon-nanotube electrodes. *Phys. Rev. B* **86**, 85443 (2012).
3. Prins, F. *et al.* Room-temperature gating of molecular junctions using few-layer graphene nanogap electrodes. *Nano Lett.* **11**, 4607–11 (2011).
4. Perrin, M. L. *et al.* Influence of the chemical structure on the stability and conductance of porphyrin single-molecule junctions. *Angew. Chem. Int. Ed. Engl.* **50**, 11223–6 (2011).
5. Jurow, M., Schuckman, A. E., Batteas, J. D. & Drain, C. M. Porphyrins as molecular electronic components of functional devices. *Coord. Chem. Rev.* **254**, 2297–2310 (2010).
6. Mohnani, S. & Bonifazi, D. Supramolecular architectures of porphyrins on surfaces: The structural evolution from 1D to 2D to 3D to devices. *Coord. Chem. Rev.* **254**, 2342–2362 (2010).
7. Sedghi, G. *et al.* Long-range electron tunnelling in oligo-porphyrin molecular wires. *Nat Nano* **6**, 517–523 (2011).
8. Bailey, S. *et al.* A study of planar anchor groups for graphene-based single-molecule electronics. *J. Chem. Phys.* **140**, 054708 (2014).
9. Perrin, M. L. *et al.* Large tunable image-charge effects in single-molecule junctions. *Nat. Nanotechnol.* **8**, 282–7 (2013).
10. Dutton, J. K., Knox, J. H., Radisson, X., Ritchie, H. J. & Ramage, R. Synthesis of

- 17H-tetrabenz[a,c,g,i]fluorene derivatives as chiral selectors for enantiomeric separation by HPLC on porous graphitised carbon. *J. Chem. Soc. Trans. 1* 2581–2587 (1995).
11. Assali, M. *et al.* Improved non-covalent biofunctionalization of multi-walled carbon nanotubes using carbohydrate amphiphiles with a butterfly-like polyaromatic tail. *Nano Res.* **3**, 764–778 (2010).
 12. Chuang, C. *et al.* Evidence for formation of multi-quantum dots in hydrogenated graphene. *Nanoscale Res. Lett.* **7**, 1–6 (2012).
 13. Barreiro, A., van der Zant, H. S. J. & Vandersypen, L. M. K. Quantum dots at room temperature carved out from few-layer graphene. *Nano Lett.* **12**, 6096–100 (2012).
 14. Osorio, E. a, Bjørnholm, T., Lehn, J.-M., Ruben, M. & van der Zant, H. S. J. Single-molecule transport in three-terminal devices. *J. Phys. Condens. Matter* **20**, 374121 (2008).
 15. Hanson, R. *et al.* Spins in few-electron quantum dots. *Rev. Mod. Phys.* **79**, 1217–1265 (2007).
 16. Kubatkin, S. *et al.* Single-electron transistor of a single organic molecule with access to several redox states. *Nature* **425**, 698–701 (2003).
 17. Otsuki, J. STM studies on porphyrins. *Coord. Chem. Rev.* **254**, 2311–2341 (2010).
 18. Lange, I. *et al.* Band bending in conjugated polymer layers. *Phys. Rev. Lett.* **106**, (2011).
 19. Koch, N. Energy levels at interfaces between metals and conjugated organic molecules. *J. Phys. Condens. Matter* **20**, 184008 (2008).
 20. Hwang, J., Wan, A. & Kahn, A. Energetics of metal-organic interfaces: New experiments and assessment of the field. *Materials Science and Engineering R:*

- Reports* **64**, 1–31 (2009).
21. Moth-Poulsen, K. & Bjørnholm, T. Molecular electronics with single molecules in solid-state devices. *Nat. Nanotechnol.* **4**, 551–6 (2009).
 22. Verzijl, C. J. O. *et al.* Image effects in transport at metal-molecule interfaces. *J. Chem. Phys.* **143**, (2015).
 23. Kaasbjerg, K. & Flensberg, K. Strong polarization-induced reduction of addition energies in single-molecule nanojunctions. *Nano Lett.* **8**, 3809–14 (2008).
 24. Osorio, E. a. *et al.* Addition energies and vibrational fine structure measured in electromigrated single-molecule junctions based on an oligophenylenevinylene derivative. *Adv. Mater.* **19**, 281–285 (2007).
 25. Neaton, J. B., Hybertsen, M. S. & Louie, S. G. Renormalization of molecular electronic levels at metal-molecule interfaces. *Phys. Rev. Lett.* **97**, (2006).
 26. Lambert, C. J. Basic concepts of quantum interference and electron transport in single-molecule electronics. *Chem. Soc. Rev.* **44**, 875–888 (2015).
 27. Liu, Z.-F. *et al.* Control of single-molecule junction conductance of porphyrins via a transition-metal center. *Nano Lett.* **14**, 5365–70 (2014).
 28. Quek, S. Y. *et al.* Mechanically controlled binary conductance switching of a single-molecule junction. *Nat. Nanotechnol.* **4**, 230–4 (2009).
 29. García-Suárez, V. M. & Lambert, C. J. First-principles scheme for spectral adjustment in nanoscale transport. *New J. Phys.* **13**, (2011).
 30. Venkataraman, L., Klare, J. E., Nuckolls, C., Hybertsen, M. S. & Steigerwald, M. L. Dependence of single-molecule junction conductance on molecular conformation. *Nature* **442**, 904–7 (2006).
 31. Donhauser, Z. J. *et al.* Conductance switching in single molecules through

- conformational changes. *Science* **292**, 2303–2307 (2001).
32. Moresco, F. *et al.* Conformational changes of single molecules induced by scanning tunneling microscopy manipulation: a route to molecular switching. *Phys. Rev. Lett.* **86**, 672–675 (2001).
 33. Dean, C. R. *et al.* Boron nitride substrates for high-quality graphene electronics. *Nat. Nanotechnol.* **5**, 722–6 (2010).
 34. Puczkarski, P. *et al.* Three-terminal graphene single-electron transistor fabricated using feedback-controlled electroburning. *Appl. Phys. Lett.* **107**, (2015).

Chapter 4: Electron-Vibron Coupling in a Graphene-Fullerene Single-Molecule Transistor

4.1 Introduction

In the previous chapter, we demonstrated a reliable approach which provides a versatile platform for the study of quantum transport in single-molecule devices. We next employ this approach to fabricate a system suitable for the study of vibrational effects in single-molecule junctions. Coupling between molecular vibrational modes and tunnelling electrons can result in novel transport phenomenon not commonly observed in metal/semiconductor quantum dots.¹⁻⁹ These vibrational modes, or vibrons, can be excited via charge transport; and strong electron-vibron coupling can result in suppressed low-bias tunnel current.^{10,11} Super-Poissonian current noise due to avalanche-type charge transport, characterized by giant Fano factors, have also been predicted for molecular junctions with weak vibron-relaxation and strong electron-vibron coupling, but has hitherto not been experimentally observed. We present a single-molecule transistor where a functionalised C₆₀ binds to graphene nano-electrodes via $\pi - \pi$ stacking interactions. The stability, strong electron-vibron coupling and weak vibron-relaxation of this system enables the investigation of redox-dependent electron-vibron coupling and avalanche transport.

4.2 Experimental Setup

We employ the same device architecture as described in the previous chapters. The architecture consists of graphene nano-electrodes fabricated via feedback controlled electroburning on a heavily doped silicon substrate with a 300 nm thick oxide layer which acts as the back gate electrode. The molecule used in this device is a pyrene functionalised C₆₀ bisadduct synthesized through a 1,3 dipolar cycloaddition using 1-pyrene carboxaldehyde and *N*-methylglycine^{6,12} and is deposited via a chloroform solution. The functionalisation produces 8 different isomers. However, steric considerations mean only the *cis*-2 (Fig. 22a) and *cis*-3 (Fig. 22b) isomers are expected to bridge the graphene nano-gap. DFT calculations of the

relaxed geometry confirm that the *cis*-3 isomer where the pyrene anchors make a planar structure with both the graphene nano-electrodes forms the most stable configuration with the least steric hindrance (Fig. 24a). In contrast, the pyrene anchors of the *cis*-2 isomer make a planar structure with one graphene nano-electrode but not the other due to the larger angle between the two anchors. Fig. 23 shows the iso-surfaces of the frontier orbitals of gas phase *cis*-3 and *cis*-2 isomers. The wavefunction of the LUMO level is mostly localised in the central C₆₀, whereas the wavefunction for the HOMO is extended to the pyrene anchors. The wavefunction delocalisation of the HOMO level is more pronounced for the *cis*-3 isomer compared to the *cis*-2 isomer, indicating better $\pi - \pi$ stacking interaction with the graphene nano-electrodes and a higher likelihood of bridging the nano-gap. We note that for pristine C₆₀, DFT predicts LUMO dominated transport as confirmed by thermoelectric experiments,¹³ in contrast to our DFT calculations which predict HOMO dominated transport for the bisadduct.

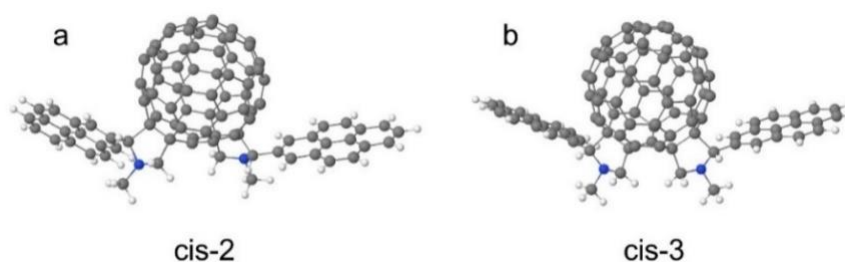


Figure 22 Chemical structure of the C₆₀ bisadduct for two isomers, *cis*-2 (a) and *cis*-3 (b), consisting of two pyrene anchor groups functionalised to a central C₆₀.

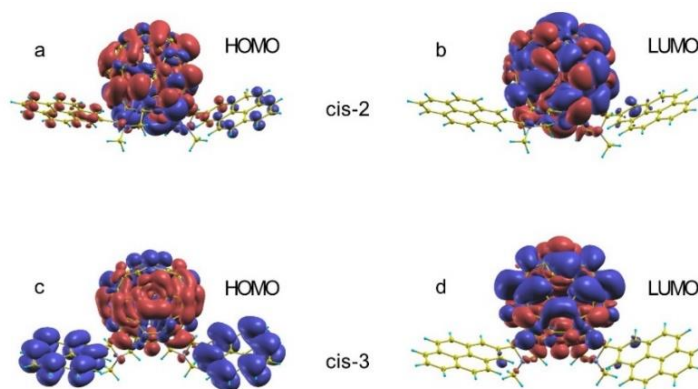


Figure 23 DFT simulations of the iso-surfaces of the frontier orbitals of the *cis*-2 (a, b) and *cis*-3 (c, d) isomers.

4.3 Orbital Degeneracy

We perform transport spectroscopy on our graphene-fullerene single-molecule transistor. Fig. 24b shows the current I stability diagram as a function of the bias voltage V_b and gate voltage V_g of device A measured at 20 mK. Three Coulomb diamonds representing 5 redox states are fully resolved. We observe that the addition energies, as measured from the height of the Coulomb diamonds, are $E_{\text{add}} \sim 160$ meV for all the redox state transitions. Notably, the odd/even oscillations of E_{add} observed for two-fold spin-degenerate orbital systems, such as the graphene-porphyrin single-molecule transistor described in Chapter 3, are absent.^{14,15} We attribute the absence to degenerate orbitals of the C_{60} molecule.¹⁶ Because of high spatial symmetry, pristine C_{60} exhibits fivefold degeneracy for the HOMO and threefold degeneracy for the LUMO. Consequently, high spin configurations are preferred due to the large degeneracy in each orbital level and $E_{\text{add}} = E_C$ for at least three charge transitions. The interactions within each shell in pristine C_{60} are almost constant except for a slight increase of the electron-electron on-site Coulomb interaction at the middle of each shell, where electrons with opposite spins begins to fill. We observe a small increase of ~ 10 meV per electron added from redox state N to $N + 2$, which is possibly due to electron-electron on-site Coulomb interactions. While the high spatial symmetry of pristine C_{60} is no longer completely preserved in the case of our bisadduct, our DFT calculations of the Kohn-Sham energy levels indicate that the HOMO and HOMO-1 levels are nearly degenerate, whereas the LUMO and LUMO +1 levels are well separated in energy (Table 4). As E_{add} is almost constant for three redox-state transitions, we infer that the electrons are exclusively filling an orbital that is at least four-fold degenerate. We therefore conclude that charge transport through the molecule is HOMO dominated, based on two independent observations. First, DFT calculations predict that the chemical potentials of the electrodes are more closely aligned to the HOMO than the LUMO. Second, the experimental observation of a four-fold orbital degeneracy is consistent with the nearly degenerate HOMO and HOMO-1 levels predicted by DFT. Note that as mentioned in the previous chapter, while DFT calculations cannot be relied upon to produce exact values

for the positions of the HOMO and LUMO levels relative to the chemical potential of the electrodes, it can be used to predict HOMO-LUMO gap trends.^{17,18}

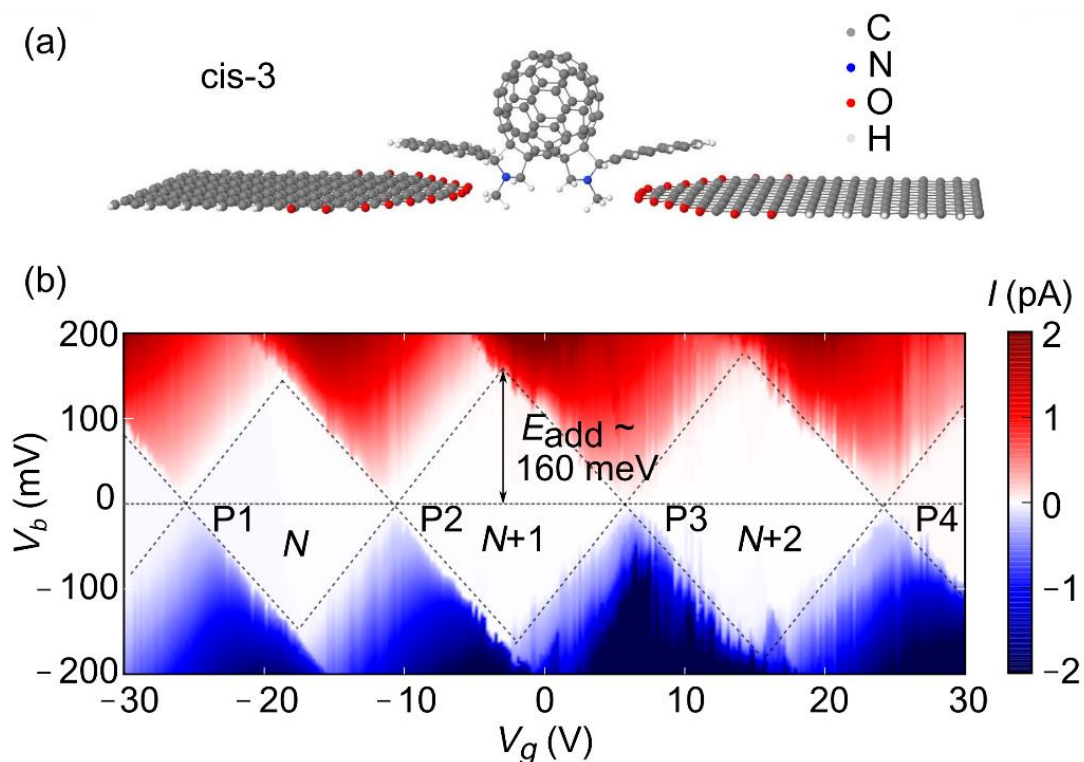


Figure 24 (a) DFT calculations of the relaxed geometry of the *cis-3* isomer bridging the graphene nano-gap. (b) Current stability diagram of device A measured at 20 mK. Three full Coulomb diamonds of similar addition energy $E_{\text{add}} \sim 160$ meV can be observed, indicating that the electrons are filling a shell that is at least four-fold degenerate.

Level	<i>cis-2</i> (eV)	<i>cis-3</i> (eV)
HOMO-2	-4.71	-4.69
HOMO-1	-4.64	-4.60
HOMO	-4.41	-4.59
LUMO	-3.07	-3.12
LUMO+1	-3.05	-2.86
LUMO+2	-2,76	-2.86
HOMO-LUMO gap	1.34	1.47

Table 4 DFT calculated Kohn-Sham energies around the Fermi energy.

4.4 Vibrational Excited States

Vibrational modes can show up as excited states lines running parallel to the Coulomb diamond edges in the stability diagram if the energy lies within the bias window defined by V_b . Fig. 25 shows the differential conductance G stability diagram as a function of V_b and V_g for the redox state transition $N + 1$ to $N + 2$ for device A taken with a higher resolution. The gate potential for this redox state transition is different for repeated measurements due to a commonly observed hysteretic effect. The hysteresis occurs when V_g is swept quickly across a large voltage range but is otherwise absent when V_g is swept slowly. We observe excited state transition lines at energies ≥ 33 meV (white arrows) which are in excellent agreement with the intrinsic vibrational modes of pristine C_{60} (Table 5).¹⁹ Excited state transitions are also observed at energies < 33 meV (green arrows) which are below the lowest intrinsic vibrational mode of pristine C_{60} . The bias polarity asymmetry of the excited states can be explained through a rate equation model involving asymmetric tunnelling barriers. A similar phenomenon has been observed for the excited state spectrum of a single donor in silicon.²⁰ When the excited state relaxations are faster than the tunnelling rates, electrons can tunnel on to the molecule through any excited states within the bias window but only leave the molecule via the ground state as the molecule relaxes. In the SET regime, the current I through the molecule is:

$$I = \frac{e(\Gamma_{in}^0 + \Gamma_{in}^1 \dots + \Gamma_{in}^n)\Gamma_{out}^1}{\Gamma_{in}^0 + \Gamma_{in}^1 + \dots + \Gamma_{in}^n + \Gamma_{out}^1}, \quad (11)$$

where Γ is the molecule-electrode coupling determining the tunnelling rate. The subscript denotes tunnelling rate in or out of the molecule, while the superscript labels the energy levels (0 is the ground state) up to the n th excited state within the bias window. For asymmetrical tunnel barriers, $\Gamma_{in} \gg \Gamma_{out}$ for $V_b > 0$ and $\Gamma_{in} \ll \Gamma_{out}$ for $V_b < 0$. In this limit, the above equation reduces to:

$$I = \begin{cases} e(\Gamma_{in}^0 + \Gamma_{in}^1 \dots + \Gamma_{in}^n) & V_b < 0 \\ e\Gamma_{out}^0 & V_b > 0. \end{cases} \quad (12)$$

Therefore, for $V_b < 0$, excited state transitions within the bias window will lead to current steps that show up as lines in the G stability diagram within the SET regime. However, for $V_b > 0$, the current saturates and no excited state lines will be observed.

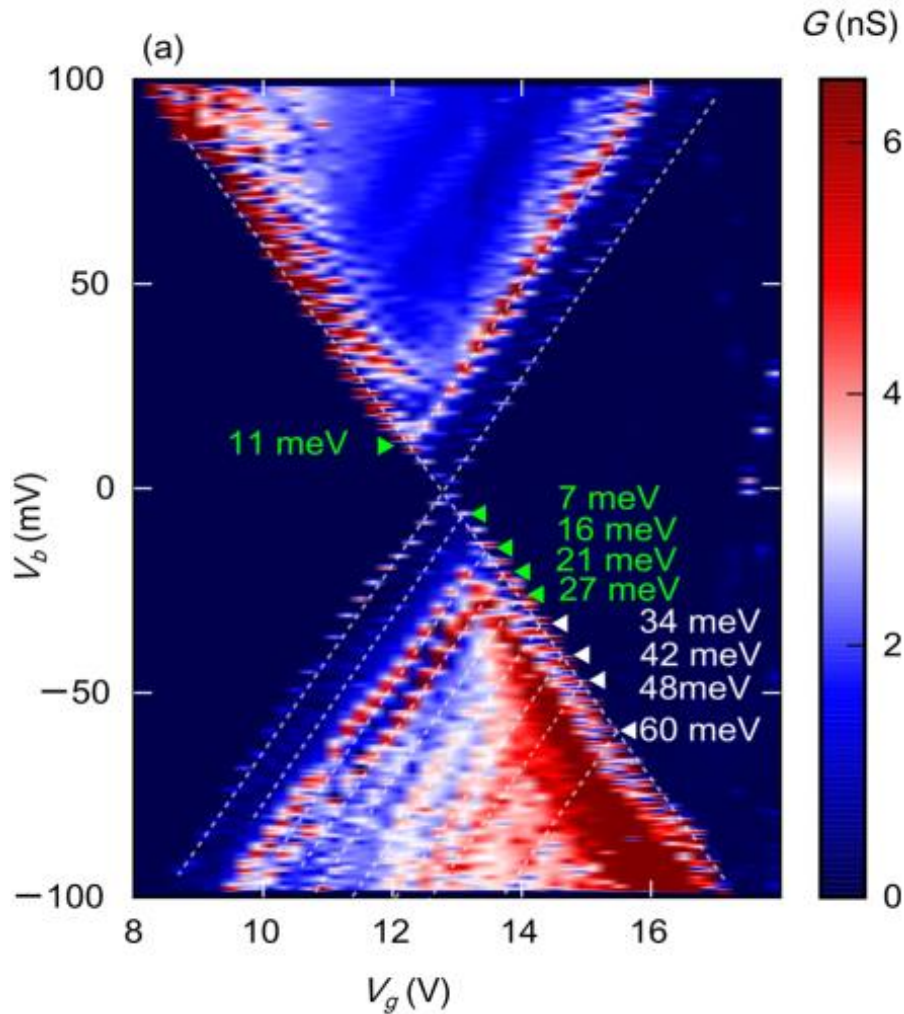


Figure 25 Conductance G stability diagram of the $N + 1$ to $N + 2$ transition (P3) obtained by taking the numerical derivative of the current measured. Excited states are indicated by the white and green arrows with the energies labelled.

To extract the energies of these excited state transitions from the transport measurements, we first determine the slopes of the Coulomb diamond edges. Fig. 26 shows the fitting procedure used to determine the excited state energies. The white circles along the Coulomb diamond edge indicate the maximum conductance over a small bias window for a fixed V_g . A typical bias window is depicted by the vertical white line. The slopes are determined

by straight line fits (red lines) to the points indicated by the white circles. We then use the slopes to determine the area indicated by the rectangular yellow boxes over which we average the conductance. The average conductance as a function of energy is shown for positive bias (Fig. 26b) and for negative bias (Fig. 26c), where the energy axis is offset by shifting the first conductance peak representing the ground state transition (Coulomb diamond edge) to zero energy. The energies of the excited state transitions are then determined from the peak positions as labelled in Fig. 26(b, c).

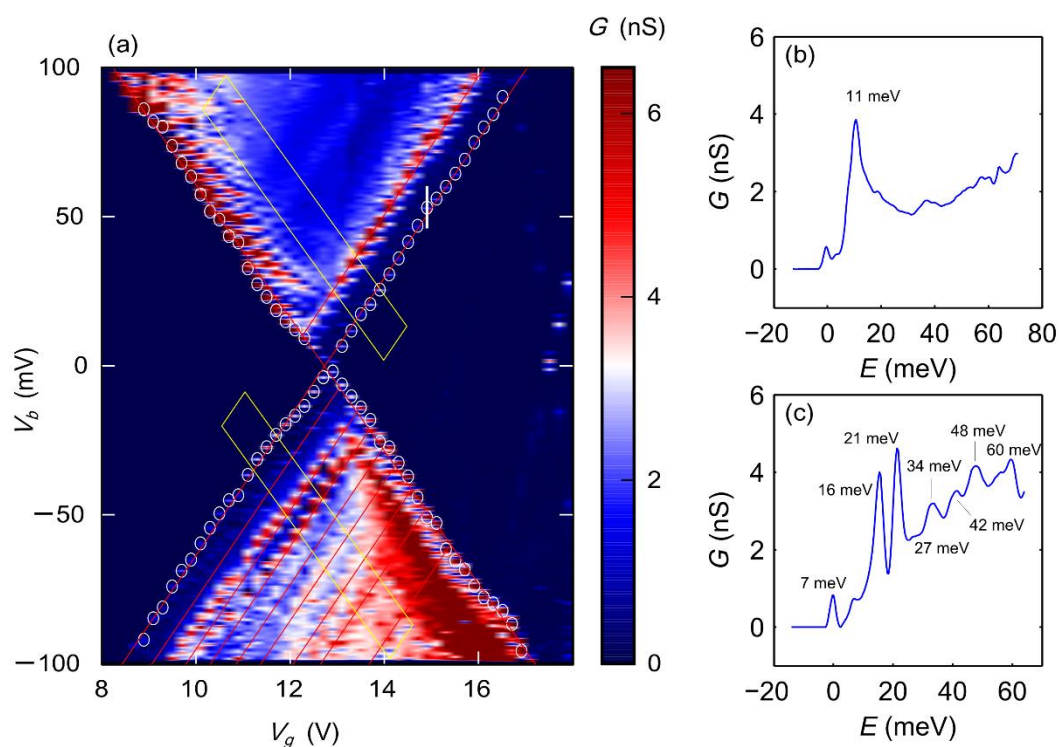


Figure 26 Procedure for determining the excited state transition energies in Fig. 25. (a) Conductance stability diagram of redox state transition P3 of device A as shown in Fig. 24. The white circles indicate the maximum conductance over a small bias window. A typical window is indicated by the vertical white line. Red lines through the white circles indicate the straight line fits for determining the slopes of the Coulomb diamond edges. This allows us to determine the area over which the conductance is averaged as indicated by the yellow box. The averaged conductance as a function of energy for positive bias (b) and negative bias (c).

To confirm the vibrational nature of the excited state transition lines observed in Fig. 25, we perform Raman spectroscopy on the bisadducts and pristine C_{60} . Fig. 27a shows the

Raman spectrum of the pristine C₆₀ (red) and the bisadducts (blue) on gold coated glass substrate recorded with 532 nm laser excitation. The gold coating enhances the Raman scattering and improves the signal. The Raman active vibrational modes are indicated above each peak. Fig. 27b shows the magnified A_g(2) Raman mode that is blue shifted for the bisadducts compared to the pristine C₆₀, similar to Raman spectra of other exohedrally functionalised or polymerized fullerenes.^{21,22} Fig. 27c shows the low energy Raman spectra of the bisadducts (blue) and the pristine C₆₀ taken on gold coated silicon substrate. The 37 meV peak is due to the silicon background. The details of the Raman spectra and transport spectroscopy are summarized in Table 5 together with values of the intrinsic vibrational modes reported in literature. A comparison of the transport spectroscopy and Raman spectra strongly suggests that the excited state transitions with energy < 33 meV (green) have a vibrational nature.

In order to identify the mechanical motion of these additional low-lying vibrational modes, we compare them to DFT simulations where we analyse the mechanical degrees of freedom of the bisadduct in the limit where the atomic mass of the pyrene anchors approaches infinity. This simulates the scenario where the anchor groups are clamped to the graphene nano-electrodes such that vibrational modes due to internal vibrations of the pyrene anchors are filtered from the vibrational spectrum. The results of the DFT calculations are summarized in Table 5. We find six vibrational modes at energies < 33 meV that matches well with the excited state energies observed in Fig. 25 (green arrows). The six vibrational modes are separated into two sets of three modes, with each set corresponding to the translational and rotational center-of-mass (CM) motion of the central C₆₀ with respect to the pyrene anchors. The animations of the vibrational motion can be found online.⁶

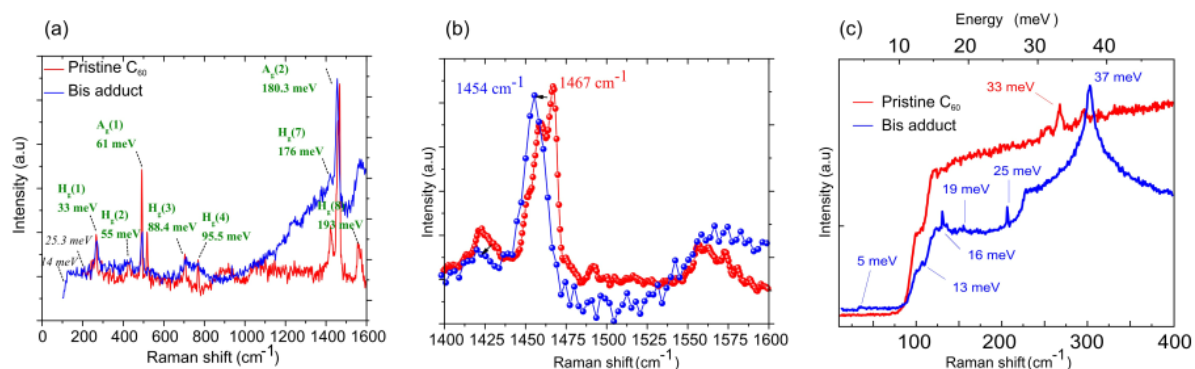


Figure 27 (a) Raman spectra of pristine C₆₀ and bisadduct on gold coated glass substrate. The intrinsic vibrational groups are labelled for each peak. (b) Magnified A_g(2) peak, which is blue shifted for the bisadduct compared to the pristine C₆₀. (c) Raman spectra showing the low energy vibrational modes for pristine C₆₀ (red) and bisadduct (blue) on gold coated silicon substrate. The 37 meV peak is due to the silicon background.

Vibrational mode	Energy (meV)			
	Transport	Raman	DFT	Literature (pristine C ₆₀) ¹⁹
CM T _y	7		8	
CM T _x			10	
CM R _z	11	13	12	
CM T _z	16	16	16	
CM R _x	21	19	19	
CM R _y	27	25	21	
H _g (1)	34	33	32,33,34	33
T _{2u} (1)	42			43
G _u (1)	42			43
H _g (2)	48	55		53
A _g (1)	60	61		61

Table 5 Comparison between vibrational mode energies from measurements by transport and Raman spectroscopy, DFT calculations and literature values of pristine C₆₀. Transport measurements of single-molecule junctions are performed at 20 mK. Raman spectroscopy is performed at room temperature with the molecules drop casted on gold coated glass/silicon substrates to enhance the Raman scattering. DFT calculations are performed in the limit where the degrees of motion of the anchor groups are completely restricted. The literature values of the vibrational modes for pristine C₆₀ are obtained from ref [19], which reports a range of values obtained from experiments and ab initio calculations performed by different groups. The values reported can differ by up to 10 meV.

4.5 Franck-Condon Blockade

Having established the vibrational nature of the excited state transition lines observed in Fig. 25, we next look in greater detail at the four redox state transitions representing the redox states from $N - 1$ to $N + 3$ (labelled P1-4 in Fig. 24). Fig. 28 shows the high resolution differential conductance G stability diagrams for these four redox state transitions. We observe evenly spaced low energy excitations (white arrows) for all four redox state transitions with spacings of 1.7 meV (P1), 1.5 meV (P2), 1.7 meV (P3) and 1.5 meV (P4). These low energy excitations are similarly observed in the conductance G stability diagram of a separate device, device B, as shown in Fig. 30a (~ 2 meV). We also observe lines with different slopes, i.e. with different capacitive coupling, within the SET regime which are probably not related to the energy spectrum of the bisadduct. They can be from a different Coulomb diamond from a separate quantum dot located close to the device such as charge traps, other molecules or graphene islands. The lines can also be associated with density of states fluctuations in the graphene electrodes. Similar fluctuations have been previously observed for silicon SETs.²³ To interpret the nature of these low energy excitations (~ 2 meV), we use DFT to analyse vibrational modes of the bisadduct in the scenario where all the mechanical degrees of freedom of the atoms are allowed. The DFT simulations show that the lowest nonzero vibrational mode has an energy of 1.7 meV, consistent with our transport measurements. This mode is associated with the combined center-of-mass motions of the pyrene anchors (in-plane) moving perpendicular relative to the central C_{60} (out-plane). The findings are consistent with previous work showing that the binding energy for adsorption (out-plane) of pyrene on graphene is much higher compared to the energy barriers to rotation or displacement on the graphene surface (in-plane). The pyrene anchors can therefore exhibit small in-plane sliding motion even when bound to the graphene electrodes via $\pi - \pi$ stacking interactions.²⁴

The Coulomb diamond edges do not intersect at $V_b = 0$ V for redox state transitions P1-3 (Fig. 28 (a-c)) where the current is suppressed at low bias. We observe the same current suppression at low bias in device C (Fig. 30b). The current suppression has no dependence

on magnetic field as shown in Fig. 29, which compares the stability diagrams with and without an applied magnetic field $B = 6$ T, thus ruling out a magnetic origin. The size of the bias gap where the current is suppressed, i.e. the lowest bias voltage V_b when current flows through the molecule, corresponds to an integer spacing of the energy excitations (white horizontal dotted guide lines in Fig. 28). We attribute these characteristics to Franck-Condon (FC) blockade which occurs for strong electron-vibron coupling and results in suppressed current at low bias due to insufficient overlap between low lying vibronic states.^{4,9-11}

Fig. 34a illustrates the FC blockade effect where the vibronic wavefunctions for redox states N and $N + 1$ are described by harmonic oscillator potentials. When an electron tunnels on to the molecule, the equilibrium coordinates of the vibronic wavefunctions for redox states N and $N + 1$ are shifted relative to each other by an amount proportional to the dimensionless electron-vibron coupling constant λ . The displacement of the $N + 1$ redox state from the redox state N is large for strong electron-vibron coupling, i.e. $\lambda \gg 1$. Consequently, the transition rate between the vibronic ground states of redox states N and $N + 1$ which is determined by the overlap of the vibronic wavefunctions, is exponentially reduced with λ . However, there is still significant overlap between the vibronic ground state of the N redox state and the highly excited vibronic states of the $N + 1$ redox state. The excited vibronic wavefunctions for these redox states are widely spread in space as a result of the harmonic oscillator potential and so the transition rates involving these excited states are much higher. The observed FC bias gap occurs when the transition rates involving low lying vibronic states are small leading to suppressed current. The FC blockade is only lifted when the applied bias is sufficient for a transition from the vibronic ground state of redox state N to a vibronic excited state of redox state $N + 1$ for which the transition rate is significant due to greater vibronic wavefunction overlap (Fig. 34c). The FC gap therefore matches a multiple of the vibrational quantum $n\hbar\omega$ and is proportional to $\lambda^2\hbar\omega$.⁴

With increasing number of electrons on the molecule, we observe that the FC gap decreases from redox transitions P2 to P4. For P4 (Fig. 28d), the FC blockade is completely

lifted and the Coulomb diamond edges intersect at $V_b = 0$ V. We infer that the addition of electrons on the molecule shifts the equilibrium coordinates of the harmonic oscillator potential, leading to a smaller displacement of the equilibrium coordinates of the vibronic wavefunctions between redox states $N + 2$ and $N + 3$, i.e. a smaller λ . Increased overlap of the vibronic ground state wavefunctions result in a higher transition rate allowing for current in the previously FC blockaded region. The observed redox-dependent electron-vibron coupling is possibly due to Jahn-Teller (JT) distortion²⁵ of the molecule, which is known to be particularly strong in molecules with large orbital degeneracy and high spatial symmetry such as C_{60} .²⁶ This is consistent with our observation of four-fold HOMO degeneracy and redox-state dependent λ .

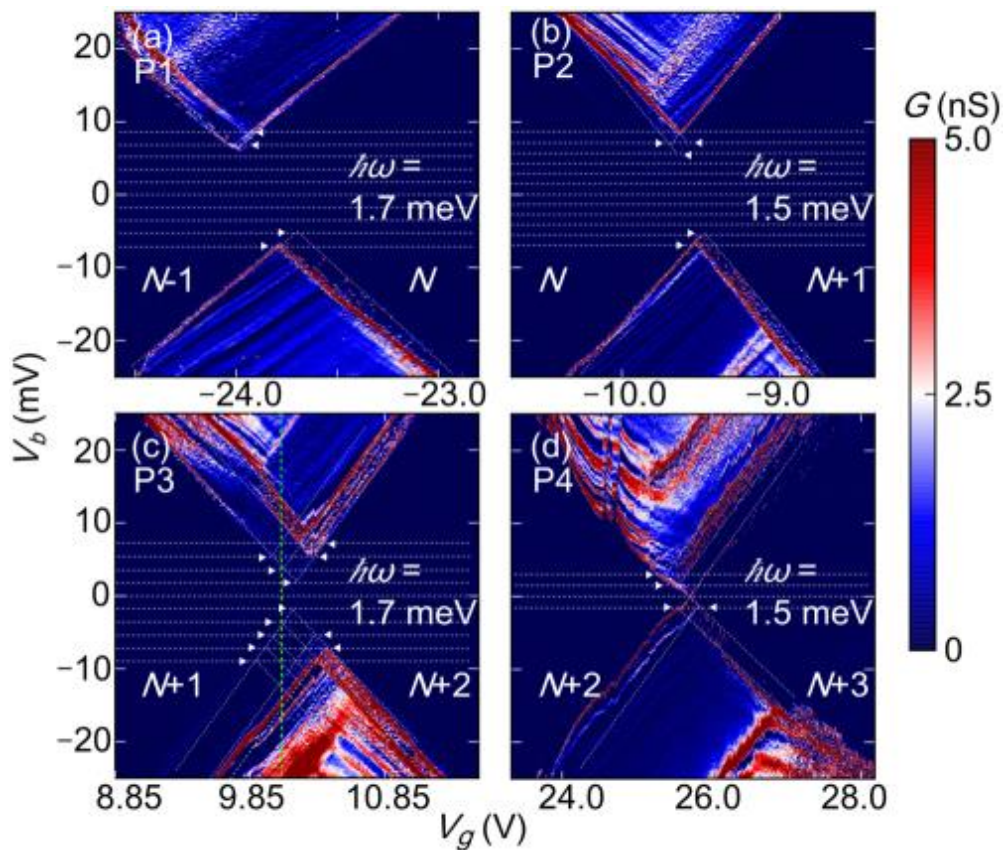


Figure 28 (a-d) Conductance G stability diagrams for redox state transitions $N - 1$ to $N + 3$. The low-bias current suppression is a result of FC blockade in systems with strong electron-vibron coupling. Sets of integer spaced vibrational excited state transition lines (white arrows) are present at low bias. The vertical green line in (c) denotes the gate voltage V_g at which the large current noise due to avalanche transport is measured (Fig. 34). The vibrational quantum energy $\hbar\omega$ is labelled for all four redox state transitions.

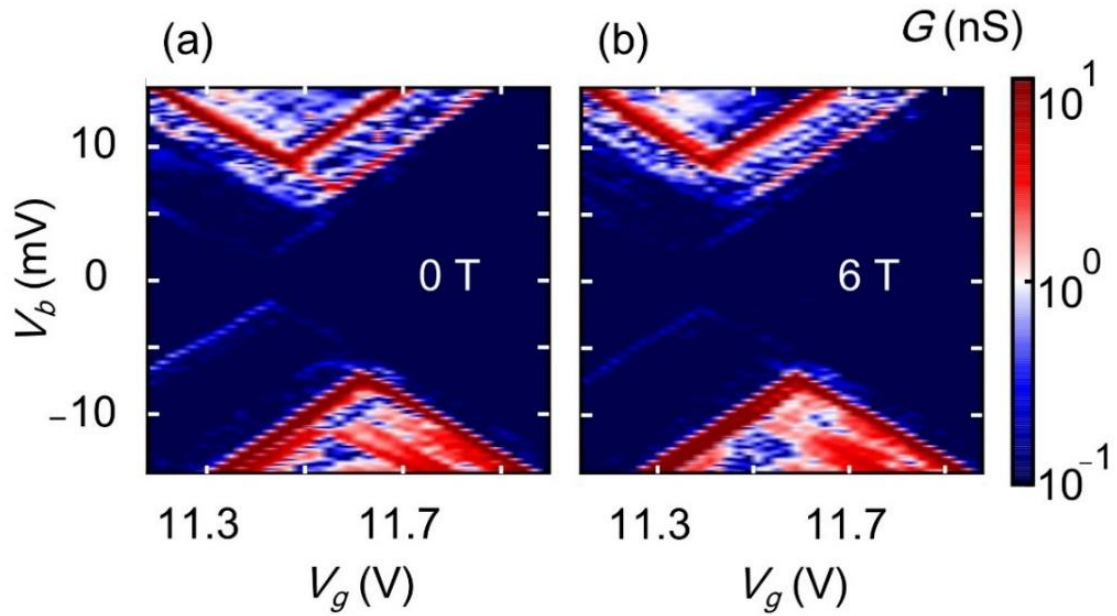


Figure 29 Magnetic field dependence. Conductance stability diagrams of P3 taken at 0 T (a) and 6 T (b). The low bias current suppression has no magnetic dependence.

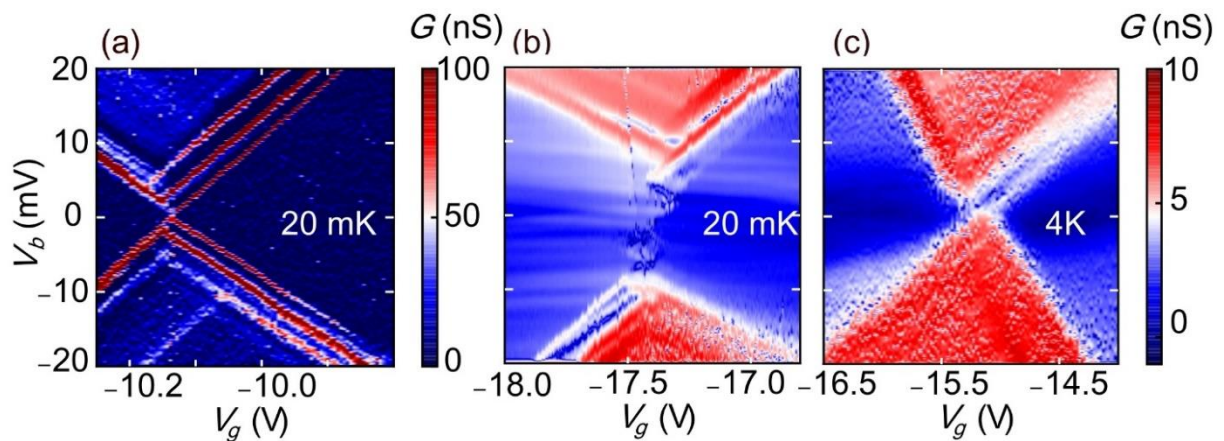


Figure 30 Conductance stability diagrams of device B measured at 20 mK (a), device C at 20 mK (b) and device C at 4 K. In device B, we observe excitation lines similar to those present in device A, but with no FC gap, suggesting a smaller λ . The FC gap is visible in device C. Inelastic co-tunnelling lines can also be seen running horizontal with the gate axis. At 4 K, the FC blockade is lifted and the Coulomb diamond intersects at $V_b = 0$ V.

4.6 Rate Equation Model

To determine λ , the set of evenly spaced excitations of P3 (Fig. 28c) is fitted to a rate equation model. Here, we review the pertinent points of the rate equation model which has

been extensively discussed in refs [4,9,27]. The rate equations determine the occupation probabilities P_q^N for the molecule with redox state N and vibron state q :

$$\frac{dP_q^N}{dt} = \sum_{N',q'} [P_{q'}^{N'} W_{q' \rightarrow q}^{N' \rightarrow N} - P_q^N W_{q \rightarrow q'}^{N \rightarrow N'}] - \frac{1}{\tau} [P_q^{eq} \sum_{q'} P_{q'}^N]. \quad (13)$$

P_q^{eq} denotes the vibron equilibrium distribution with a relaxation time τ and $W_{q \rightarrow q'}^{N \rightarrow N'}$ denotes the total transition rate from the molecular state $|N, q\rangle$ to $|N', q'\rangle$, given by:

$$W_{q \rightarrow q'}^{N \rightarrow (N+1)} = \sum_{a=L,R} [f_a (E_{q'}^{N+1} - E_q^N)] \zeta_{q \rightarrow q'; a}^{N \rightarrow (N+1)}, \quad (14)$$

$$W_{q \rightarrow q'}^{N \rightarrow (N-1)} = \sum_{a=L,R} [1 - f_a (E_q^N - E_{q'}^{N-1})] \zeta_{q \rightarrow q'; a}^{N \rightarrow (N-1)}, \quad (15)$$

where f_a is the Fermi-Dirac distribution for the electrode a (left/right) and the bare transition rates ζ are calculated from Fermi's golden rule. ζ is given by:

$$\zeta_{q \rightarrow q'; a}^{N \rightarrow (N+1)} = s^{N \rightarrow N+1} \frac{2\pi}{\hbar} \rho_a (E_{q'}^{N+1} - E_q^N) |M_{q \rightarrow q'; a}^{N \rightarrow N+1}|^2, \quad (16)$$

$$\zeta_{q \rightarrow q'; a}^{N \rightarrow (N-1)} = s^{N \rightarrow N-1} \frac{2\pi}{\hbar} \rho_a (E_q^N - E_{q'}^{N-1}) |M_{q \rightarrow q'; a}^{N \rightarrow N-1}|^2. \quad (17)$$

Here, ρ_a denotes the density of states in electrode a which we assume in our calculations to be constant for both electrodes. $M_{q \rightarrow q'; a}^{N \rightarrow N \pm 1}$ denotes the FC matrix elements and $s^{N \rightarrow N'}$ the spin factor. For sequential-tunnelling and two-fold degeneracy they are:

$$s^{1 \rightarrow 0} = s^{1 \rightarrow 2} = 1, s^{0 \rightarrow 1} = s^{2 \rightarrow 1} = 2. \quad (18)$$

The FC matrix elements $M_{q \rightarrow q'; a}^{N \rightarrow N \pm 1}$ defined for vibrations are:

$$M_{q \rightarrow q'; a}^{N \rightarrow N \pm 1} = \Gamma \left(\frac{q_1!}{q_2!} \right)^{\frac{1}{2}} \times \lambda^{q_2 - q_1} e^{-\frac{\lambda^2}{2}}, \quad (19)$$

where Γ is the molecule-electrode tunnel coupling $q_1 = \min\{q, q'\}$ and $q_2 = \max\{q, q'\}$.

To determine the energy of the evenly spaced excitations, we use the $I - V$ trace (Fig. 31a) of P3 at $V_g = 10.85$ V (Fig. 28c), which shows a series of steps due to vibron transitions.

The current steps I^n are fitted to a thermally broadened Lorentzian by taking the convolution of the Lorentzian and Fermi-Dirac lineshape:^{28,29}

$$I^n = I_{\text{step}}^n \int \frac{1}{\left(e^{\frac{\beta V_g - E_{\text{res}} - E}{k_B T}} + 1 \right)} \frac{h\Gamma_0/2}{(h\Gamma_0/2)^2 + E^2} dE, \quad (20)$$

where I_{step}^n is the step height, h the planck constant, V_g the gate voltage, β the gate coupling, E_{res} the resonance energy, Γ_0 the molecule-electrode tunnel coupling and E is the energy over which the integral is taken. A typical fit of the current step to the thermally broadened Lorentzian is shown in Fig. 31b, with fit parameters $\Gamma_0 = 1.36$ meV and the step position $V_0 = 23.4$ mV. The fitted step positions V_0 are shown as a function of the current steps n in Fig. 31c. The straight line fit yields a vibrational quantum of 1.7 meV after scaling the bias voltage axis to account for the intersection with the positive slope of the Coulomb diamond. We then determine λ by fitting the five current step heights I_{step}^n obtained from the data to a set of current heights generated using the rate equation model with λ as the fitting parameter (Fig. 31d.) This fit yields $\lambda = 3$ for the redox state transition $N + 1$ to $N + 2$ which is consistent with our experimental observations of strong electron-vibron coupling.

We simulate the current stability diagram using the rate equation model with $\lambda = 3$ and compare it to our measurements for the redox state transition $N + 1$ to $N + 2$ (Fig. 32a). For an asymmetric molecule-electrode tunnel coupling $\Gamma_L = 0.2\Gamma_R$, the simulation shows good qualitative agreement with our data. Asymmetric tunnel coupling can be expected as the electroburnt graphene nano-electrodes are not likely to be symmetric on the atomic scale which can lead to asymmetric positioning of the molecule across the nano-gap. In addition, the relaxed geometry of the molecule as calculated by DFT shows that the pyrene anchors are not symmetric relative to the central C_{60} (Fig. 24a).

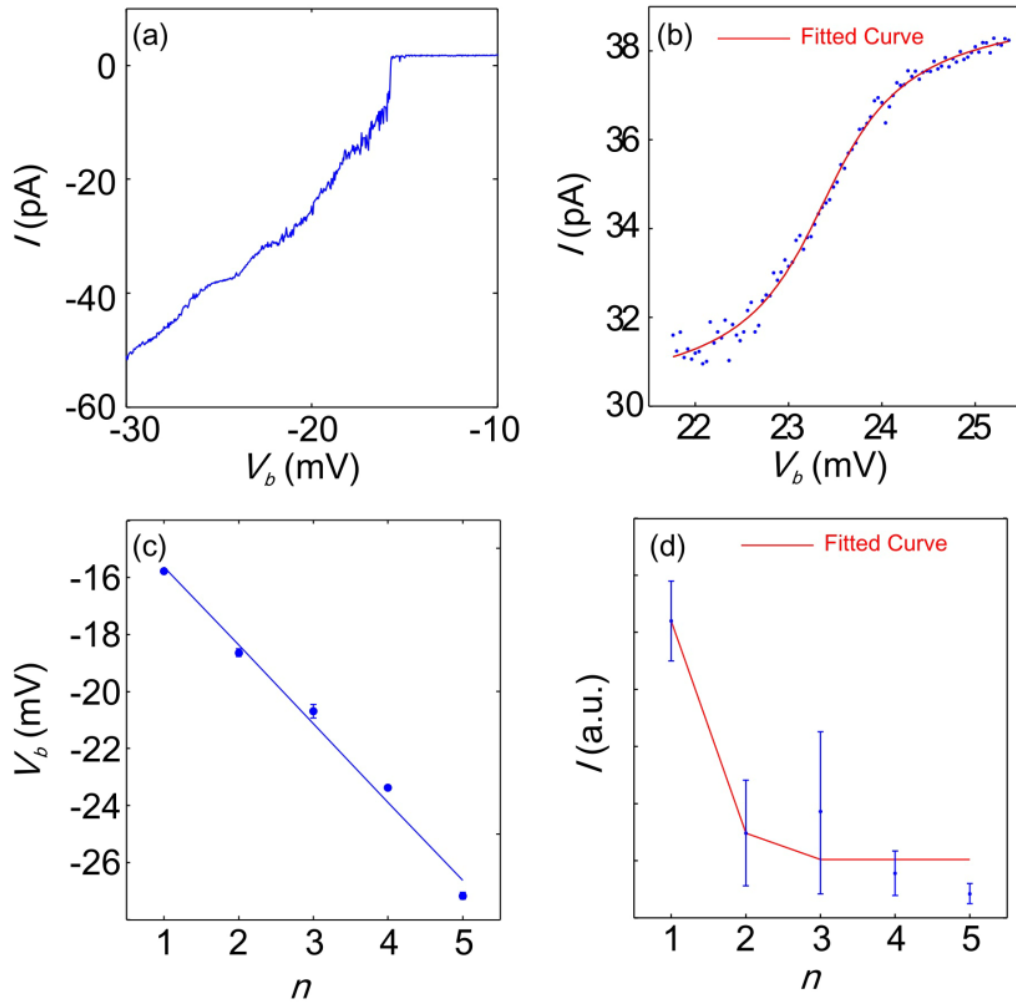


Figure 31 (a) $I - V$ trace at $V_g = 10.85$ V, showing current steps from vibron transitions. (b) Typical fit of the tunnel-coupling Γ_0 broadened current steps. We obtain as the fitting parameters $\Gamma_0 = 1.36$ meV and the step position $V_0 = 23.4$ meV. (c) Peak positions V_0 obtained from the fit as a function of the current steps n . The straight line fit yields a vibrational quantum $\hbar\omega = 1.7$ meV after scaling the bias voltage axis to account for the intersection with the Coulomb diamond slope. (d) Current step heights I_{step} as a function of the current steps n . The fit to the rate equation model yields $\lambda = 3$.

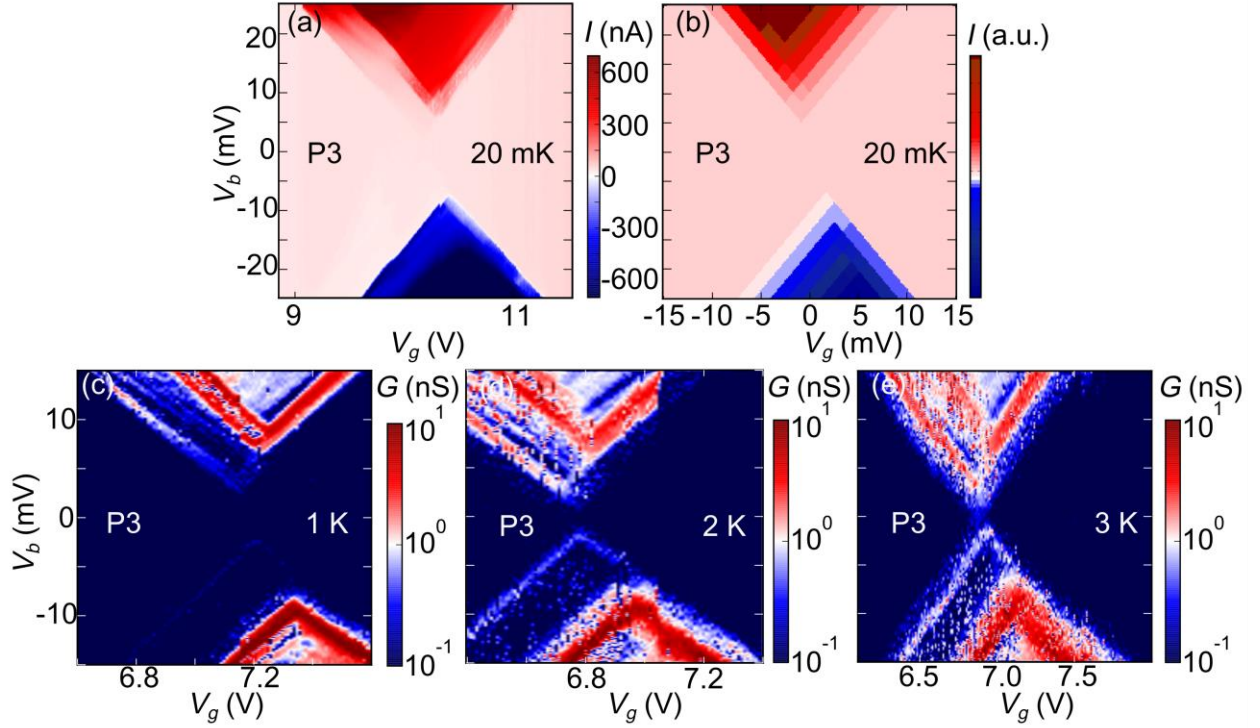


Figure 32 (a) Current stability diagram of redox state transition P3 taken at 20 mK. (b) Simulated current stability diagram from the rate equation model using $\lambda = 3$ and $\Gamma_L = 0.2 \Gamma_R$. Conductance stability diagrams of redox state transition P3 taken at (c) 1 K, (d) 2 K and (e) 3 K.

4.7 Temperature Dependence

Vibrons obey Bose-Einstein statistics and the value of the vibrational quantum $\hbar\omega$ can be independently estimated from the temperature dependence of the transport measurements. At elevated temperatures, the thermal equilibrium population of vibrational excited states with exponentially greater transition rates are increased such that even at low bias, transitions can proceed via these states resulting in current flow. We observe that for device A, the FC gap for redox state transition P3 is lifted at higher temperatures and that the Coulomb diamond edges actually cross at 3 K (Fig. 32 (c-e)). The lifting of the FC gap is also observed for device C at 4 K (Fig. 30 (b, c)). We can independently estimate the value of $\hbar\omega$ from the temperature dependence by fitting the current steps to the equilibrium vibron distribution given by the Bose-Einstein distribution and the derivative of the Fermi distribution:^{10,11}

$$I_{\text{step}}^0 \propto \frac{1}{k_B T} \times 1/(\exp\left(\frac{\hbar\omega}{k_B T}\right) - 1). \quad (21)$$

We fit the current steps at $V_g = 7$ V and $V_b = 7.2$ mV for redox state transition P3 (Fig. 28c) to eqn (21) with $\hbar\omega$ as the fitting parameter and obtain a value of $\hbar\omega = 1.7$ meV, in excellent agreement with our experimentally obtained value (Fig. 33a). Shifts in the gate potential are accounted for by fitting $I - V$ at different temperatures such that the current steps occur at the same V_b . Fig. 33a shows the current steps I_{step}^0 as a function of the temperature T . The black curve is the fit to the data with the fit parameter $\hbar\omega = 1.7$ meV. For comparison, the curves for a value of $\hbar\omega = 0.17$ meV (green) and $\hbar\omega = 17$ meV (red) are also shown. Fig. 33b shows the normalised curves over a larger temperature range.

Such an increase of the current with temperature can be explained through the absorption of one or more vibrational quanta by tunnelling electrons. At elevated temperatures, electronic transport is enabled even in the previously FC blockaded regime because higher vibrational states are populated at elevated temperatures. This increase in current with temperature is in direct contrast with the case for which a Fermi-Dirac distribution in the quantum Coulomb blockade regime is relevant. In such a case, the current $I \propto 1/k_B T$ such that a decrease in current is expected due to thermal broadening in the leads.¹⁰ This temperature dependency of the current has also been similarly observed in suspended carbon nanotubes¹ and single molecule transistors² containing an individual Fe₄ single molecule magnet. There, only excited states that are due to vibrational absorptions displayed an increase of conductance with temperature as compared to electronic excited states which displayed a decrease in conductance with temperature. We note as well that the FC blockade persists even with the application of a 6 T magnetic field, as shown in Fig. 29, thus ruling out a magnetic origin. The temperature dependence of our data is a signature of the bosonic nature of the transitions and is consistent with our interpretation of the FC model.

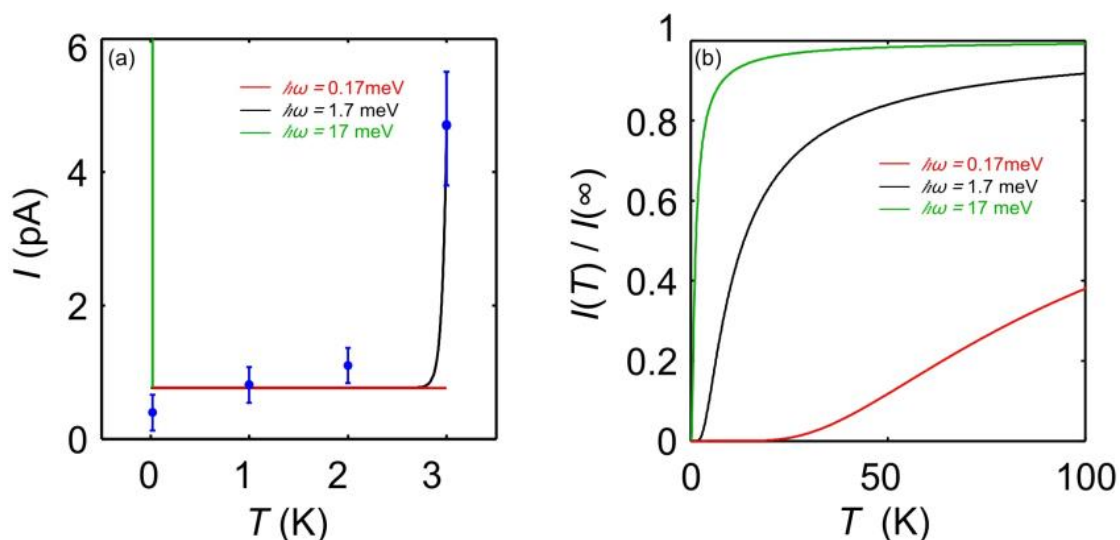


Figure 33 Current step heights as a function of the temperature. The black curve is a fit to eqn (21) given by the Bose-Einstein distribution and the derivative of the Fermi-Dirac distribution. For comparison, the curves for $\hbar\omega = 0.17$ meV (green) and 17 meV (red) are also shown. (b) Normalised curves over a larger temperature range.

4.8 Vibrations vs Oscillations

We can distinguish between two types of vibrons: vibrations or oscillations.^{4,27} Vibrations refer to the internal molecular vibrational modes for which the CM of the molecule remains at rest. Oscillations refer to the CM motion of the molecule as a whole. While internal vibrations couple directly to the charge degree of freedom, CM oscillations instead couple through displacement dependent tunnelling matrix elements. For energies < 10 meV, the coupling strength of CM oscillations is predicted to be insufficient to induce FC blockade.¹¹ This is evident in experiments on gold electrodes based pristine C_{60} single-molecule transistors where no FC blockade are observed for low energy excitations (3 – 7 meV) as these excitations are attributed to pure CM motion of the pristine C_{60} . However, the $\hbar\omega = 1.7$ meV excitations observed in our experiments is accompanied by the internal vibration of the combined C_{60} -pyrene bisadduct system as shown by the DFT simulations (animations available online⁶). Based on our experimental observations and DFT simulations, we attribute the observation of FC blockade in our device to the internal vibrations of the functionalised bisadduct as electron-vibron coupling mediated by internal vibrations are much stronger than electron-vibron coupling mediated by CM oscillations.¹¹

4.9 Avalanche Transport

We have discussed the phenomenon of Franck-Condon blockade caused by strong electron-vibron coupling in our system. If the system also possesses weak vibron relaxation, avalanche transport characterized by strong current fluctuations can occur.^{4,9} Fig. 34(a-f) illustrates the avalanche transport phenomenon. Electron avalanche transport occurs when the vibronic relaxation rate is comparable to the slow transition rates of low lying vibronic states. In the rare event of an electron tunnelling onto the molecule, it is favourable to excite the molecule to an excited state since transition rates involving vibronic excited states are higher. Subsequent transitions can further increase this excitation leading to an avalanche of tunnelling events. The avalanche transport is terminated when the molecule returns to its ground state by tunnelling induced de-excitation or dissipative relaxation.

Fig. 34g shows that avalanche transport leads to fluctuations that persist over the entire bias range corresponding to the vibronic $0 \leftrightarrow 2$ transition. In contrast, field-induced bistabilities occurs only at the initial onset of current.³⁰ For $\beta eV_b < 2\hbar\omega$ ($\beta \sim 0.5$ given by the ratio of the source capacitance and the total capacitance as obtained from the slopes of the Coulomb diamond), the vibron transitions $0 \leftrightarrow 0$ and $0 \leftrightarrow 1$ are suppressed due to FC blockade (Fig. 34(a, d)) and no current flows. At $2\hbar\omega \leq \beta eV_b < 3\hbar\omega$, the $0 \leftrightarrow 2$ transition enters the bias window (Fig. 34(b, e)). While the transition rate is higher compared to the lower lying vibronic transitions, it is still low enough that the system typically remains in the vibronic ground state, resulting in a long wait time with no current. However, occasional electron inelastic tunnelling can excite the molecule to a higher vibronic excited state for which the transition rates are higher, with subsequent electron tunnelling events further increasing the molecular vibronic excitation. Having escaped the ground state, an avalanche of electron tunnelling events through the molecule can now occur and current flows. The avalanche transport terminates when the molecule returns to the vibronic ground state, resulting in another long wait time before the cycle repeats. Within this window, the current fluctuates between a low and high state reflecting the molecular vibronic state (Fig. 34e). For $\beta eV_b \geq$

$3\hbar\omega$, charge transport can proceed through the vibronic $0 \leftrightarrow 3$ transition as the transition rate is sufficiently high for sequential tunnelling leading to current flow (Fig. 34(c, f)).

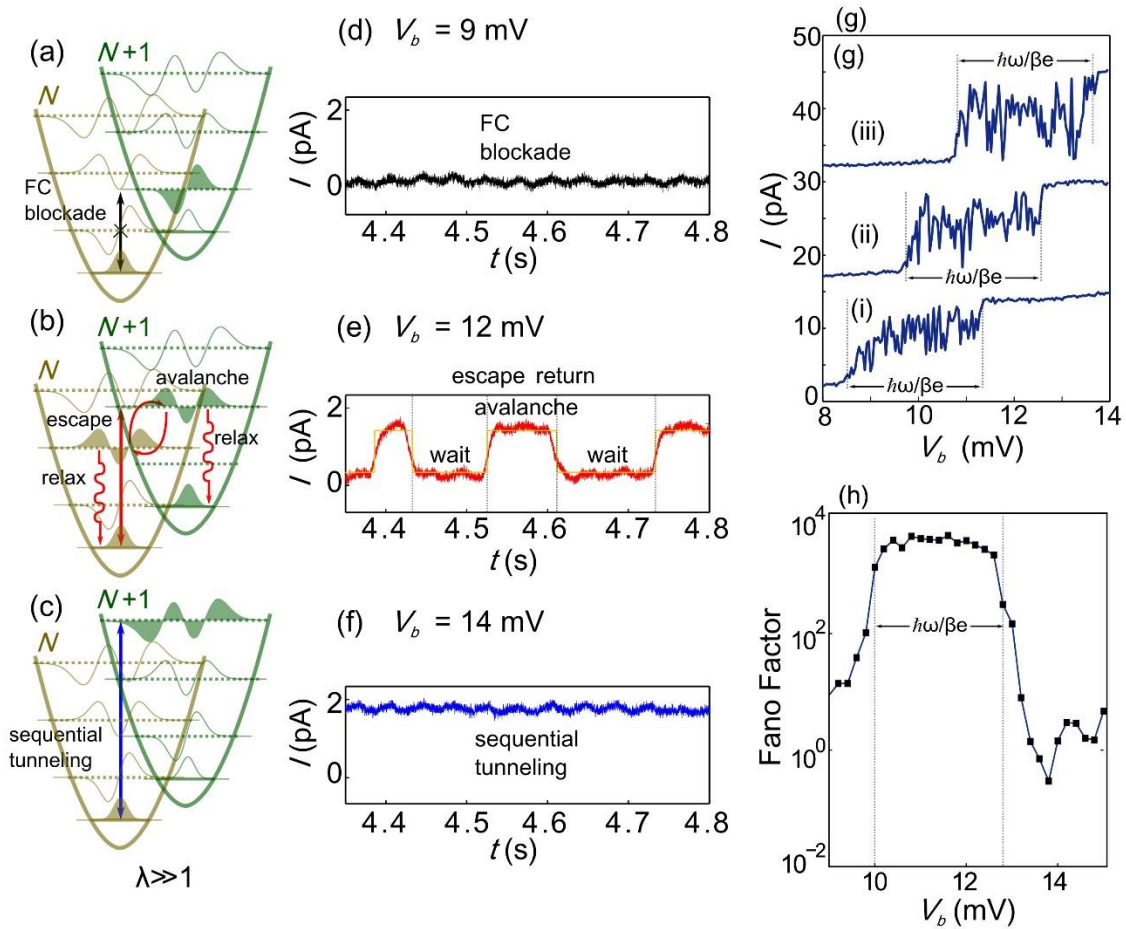


Figure 34 (a-c) Schematics for FC blockade and avalanche transport. (d-f) Current-time traces at $V_b = 9, 12, 14$ mV and $V_g = 10.15$ V. The full current-time trace over which we perform the HMM fit is measured for 20 s with a 100 kHz sampling rate. The orange curve in (e) is part of the full HMM fit. (g) $I - V$ traces at $V_g =$ (i) 10.1, (ii) 10.15, and (iii) 10.2 V. Curves are offset for clarity, +15 pA (ii) and +30 pA (iii). The current fluctuations extend over an applied bias corresponding to $\hbar\omega/\beta e$. (h) Fano factors of the zero-frequency noise measured as a function of V_b at $V_g = 10.15$ V as indicated by the vertical green line in Fig. 28c. Giant Fano factors $\sim 10^3$ reflecting avalanche transport extend over a bias window corresponding to $\hbar\omega/\beta e$, before decreasing to ~ 1 at higher bias where sequential tunnelling sets in.

We characterize the current fluctuations and extract the $0 \leftrightarrow 2$ escape (vibronic transition from the ground state to an excited state) and return (vibronic transition from an excited state back to the ground state) rates by fitting the current-time trace of device A

measured at $V_b = 12$ mV and $V_g = 10.15$ V to a Hidden Markov Model (HMM). We assume a two state stochastic process (orange curve in Fig. 34e).³¹ The software package SMART: Single Molecule Analysis Research Tool³¹ is used for the HMM fit. For each state in the model, the software determines the probability for each point in time; a state probability close to 1 indicates a high probability that the state is occupied. This yields the rate constants k_{ij} , the rate of a transition from state i to j . A combined kinetic and noise model is fitted to each trace and the parameters for the models are determined using maximum likelihood estimation. Typical fits are shown in Fig. 34c and Fig. 35c. We perform the HMM fit for a full current-time trace measured over 20 s with a 100 kHz sampling rate. The escape and return rates are determined using 14 current traces extending over the bias range for which avalanche transport occurs, i.e. $2\hbar\omega \leq \beta eV_b < 3\hbar\omega$, the $0 \leftrightarrow 2$ transition. The value of k_{ij} as determined by the software is in units of per point, which we convert to s^{-1} using the sampling frequency. We obtain an escape rate $1/\tau_e$ of 15 ± 2 s^{-1} . The FC matrix element is estimated by assuming that the current in the high state for Fig. 34e, which corresponds to the vibron transition $0 \leftrightarrow 2$, has a transition probability close to 1. The current $I_{0 \leftrightarrow 2} \approx 1.1$ pA = $e \frac{dN}{dT}$, where e is the electron charge and $\frac{dN}{dT}$ is the electron tunnelling rate corresponding to a transition probability of 1 (We use the value for the current from the HMM fit where the 'low state' is offset to 0). The transition probability associated with the escape rate $1/\tau_e = 15 \pm 2$ s^{-1} is then $1/\tau_e / (\frac{dN}{dt})$ which corresponds to a FC matrix element $M_{0 \leftrightarrow 2} \sim 0.002$ and $\lambda \sim 4$. We obtain a return rate of 22 ± 2 s^{-1} , which places an upper bound of ~ 10 s^{-1} on the dissipative relaxation rate.

The observation of such a slow relaxation rate is indeed surprising especially when compared to typical values measured in time resolved spectroscopy (~ 1 ns⁻¹ to 1 ps⁻¹).³² However, time resolved spectroscopy measurements are generally performed in a solvent where dissipation through solvent ions can occur. Our experimental conditions in low temperature and vacuum will suppress the dissipation rate.³³ Dissipation in single-molecule junctions is mostly dependent on dissipation to the connecting electrodes.^{7,34} Even though the

in-plane thermal conductivity of graphene is known to be exceptionally large, the out-plane thermal conductivity is limited by weak van der Waals interaction between adjacent planes and substrate and can suppress vibronic dissipation from the molecule.³⁵ The molecule-electrode coupling $\Gamma_0 \sim 1$ meV in our devices is indicative of the weak $\pi - \pi$ stacking interactions between the pyrene anchors and the graphene nano-electrode. Other possibilities for the low dissipative relaxation rate includes vibrationally-induced conformation changes where an anharmonic potential with local minimas suppress vibronic dissipation.² Further theoretical work that can determine the factors limiting dissipation should prove interesting but will require a self-consistent calculation of electron-vibron dynamics. Vibronic dissipation to the electrodes depends on the atomistic details at the molecule-electrode interface such as the vibron density of states for which the non-equilibrium distribution is nontrivial.

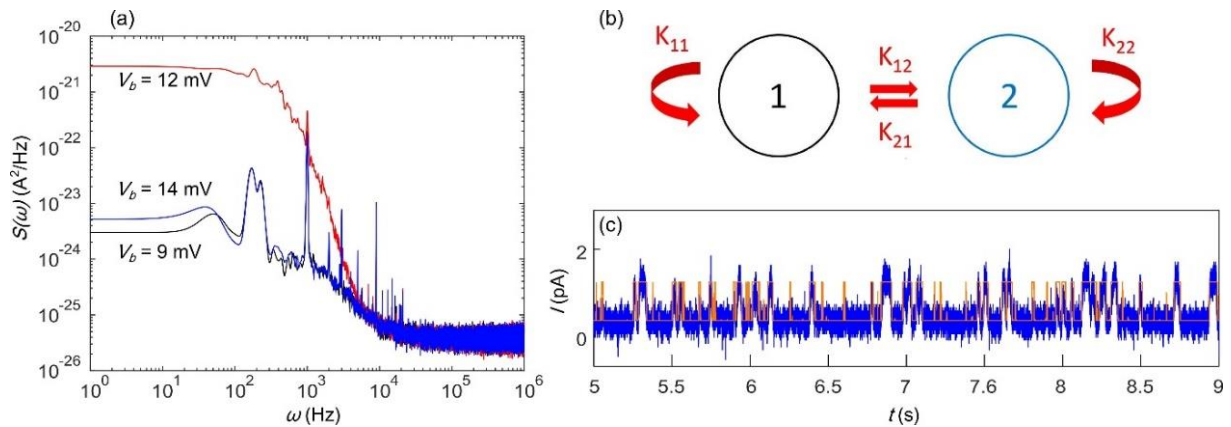


Figure 35 (a) Noise power density for $V_b = 9, 12$ and 14 mV. The cut-off frequency occurs at ~ 100 Hz due to the bandwidth limit of our current amplifier. (b) Schematics of a two state system described by the HMM model, where the rate constants k_{ij} describes the rate of a transition from state i to j . (c) Part of the HMM fit (orange curve) to a current-time trace taken for 20 s at a sampling frequency of 100 kHz.

Electron avalanche transport is also characterized by giant Fano factors on the order of $10^2 - 10^3$ occurring in steps over the bias window corresponding to a vibronic transition $(\hbar\omega/\beta e)$.⁴ The zero frequency Fano factor F for the excess noise $S(0) - S(0)_{V_b=0V}$ indicates the deviation from Poissonian noise where $F = 1$. The noise power density $S(\omega)$ is defined as the Fourier transform of the current-current correlation:

$$S(\omega) = \int_{-\infty}^{\infty} dt e^{i\omega t} \langle \delta I(t + t') \delta I(t') \rangle_{t'}, \quad (\text{XX})$$

where ω is the frequency. In contrast, sequential tunnelling is characterized by $0.5 < F < 1$ depending on the ratio of the molecule-electrode couplings Γ_L and Γ_R .³⁶ Higher order co-tunnelling processes such as inelastic co-tunnelling is known to result in super-Poissonian noise with F up to 8.³⁷ Fig. 34h shows the zero frequency Fano factors as a function of V_b determined at $V_g = 10.15$ V indicated by the vertical green line in Fig. 28c. For $10 \leq V_b \leq 13$ meV, the Fano factors increase to $\sim 10^3$ which reflects the current fluctuations due to avalanche transport. These giant Fano factors too persist over a bias window corresponding to $\hbar\omega/\beta e$ and returns to values of ~ 1 when $V_b = 13.4$ mV which is sufficient to lift the FB blockade, as expected for sequential transport.

4.10 Conclusion

Using functionalised C₆₀ bisadduct and graphene nano-electrodes, we demonstrate single-molecule transistors that exhibits redox-dependent FC blockade and avalanche transport. We observe HOMO dominated transport for the bisadducts in contrast to LUMO dominated transport for pristine C₆₀.³⁴ While doping-induced variations in the Fermi-level of the graphene electrodes and charge traps in the oxide layer can influence the electrochemical potential alignment of the molecule with respect to the Fermi-level of the graphene nano-electrodes, the functionalisation of C₆₀ with pyrene anchors can modify electron delocalisation and energy levels leading to HOMO dominated transport. Theoretical calculations have suggested that modification of electron delocalisation and energies through attaching side groups to the molecule can be used to tune the thermopower of single-molecule junctions.^{38,39} Moreover, thermoelectric efficient is maximised when charge transport across a junction occurs through a single level with low vibrational heat conductance. Therefore, the extremely long vibronic lifetime observed offers the potential for both fundamental study of quantized motion and thermal transport on the nanoscale, and practical applications in single-molecule devices.³⁹

References

1. Lüffe, M., Koch, J. & von Oppen, F. Theory of vibrational absorption sidebands in the Coulomb-blockade regime of single-molecule transistors. *Phys. Rev. B* **77**, 125306 (2008).
2. Galperin, M., Ratner, M. a & Nitzan, A. Molecular transport junctions: vibrational effects. *J. Phys. Condens. Matter* **19**, 103201 (2007).
3. Osorio, E. a. *et al.* Addition energies and vibrational fine structure measured in electromigrated single-molecule junctions based on an oligophenylenevinylene derivative. *Adv. Mater.* **19**, 281–285 (2007).
4. Koch, J. & Von Oppen, F. Franck-Condon blockade and giant Fano factors in transport through single molecules. *Phys. Rev. Lett.* **94**, (2005).
5. Burzurí, E. *et al.* Sequential electron transport and vibrational excitations in an organic molecule coupled to few-layer graphene electrodes. *ACS Nano* **10**, 2521–2527 (2016).
6. Lau, C. S. *et al.* Redox-dependent Franck–Condon blockade and avalanche transport in a graphene–fullerene single-molecule transistor. *Nano Lett.* **16**, 170–176 (2016).
7. Pascual, K. J. F. and J. I. Effects of electron–vibration coupling in transport through single molecules. *J. Phys. Condens. Matter* **24**, 394002 (2012).
8. Seldenthuis, J. S., van der Zant, H. S. J., Ratner, M. A. & Thijssen, J. M. Vibrational excitations in weakly coupled single-molecule junctions: A computational analysis. *ACS Nano* **2**, 1–9 (2010).
9. Koch, J., von Oppen, F. & Andreev, a. Theory of the Franck-Condon blockade regime. *Phys. Rev. B* **74**, 205438 (2006).
10. Leturcq, R. *et al.* Franck–Condon blockade in suspended carbon nanotube quantum dots. *Nat. Phys.* **5**, 327–331 (2009).

11. Burzurí, E. *et al.* Franck-Condón blockade in a single-molecule transistor. *Nano Lett.* **14**, 3191–3196 (2014).
12. Maggini, M., Scorrano, G. & Prato, M. Addition of azomethine ylides to C₆₀: synthesis, characterization, and functionalization of fullerene pyrrolidines. *J. Am. Chem. Soc.* **115**, 9798–9799 (1993).
13. Yee, S. K., Malen, J. a., Majumdar, A. & Segalman, R. a. Thermoelectricity in fullerene-metal heterojunctions. *Nano Lett.* **11**, 4089–4094 (2011).
14. Mol, J. A. *et al.* Graphene-porphyrin single-molecule transistors. *Nanoscale* **7**, 13181–13185 (2015).
15. Kubatkin, S. *et al.* Single-electron transistor of a single organic molecule with access to several redox states. *Nature* **425**, 698–701 (2003).
16. Ke, S.-H., Baranger, H. & Yang, W. Addition energies of fullerenes and carbon nanotubes as quantum dots: The role of symmetry. *Phys. Rev. Lett.* **91**, 116803 (2003).
17. Lambert, C. J. Basic concepts of quantum interference and electron transport in single-molecule electronics. *Chem. Soc. Rev.* **44**, 875–888 (2015).
18. Liu, Z.-F. *et al.* Control of single-molecule junction conductance of porphyrins via a transition-metal center. *Nano Lett.* **14**, 5365–70 (2014).
19. Heid, R., Pintschovius, L. & Godard, J. M. Eigenvectors of internal vibrations of C₆₀: Theory and experiment. *Phys. Rev. B* **56**, 5925–5936 (1997).
20. Lansbergen, G. P. *et al.* Lifetime-enhanced transport in silicon due to spin and valley blockade. *Phys. Rev. Lett.* **107**, 136602 (2011).
21. Kuzmany, H., Pfeiffer, R., Hulman, M. & Kramberger, C. Raman spectroscopy of fullerenes and fullerene–nanotube composites. *Philos. Trans. R. Soc. London A Math. Phys. Eng. Sci.* **362**, 2375–2406 (2004).

22. Martin, M. C., Koller, D., Rosenberg, A., Kendziora, C. & Mihaly, L. Infrared and Raman evidence for dimers and polymers in RbC₆₀. *Phys. Rev. B* **51**, 3210–3213 (1995).
23. Fuechsle, M. *et al.* A single-atom transistor. *Nat. Nanotechnol.* **7**, 242–246 (2012).
24. Bailey, S. *et al.* A study of planar anchor groups for graphene-based single-molecule electronics. *J. Chem. Phys.* **140**, 054708 (2014).
25. Lannoo, M., Baraff, G. A., Schlüter, M. & Tomanek, D. Jahn-Teller effect for the negatively charged C₆₀ molecule: Analogy with the silicon vacancy. *Phys. Rev. B* **44**, 12106–12108 (1991).
26. O'Brien, M. C. M. The Jahn–Teller effect: An introduction and current review. *American Journal of Physics* **61**, 688 (1993).
27. Koch, J., Von Oppen, F., Oreg, Y. & Sela, E. Thermopower of single-molecule devices. *Phys. Rev. B - Condens. Matter Mater. Phys.* **70**, 1–12 (2004).
28. Van Der Heijden, J. *et al.* Probing the spin states of a single acceptor atom. *Nano Lett.* **14**, 1492–1496 (2014).
29. Foxman, E., McEuen, P. & Meirav, U. Effects of quantum levels on transport through a Coulomb island. *Phys. Rev. B* **47**, 20–23 (1993).
30. Secker, D. *et al.* Resonant vibrations, peak broadening, and noise in single molecule contacts: The nature of the first conductance peak. *Phys. Rev. Lett.* **106**, 3–6 (2011).
31. Greenfeld, M., Pavlichin, D. S., Mabuchi, H. & Herschlag, D. Single molecule analysis research tool (SMART): An integrated approach for analyzing single molecule data. *PLoS One* **7**, (2012).
32. Laubereau, A., Von Der Linde, D. & Kaiser, W. Direct measurement of the vibrational lifetimes of molecules in liquids. *Phys. Rev. Lett.* **28**, 1162–1165 (1972).
33. Kuznetsov, A. M. & Ulstrup, J. Single-molecule electron tunnelling through multiple

- redox levels with environmental relaxation. *J. Electroanal. Chem.* **564**, 209–222 (2004).
34. Schulze, G. *et al.* Resonant electron heating and molecular phonon cooling in single C₆₀ junctions. *Phys. Rev. Lett.* **100**, 136801 (2008).
 35. Pop, E., Varshney, V. & Roy, A. K. a. K. Thermal properties of graphene: Fundamentals and applications. *MRS Bull.* **37**, 1273–1281 (2012).
 36. Onac, E., Balestro, F., Trauzettel, B., Lodewijk, C. & Kouwenhoven, L. Shot-noise detection in a carbon nanotube quantum dot. *Phys. Rev. Lett.* **96**, 026803 (2006).
 37. Sukhorukov, E. V., Burkard, G. & Loss, D. Noise of a quantum-dot system in the cotunneling regime. **63**, 20 (2000).
 38. Kim, Y., Jeong, W., Kim, K., Lee, W. & Reddy, P. Electrostatic control of thermoelectricity in molecular junctions. *Nat Nano* **9**, 881–885 (2014).
 39. Reddy, P., Jang, S.-Y., Segalman, R. a & Majumdar, A. Thermoelectricity in molecular junctions. *Science* **315**, 1568–1571 (2007).

Chapter 5: Final Conclusion and Outlook

The ultimate miniaturization of electronic devices will heavily depend on precise control over sub-nanometre distances and the reproducible production of identical building blocks. Molecular electronics is therefore well positioned to fulfil the needs for scaling down of electronics. While it may be that molecular electronics cannot replace silicon technologies entirely, molecular devices can complement silicon electronics by providing new functionalities beyond the scope of conventional solid-state devices through clever chemical design and synthesis. Furthermore, single-molecule devices offer an appropriate platform for fundamental studies such as quantum transport. However, early efforts in building single-molecule devices have been hampered by device variability and the lack of control over physical and chemical properties of the molecular junction.

Carbon based materials offer an alternative platform for the fabrication of robust room temperature operable single-molecule devices by overcoming many of the limitations faced by gold nano-electrodes. In this thesis, we first demonstrated a novel approach for the fabrication of graphene nano-electrodes based on combining feedback controlled electroburning and plasma etching. The production of these nano-gaps using large area CVD graphene allows for scalability and compatibility with conventional silicon technologies. Using our graphene nano-gap arrays, we next demonstrate a device architecture for reproducible production of room temperature operable porphyrin based single-molecule transistors. The modular design of our porphyrin molecules are tailored for specific device functionalities. Finally, we utilised the same device architecture as a platform for fundamental investigations of redox dependent electron-vibron coupling and avalanche transport in a graphene-fullerene single-molecule transistor.

There are many improvements that can be made to the devices reported in this thesis. A key next step is to attain even greater control over the graphene nano-gap fabrication. The precise control over nano-gap sizes down to sub-nanometre lengths will decrease device variability and enable improved molecule-electrode contact. The molecule-electrode coupling

is vital to the single-molecule junction properties. It is also well known that graphene edges determine the magnetic, electrical and optical properties of graphene.¹ Knowledge of the graphene edge passivation will enable the design of specific molecular anchoring groups for tuneable molecule-electrode coupling. While the feedback controlled electroburning process allows for the fabrication of sub 10 nm nano-gaps, it is difficult to control the nano-gap sizes obtained with sub-nm precision. The graphene edge configuration and passivation remains unknown.

A better understanding of the electroburning process is required in order to improve the fabrication process. The atomistic details of the electroburning process can be revealed through the use of transmission electron microscopy (TEM). The devices can be fabricated on a TEM compatible silicon nitride substrate where windows can be cut using focused ion beam or reactive ion etching. The graphene 'bowtie' structure is then suspended over these windows which will allow in situ characterization during the electroburning process. The electroburning can also be performed under different gas pressures and types to study edge passivation of graphene. One can imagine that the graphene edges might be H₂ passivated if the electroburning is performed in a hydrogen rich environment.

It has already been shown that electroburning without the use of a feedback has a much higher yield in vacuum than in ambient conditions.² It is likely that performing our feedback controlled electroburning process in vacuum can provide greater control over the nano-gap sizes and increase the production yield. Currently, the feedback controlled electroburning process has a rather low throughput as each nano-gap has to be burned separately. The development of a parallel fabrication process will contribute greatly towards scalable applications.

An improved understanding of the electroburning process will enable more precise fabrication of additional side gate electrodes. The addition of graphene side gates can enhance the gate coupling β allowing access to more redox states. Three terminal graphene nano-electrodes has been demonstrated using feedback controlled electroburning, but with

low yield and control over the nano-gaps.³ Integrating other two dimensional materials such as hexagonal boron nitride not only also offers possibilities for enhancing β and reducing charge traps for more reproducible devices, but also has the potential for creating flexible and transparent devices for applications.

The molecules described in this thesis, the porphyrins and C₆₀ fullerenes, are comparatively basic members in their families.^{4,5} The synthetic chemistry for both porphyrins and fullerenes have been extensively studied and are well developed. More complex porphyrin and fullerene molecules can be synthesized including dimers and trimers which are suitable for length dependent transport measurements. Side groups with different properties can be added for varied device functionalities. The porphyrin ligand can bind to an extensive list of metallic ions such as Cu, Mn, Co and Fe etc. This opens up interesting possibilities for experiments probing the spin dependence and charge transport through porphyrins with different metallic cations. For example, one can investigate the magnetic anisotropy of high spin complexes such as Mn porphyrin compared to low spin complexes such as Zn porphyrins. Dimer and trimer structures with combinations of different cations may lead to novel transport properties. Endohedral fullerenes have been proposed for electrostatic encapsulation of molecular species which can preserve chemical integrity and control intermolecular coupling for parallel assembly.⁶ N@C₆₀ has attracted attention for its potential applications in fields such as quantum information processing and spintronics because of its long spin lifetime even at room temperature. The long spin lifetime is a result of being largely immune to environmental decoherence due to the shielding by the cage.^{7,8} The manipulation of the magnetic properties of a system of paramagnetic metallofullerene Sc₃C₂@C₈₀ has been demonstrated by attaching the fullerene to a nitroxide radical serving as a magnetic switch for the electron spin resonance signals of the Sc₃C₂@C₈₀ through spin-spin coupling.⁹ This spin-spin interaction can even be tuned by controlling the distance between the two spin centres.

The examples for future work described here are but the tip of the iceberg. The development of molecular electronics will depend on a multidisciplinary effort involving

experimentalists and theorists from fields such as physics, chemistry, material science and electrical engineering. While still far from practical applications, molecular electronics hold enormous potential. As Richard Feynman said, “there’s plenty of room at the bottom.”

References

1. Castro Neto, A. H. . *et al.* The electronic properties of graphene. *Rev. Mod. Phys.* **81**, 109–162 (2009).
2. Nef, C. *et al.* High-yield fabrication of nm-size gaps in monolayer CVD graphene. *Nanoscale* **6**, 7249–54 (2014).
3. Puczkarski, P. *et al.* Three-terminal graphene single-electron transistor fabricated using feedback-controlled electroburning. *Appl. Phys. Lett.* **107**, (2015).
4. Jurow, M., Schuckman, A. E., Batteas, J. D. & Drain, C. M. Porphyrins as molecular electronic components of functional devices. *Coord. Chem. Rev.* **254**, 2297–2310 (2010).
5. Guldi, D. M., Illescas, B. M., Atienza, C. M., Wielopolski, M. & Martín, N. Fullerene for organic electronics. *Chem. Soc. Rev.* **38**, 1587–1597 (2009).
6. Lörtscher, E. Wiring molecules into circuits. *Nat. Nanotechnol.* **8**, 381–4 (2013).
7. Harneit, W. Fullerene-based electron-spin quantum computer. *Phys. Rev. A* **65**, 1–6 (2002).
8. Nikawa, H. *et al.* The effect of atomic nitrogen on the C60 cage. *Chem. Commun.* **46**, 631–633 (2010).
9. Wu, B. *et al.* Molecular magnetic switch for a metallofullerene. *Nat Commun* **6**, (2015).

Appendix I: Feedback Controlled Electroburning Codes

Included in this appendix is the python QTLab code and Adwin code for performing the feedback controlled electroburning of graphene nano-gaps discussed in Chapter 2.

Python Code:

```
base = 'Filename'

cascade = qt.instruments.create('cascade','Cascade_Summit_12000')

adwin_gold_II = qt.instruments.create('adwin_gold_II','ADwin_Gold_II',dev=1)

femto_dlpca_200 = qt.instruments.create('femto_dlpca_200','FEMTO_DLPCA_200',dev=1)

fn1 = adwin_gold_II.compile_process('C:\scripts\ADwin\Aaroneb1.bas',process=1)

fn2 = adwin_gold_II.compile_process('C:\scripts\ADwin\AaronIV1.bas',process=2)

adwin_gold_II.load_process(fn1)

adwin_gold_II.load_process(fn2)

#adwin_gold_II.set('data1',y,data_type=types.IntType)

# Set ramping up, par10, and ramping down, par11 speed

# in units of 1.5 V/s

adwin_gold_II.set('fpar10',0.5)

adwin_gold_II.set('fpar11',150)
```

```
# Set drop in G for which to stop ramping the voltage

adwin_gold_II.set('fpar12',4)

# Set voltage over which to measure the drop in G

# in units of 300 uV

adwin_gold_II.set('par12',50)

start_row = 1

stop_row = 30

row_pitch = -250

row_numbers = range(start_row,stop_row+1)

row_positions = [row_pitch*i for [i,v] in enumerate(row_numbers)]

start_column = 'a'

stop_column = 'r'

column_pitch = 500

column_letters = [chr(i) for i in range(ord(start_column),ord(stop_column)+1)]

column_positions = [column_pitch*i for [i,v] in enumerate(column_letters)]

gain = 'L9'

number_of_samples = 20000

burn_gain = 'L4'
```

```
V_R = 0.1
```

```
R_crit = 500e6
```

```
V_crit = [39000,38000,37000,36000]
```

```
dldV_crit = [4,6,6.0,8.0,10.0]
```

```
V_min = -0.4
```

```
V_max = 0.4
```

```
step_out = 100
```

```
def measure_R(V,gain,number_of_samples):
```

```
    qt.msleep(1)
```

```
    adwin_gold_II.set('par22',voltage_to_digit(V))
```

```
    adwin_gold_II.set('par23',number_of_samples)
```

```
    adwin_gold_II.start_process(2) #starts process 2
```

```
    qt.msleep((number_of_samples+5)*1e-5)
```

```
    adwin_gold_II.set('par22',voltage_to_digit(0))
```

```
    R = V/digit_to_current(adwin_gold_II.get('par21'),gain)
```

```
    adwin_gold_II.start_process(2) #starts process 2
```

```
    qt.msleep((number_of_samples+5)*1e-5)
```

```
    return R
```

```
def burn(gain,burn_gain,V_crit,dldV_crit,data_burn,n):
```

```

femto_dlpca_200.set('gain',burn_gain)

qt.msleep(1)

adwin_gold_II.start_process(1)

fin = 0

while not fin:

    fin = adwin_gold_II.get('par6')

    qt.msleep(1)

count = adwin_gold_II.get('par3')

I = adwin_gold_II.get('data2')[:count-1]

V = adwin_gold_II.get('data3')[:count-1]

if ((max(V)<V_crit[0]) and (max(V)>V_crit[1])):

    adwin_gold_II.set('fpar12',dIdV_crit[1])

elif ((max(V)<V_crit[1]) and (max(V)>V_crit[2])):

    adwin_gold_II.set('fpar12',dIdV_crit[2])

elif ((max(V)<V_crit[2])and (max(V)>V_crit[3])):

    adwin_gold_II.set('fpar12',dIdV_crit[3])

    adwin_gold_II.set('par12',50)

elif (max(V)<V_crit[3]):

    adwin_gold_II.set('fpar12',dIdV_crit[4])

    adwin_gold_II.set('par12',50)

else:

```

```

    adwin_gold_II.set('fpar12',dIdV_crit[0])

    adwin_gold_II.set('par12',50)

data_burn.add_data_point(V, n*ones(size(V)), I)

data_burn.new_block()

#plot_burn.update()

femto_dlpca_200.set('gain',gain)

qt.msleep(1)

print max(V)

if (max(V)>55001):

    return False

#elif ((n==1) & (max(V)<39001)):

    #return False

else:

    return True

def measure_IV(number_of_samples,V_min,V_max,step_out,base):

    adwin_gold_II.set('par23',number_of_samples)

    out1 = linspace(0,V_max,step_out)

    out2 = append(out1,linspace(V_max,V_min,2*step_out))

    out = append(out2,linspace(V_min,0,step_out))

    data_IV = create_IV_file(base,r,c)

```

for o in out:

```
adwin_gold_II.set('par22',voltage_to_digit(o))
```

```
qt.mstart()
```

```
adwin_gold_II.start_process(2) #starts process 2
```

```
qt.msleep(0.205)
```

```
V = digit_to_voltage(adwin_gold_II.get('par22')) #get data par21
```

```
I = digit_to_current(adwin_gold_II.get('par21'),gain) #get data par22
```

```
data_IV.add_data_point(V, I)
```

```
data_IV.close_file()
```

```
def move(row_position,column_position):
```

```
cascade.set('position',[column_position,row_position,0],rel=True)
```

```
qt.msleep(1)
```

```
def voltage_to_digit(V):
```

```
return int(65535/20.0*(V+10.0))
```

```
def digit_to_voltage(d):
```

```
return (d*20.0/65535 - 10.0)
```

```
def digit_to_current(d,gain):
```

```

g = 10.0**int(gain[1:])

return (d*20.0/65535 - 10.0)/g

def create_burn_file(base,r,c):

    data_burn = qt.Data(name='%s_burn_%s%d' % (base,c,r))

    data_burn.add_coordinate('V')

    data_burn.add_coordinate('n')

    data_burn.add_value('I')

    plot_burn = qt.Plot2D(data_burn, name='burn current', coorddim=0, valdim=2, traceofs=0)

    return data_burn

def create_IV_file(base,r,c):

    data_IV = qt.Data(name='%s_IV_%s%d' % (base,c,r))

    data_IV.add_coordinate('V')

    data_IV.add_value('I')

    plot_IV = qt.Plot2D(data_IV, name='IV current', coorddim=0, valdim=1, traceofs=0)

    return data_IV

femto_dlpca_200.set('gain',gain)

femto_dlpca_200.set('coupling','DC')

qt.msleep(1)

r_old = 0

```

```

c_old = 0

cascade.set('contact',1)

for [j,c] in enumerate(column_letters):

    for [i,r] in enumerate(row_numbers):

        move(row_positions[i]-r_old,column_positions[j]-c_old)

        r_old = row_positions[i]

        c_old = column_positions[j]

        R = abs(measure_R(V_R,gain,number_of_samples))

        print R

        cont = True

        if (R < R_crit):

            data_burn = create_burn_file(base,r,c)

            n = 1

            while ((R < R_crit) and n<400 and cont):

                cont = burn(gain,burn_gain,V_crit,dldV_crit,data_burn,n)

                R = abs(measure_R(V_R,gain,number_of_samples))

                n = n+1

                print R

                print n

            if cont:

                measure_IV(number_of_samples,V_min,V_max,step_out,base)

```

Adwin Code: Feedback

```
#Include ADwinGoldII.inc
```

```
Dim in As Long 'Input current'
```

```
Dim out As Float 'Output voltage'
```

```
Dim count As Long 'Counter'
```

```
Dim diff1 As Float 'Current Differential'
```

```
Dim Data_2[49149] As Long 'Current'
```

```
Dim Data_3[49149] As Long 'Voltage'
```

```
Dim f[0] As Long
```

```
Dim f[1] As Long
```

```
Dim f[2] As Long
```

```
Dim f[3] As Long
```

```
Dim f[4] As Long
```

```
Dim f[5] As Long
```

```
Dim f[6] As Long
```

```
Init:
```

```
Processdelay = 60000 '60000 = 5kHz'
```

```
out = 32767 'Set Output Voltage to 0 (32767=0)'
```

```
count = 1 'Starts Count'
```

```
diff1 = 0 'Sets Current Differential to 0'
```

```
Par_5 = 0 'Set Event Flag to false'
```

Par_6 = 0 'Set Ramp End Flag to false'

Event:

DAC(1,out) 'Outputs Source Voltage as defined by out'

in = ADC(1)

Par_1 = in 'Set Global Input Current'

Par_2 = out

Par_3 = count

Par_4 = diff1

Data_2[count] = in 'Save Current'

Data_3[count] = out 'Save Voltage'

f[0] = Data_2[count]

f[1] = Data_2[count-Par_12]

f[2] = Data_2[count-2*Par_12]

f[3] = Data_2[count-3*Par_12]

f[4] = Data_2[count-4*Par_12]

f[5] = Data_2[count-5*Par_12]

f[6] = Data_2[count-6*Par_12]

If (count > 10*Par_12) Then

diff1 = (f[0]-f[1])/Par_12

'diff1 = ((49/20)*f[0]-6*f[1]+(15/2)*f[2]-(20/3)*f[3]+(15/4)*f[4]-(6/5)*f[5]+(1/6)*f[6])/Par_12'

'Set diff1 as the current differential over range defined by Par_12, after 10000 counts'

EndIf

If ((Par_5 = 0) And (diff1 < -FPar_12)) Then 'If event flag check and diff1 is less than value defined by negative of FPar_12'

Par_5 = 1 'Set event Flag to true'

EndIf

If ((out > 38000) And (in < 33000)) Then

Par_5 = 1

EndIf

If (Par_5 = 1) Then

out = out - FPar_11 'Ramp DOWN of Voltage, rate defined by Par_11'

Else

out = out + FPar_10 'Ramp UP of Voltage, rate defined by Par_12'

EndIf

If (out < 32767) Then 'When voltage ramp down to below 0 volts (32767=0)'

out = 32767 'Output Voltage is set to 0'

Par_6 = 1 'Ramp End Flag set to true'

EndIF

If (out > 55535) Then 'If Output Voltage > threshold value'

Par_5 = 1 'Set event flag to true for voltage ramp down'

EndIf

```
count = count + 1 'Increase counter'
```

```
If (Par_6 = 1) Then End 'Programe completed'
```

Adwin Code: Measure

```
#Include ADwinGoldII.inc
```

```
Dim count,in As Long
```

```
'par22 = Output voltage'
```

```
'par23 = No. of counts of samples taken'
```

```
'par21 = Averaged Current'
```

```
Init:
```

```
DAC(1,32767)
```

```
Processdelay = 3000
```

```
in = 0
```

```
count = 0
```

```
Event:
```

```
Inc(count)
```

```
in = in + ADC(1)
```

```
If (count > Par_23) Then End
```

```
Finish:
```

```
Par_21 = in/count
```

Appendix II: Simmons Model Fit

Included in this appendix are the Matlab codes for performing the Simmons model $I - V$ fit discussed in Chapter 2.

Matlab Code: Simmons Function

```
function I = simmons(V,phi,alpha,d)

beta = 10.25; %eV nm

for i = 1:length(V)

    phi_L = (1+alpha)*phi+V(i)/2;

    phi_R = (1-alpha)*phi-V(i)/2;

    Ex = [-2*phi:1e-2:abs(V(i)/2)];

    %electron energies

    nL = -(Ex-V(i)/2).*(Ex-V(i)/2<0);

    %number of electrons on left,

    nR = -(Ex+V(i)/2).*(Ex+V(i)/2<0);

    %Distribution of electron energies on right

    F = [];

    for j = 1:length(Ex)

        if Ex(j) > phi_R

            F(j) = -d*2/3*(phi_L-Ex(j))^(3/2)/(phi_R-phi_L);

        elseif Ex(j) > phi_L
```

```
F(j) = d*2/3*(phi_R-Ex(j))^(3/2)/(phi_R-phi_L);
```

```
else
```

```
F(j) = d*2/3*((phi_R-Ex(j))^(3/2)-(phi_L-Ex(j))^(3/2))/(phi_R-phi_L);
```

```
end
```

```
end
```

```
I(i) = trapz((nL-nR).*exp(-beta*F));
```

```
end
```

```
I = real(I'/max(I));
```

Matlab Code: Simmons $I - V$ fit

```
clear;
```

```
close all;
```

```
s_A = 1;
```

```
A_L = -100;
```

```
A_U = 100;
```

```
s_I0 = 0.01;
```

```
I0_L = -1;
```

```
I0_U = 1;
```

```
s_alpha = 0.01;
```

```
alpha_L = -1;
```

```

alpha_U = 1;

s_d = 2;

d_L = 0;

d_U = 5;

s_phi = 0.3;

phi_L = 0.1;

phi_U = 4;

pth = 'Pathname';

dr = dir([pth '*filename*']);

for i = 1:length(dr)

    fn = [pth '/' dr(i).name '/' dr(i).name '.dat'];

    dat = importdata(fn,'\t',15);

    data = dat.data;

    V = data(98:299,1);

    I = -data(98:299,2);

    R(i) = I(:)\V(:);

    [f,g] = fit(V,I*1e9,'A*simmons(x,phi,alpha,d)',...

        'Startpoint',[s_A,s_alpha,s_d,s_phi],...

        'Lower',[A_L,alpha_L,d_L,phi_L],...

```

```
'Upper',[A_U,alpha_U,d_U,phi_U],...
```

```
'MaxFunEval',3000,...
```

```
'MaxIter',500,...
```

```
'TolFun',1e-16,...
```

```
'TolX',1e-18,...
```

```
'Display','iter')
```

```
figure(i);
```

```
plot(V,I*1e9)
```

```
hold on
```

```
plot(f,'r')
```

```
D(i)= f.d;
```

```
Coeff(i)=g.rsquare;
```

```
B(i) = f.phi;
```

```
T = strsplit(dr(i).name,'_');
```

```
title(T{end},'FontSize',20,'FontWeight','bold');
```

```
set(gca, 'FontSize', 14);
```

```
mtextbox1 = uicontrol('style','text');
```

```
mtextbox2 = uicontrol('style','text');
```

```

mtextbox3 = uicontrol('style','text');

set(mtextbox1,'String',D(i), 'FontSize', 13, 'Position', [20 80 60 20]);

set(mtextbox2,'String',B(i), 'FontSize', 13, 'Position', [20 50 60 20]);

set(mtextbox3,'String',Coeff(i), 'FontSize', 13, 'Position', [20 20 60 20]);

xlabel('Voltage (V)','FontSize',18);

ylabel('Current (nA)','FontSize',18);

xlim([-0.51 0.51]);

grid

saveas(gcf,T{end})

saveas(gcf,T{end},'jpg')

close all

end

close all;

plot(D,R,'o');

set(gca, 'FontSize', 14);

title('Diameter vs Resistance','FontSize',20,'FontWeight','bold');

ylabel('Resistance (Ohms)','FontSize',18);

xlabel('Diameter (nm)','FontSize',18);

saveas(gcf,'Resistance diameter plot','jpg');

saveas(gcf,'Resistance diameter plot');

```

```
close all;

semilogy(D,R,'o');

set(gca, 'FontSize', 14);

title('Diameter vs Resistance Log Plot','FontSize',20,'FontWeight','bold');

ylabel('Resistance (Ohms)','FontSize',18);

xlabel('Diameter (nm)','FontSize',18);

saveas(gcf,'log Resistance diameter plot','jpg');

saveas(gcf,'log Resistance diameter plot');
```

```
close all;

plot(B,R,'o');

set(gca, 'FontSize', 14);

title('Barrier vs Resistance','FontSize',20,'FontWeight','bold');

ylabel('Barrier (eV)','FontSize',18);

xlabel('Diameter (nm)','FontSize',18);

saveas(gcf,'Resistance Phi plot','jpg');

saveas(gcf,'Resistance Phi plot');
```

Appendix III: Rate Equation Model

Included in this appendix is the Matlab code for simulating the rate equation model discussed in Chapter 4.

Matlab Code: Rate Equation Model

```
clear all

close all;

kb = 8.62e-2; %boltzman constant

lambda = 3; %electron phonon coupling

t_0 = 1; %tunnel coupling

t_L = 1*t_0; % Left

t_R = 0.2*t_0; % Right

Epho = 1.7; %Phonon energy

tau = 1e-10; %Equilibrium phonon lifetime

T = 20e-3; %Temperature

n = [0 1];

rho = 1; %density of states of lead

hbar = 6.53e-16; %eV

son = 2; %Spin degeneracy

soff = 1; %Spin degeneracy

W = 0.5;

S_0 = 0.2; %oscillations coupling
```

```

Q = 10; %Phonon number

qi = linspace(1,Q,Q); %initial

qf = linspace(1,Q,Q); %final

Vg = linspace(-12.5,12.5,100);% linspace(-1e-3,1e-3,3); Gate voltage

V = linspace(-25,25,100); %Source-drain voltage

%% Franck-Condon matrix elements calculations for vibrations and oscillations

for i = 1:length(qi);

    for j = 1:length(qf);

        if (qf(j) >= qi(i));

            A = (-1)^(qf(j)-qi(i));

        else

            A = 1;

        end

        q1 = min(qi(i)-1,qf(j)-1);

        q2 = max(qi(i)-1,qf(j)-1);

        q1 - q2 ;

        %Mvibone      =      (factorial(q1)/factorial(q2))^(0.5)*lambda^(q2-q1)*exp(-
0.5*(lambda^2))*polyval(LaguerreGen(q1,q2-q1),lambda^2)*A;

        Mvibone      =      (factorial(q1)/factorial(q2))^(0.5)*lambda^(q2-q1)*exp(-
0.5*(lambda^2))*polyval(LaguerreGen(q1,q2-q1),lambda^2)*A;

```

```

MoscLe = ((2^(q2-q1)*factorial(q1))/factorial(q2))^(0.5)*(-0.5/S_0)^(q2-q1)*exp(-
0.25*(1/S_0)^2)*polyval(LaguerreGen(q1,q2-q1),(0.5*(1/S_0)^2));

```

```

MoscRe = ((2^(q2-q1)*factorial(q1))/factorial(q2))^(0.5)*(0.5/S_0)^(q2-q1)*exp(-
0.25*(1/S_0)^2)*polyval(LaguerreGen(q1,q2-q1),(0.5*(1/S_0)^2));

```

```

Mvibon(i,j) = Mvibone;

```

```

Mviboff = transpose(Mvibon);

```

```

Mosc(i,j) = MoscLe;

```

```

end

```

```

end

```

```

GammaonvibL = t_L^2*son*(abs(Mvibon)).^2;

```

```

GammaonvibR = t_R^2*son*(abs(Mvibon)).^2;% units of 2*pi*rho/hbar

```

```

GammaoffvibL = t_L^2*soff*(abs(Mviboff)).^2;

```

```

GammaoffvibR = t_R^2*soff*(abs(Mviboff)).^2;

```

```

% Gammaonosc = t_0^2*son*(abs(Mosc)).^2;

```

```

% Gammaoffosc = t_0^2*soff*(abs(Mosc)).^2;

```

```

GammaonoscL = t_L^2*son*(abs(Mosc)).^2;

```

```

GammaonoscR = t_R^2*son*(abs(Mosc)).^2;

```

```

GammaoffoscL = t_L^2*soff*(abs(Mosc)).^2;

```

```

GammaoffoscR = t_R^2*soff*(abs(Mosc)).^2;

```

```

imagesc(abs(Mvibon))

```

```

%set(gca,'YDir','normal')

```

%% Transition rates and rate equation model using either vibrations or oscillations

for l = 1:length(Vg);

for k = 1:length(V);

for i = 1:length(qi);

for j = 1:length(qf);

%Gammaonvib(i,j)

E(i,j) = Enq(1,Vg(l),Epho,qi(i))-Enq(0,Vg(l),Epho,qf(j));

F(i,j) = ((1-Fermi(Enq(1,Vg(l),Epho,qi(i))-Enq(0,Vg(l),Epho,qf(j)),V(k)/2,T)))+(1-Fermi(Enq(1,Vg(l),Epho,qi(i))-Enq(0,Vg(l),Epho,qf(j)),-V(k)/2,T));

F1(i,j) = (1-Fermi(Enq(1,Vg(l),Epho,qi(i))-Enq(0,Vg(l),Epho,qf(j)),-V(k)/2,T));

% Wvibone = Gammaonvib(i,j)*(Fermi(Enq(1,Vg(l),Epho,qf(j))-Enq(0,Vg(l),Epho,qi(i)),V(k)/2,T)+Fermi(Enq(1,Vg(l),Epho,qf(j))-Enq(0,Vg(l),Epho,qi(i)),-V(k)/2,T));

% Wvibon(i,j) = Wvibone;

% Wviboffe = Gammaoffvib(i,j)*((1-Fermi(Enq(1,Vg(l),Epho,qi(i))-Enq(0,Vg(l),Epho,qf(j)),V(k)/2,T)))+(1-Fermi(Enq(1,Vg(l),Epho,qi(i))-Enq(0,Vg(l),Epho,qf(j)),-V(k)/2,T));

% Wviboff(i,j) = Wviboffe;

WvibonLe = GammaonvibL(i,j)*(Fermi(Enq(1,Vg(l),Epho,qf(j))-Enq(0,Vg(l),Epho,qi(i)),V(k)/2,T));

WvibonRe = GammaonvibR(i,j)*(Fermi(Enq(1,Vg(l),Epho,qf(j))-Enq(0,Vg(l),Epho,qi(i)),-V(k)/2,T));

```

WvibonL(i,j) = WvibonLe;

WvibonR(i,j) = WvibonRe;

Wvibon = WvibonL + WvibonR;

WviboffLe      =      GammaoffvibL(i,j)*(1-Fermi(Enq(1,Vg(l),Epho,qf(i))-
Enq(0,Vg(l),Epho,qf(j)),V(k)/2,T));

WviboffRe      =      GammaoffvibR(i,j)*(1-Fermi(Enq(1,Vg(l),Epho,qf(i))-
Enq(0,Vg(l),Epho,qf(j)),-V(k)/2,T));

WviboffL(i,j) = WviboffLe;

WviboffR(i,j) = WviboffRe;

Wviboff = WviboffL + WviboffR;

%      WosconLe = GammaonoscL(i,j)*(Fermi(Enq(1,Vg(l),Epho,qf(j))-
Enq(0,Vg(l),Epho,qf(i)),V(k)/2,T));

%      WosconRe = GammaonoscR(i,j)*(Fermi(Enq(1,Vg(l),Epho,qf(j))-
Enq(0,Vg(l),Epho,qf(i)),-V(k)/2,T));

%      WosconL(i,j) = WosconLe;

%      WosconR(i,j) = WosconRe;

%      Woscon = WosconL + WosconR;

%      WoscoffLe = GammaoffoscL(i,j)*((1-Fermi(Enq(1,Vg(l),Epho,qf(i))-
Enq(0,Vg(l),Epho,qf(j)),V(k)/2,T));

%      WoscoffRe = GammaoffoscR(i,j)*((1-Fermi(Enq(1,Vg(l),Epho,qf(i))-
Enq(0,Vg(l),Epho,qf(j)),-V(k)/2,T));

%      WoscoffL(i,j) = WoscoffLe;

%      WoscoffR(i,j) = WoscoffRe;

```

```

%      Woscoff = WoscoffL + WoscoffR;

      M0eq(i,j) = 1/tau*[exp(-((qi(i)-1)*Epho)/(kb*T))*(1-exp(-Epho/(kb*T))));

      end

end

Meq = [M0eq zeros(size(M0eq));

      zeros(size(M0eq)) M0eq];

Meqtau = [M0eq zeros(size(M0eq));

      zeros(size(M0eq)) M0eq] - eye(size(Meq)).*(1/tau);

M = [zeros(size(Wvibon)) Wviboff';

      Wvibon' zeros(size(Wvibon))] - [diag(sum(Wvibon, 2)) zeros(size(Wvibon));

      zeros(size(Wvibon)) diag(sum(Wviboff, 2))] - Meqtau;

%      M = [zeros(size(Woscon)) Woscoff';

%      Woscon' zeros(size(Woscon))] - [diag(sum(Woscon, 2)) zeros(size(Woscon));

%      zeros(size(Woscon)) diag(sum(Woscoff, 2))] - Meqtau;

[P,D] = eig(M);

[a,b]=min(abs((diag(D))));

P = abs(P(:,b));

p1(i,j) = abs(P(1));

```

```

P0 = transpose(P(1:length(qi)));

P1 = transpose(P(length(qi)+1:end));

I(k,l) = 0;

for i = 1:length(qi);

    for j = 1:length(qf);

        %l(k,l) = sum((P0+P1)*WvibonL);

%        I(k,l) = I(k,l) + WosconL(i,j)*abs(P(j))-WoscoffL(i,j)*abs(P(j+Q));

        I(k,l) = I(k,l) + WvibonL(i,j)*abs(P(i))-WviboffL(i,j)*abs(P(i+Q));

    end

end

end

end

end

%figure;

imagesc(Vg,V,diff(I))

set(gca,'YDir','normal')

%plot(V,I)

%Won(i,j) = Won;

%bar3(Gammaonvib)

%set(gca,'YDir','normal')

```

Matlab Code: Functions

```
function y =Fermi(E,V,T);
```

```
kb = 8.62e-5;
```

```
y = 1./((exp((E-V)/kb*T)+1));
```

```
function y = Enq(n,Vg,E,q);
```

```
y= n*Vg + E*(q+0.5);
```